Development and Testing of an Externally Finned Tube Cavity Receiver for Brayton Cycle Preheating Purposes

by
Elias Johannes Jacobus Basson

Thesis presented in partial fulfilment of the requirements for the degree of Master of Engineering (Mechanical) in the Faculty of Engineering at Stellenbosch University

Supervisor: Dr. JE Hoffmann
Co-supervisor: Prof. AB Sebitosi

April 2019

Declaration

By submitting this thesis electronically, I declare that the entirety of the work contained therein is my own, original work, that I am the sole author thereof (save to the extent explicitly otherwise stated), that reproduction and publication thereof by Stellenbosch University will not infringe any third party rights and that I have not previously in its entirety or in part submitted it for obtaining any qualification.

Date: April 2019

Abstract

Development and Testing of an Externally Finned Tube Cavity Receiver for Brayton Cycle Preheating Purposes

E.J.J. Basson

Department of Mechanical and Mechatronic Engineering,

Stellenbosch University,

Private Bag X1, Matieland 7602, South Africa

Thesis: MEng (Mech)

March 2019

The low cost energy storage of concentrated solar power is the biggest advantage of this technology over other renewable energy sources. This storage enables such a power plant to dispatch the energy on demand. A combined cycle air driven CSP plant called the SUNDISC, consisting of an upstream solarised Brayton cycle with an intermediate rock bed energy storage and a downstream steam Rankine cycle, was conceived at Stellenbosch University. The use of air as working fluid enables potential co-firing with natural gas in the solarised Brayton cycle. This increases the annual capacity factor and ensures nominal operation during periods of intermittent irradiation. The bottoming Rankine cycle further increases the annual capacity factor of the plant and with the aid of the rock bed, the bottoming cycle can deliver power on demand after the sun has set.

The Brayton cycle gas turbine, however, limits the mass throughput and thereby the charging quantity to the storage and bottoming cycle during periods of high solar resource. In past studies of the SUNDISC cycle a receiver system capable of bypassing the Brayton cycle and directly charging the rock bed was conceived and investigated numerically. The Hybrid Pressurised Air Receiver (HPAR) intends to supply compressed air to the Brayton cycle and atmospheric air to the rock bed simultaneously. Simulation suggested that the desired thermal output to the rock bed could not be achieved. Several suggestions to improve the heat transfer to the non-pressurised side were made, among which was the addition of external fins to the tubes. The objective of this study is to experimentally determine the ray trapping and heat transfer enhancement effect of external fins.

In this project, a test receiver was designed based on the suggestions from previous studies. The receiver was instrumented and installed at the receiver test facility of STERG at Stellenbosch University where several tests were conducted to determine the behaviour of the modified HPAR.

The experimental investigation yielded on-sun data with which future investigations can be validated. The circumferential temperature distribution on selected tubes, the volumetric cavity temperature, the heat removal relationship between the inner and outer fluid and the ray penetration depth was captured. Using the test data a sensitivity analysis of the on-sun tests were conducted which highlights the sensitivities of the receiver to the environmental effects.

During the experimental investigation, the receiver demonstrated the ability to modulate the circumferential temperature gradient on the tubes which can potentially reduce thermal fatigue of the components. The receiver further demonstrated the ability to control the different energy absorption quantities to the two streams, enabling better thermal control of the receiver and cycle. Lastly, the receiver was found to be fairly insensitive to wind and demonstrated the ability to capture and repurpose the convective losses, thereby further increasing its efficiency.

Uittreksel

Ontwikkeling en toets van ‘n ekstern gevinde buis luik ontvanger vir Brayton siklus voor verhittings doeleindes

E.J.J. Basson

Department of Mechanical and Mechatronic Engineering,

Stellenbosch University,

Private Bag X1, Matieland 7602, South Africa

Thesis: MEng (Mech)

March 2019

Die lae koste energie berging van gekonsentreerde sonkrag is die grootste voordeel bo ander hernubare energiebronne. Hierdie lae koste berging stel so 'n kragsentrale instaat om energie op aanvraag te voorsien. 'n Gekombineerde siklus, lug gedrewe, CSP-aanleg, met 'n primêre Brayton-siklus, 'n intermediêre rotsbed energie-stoor en 'n sekondêre Rankine-siklus, bekend as die SUNDISC siklus is deur die Universiteit Stellenbosch ontwikkel. Die gebruik van lug as werksvloeier maak die verbranding van gasse moontlik in die Brayton-siklus. Hierdie verbranding van gasse verhoog die jaarlikse kapasiteitsfaktor en verseker nominale uitsette van die aanleg gedurende die nag en bewolkte toestande. Die sekondêre Rankine-siklus verhoog die jaarlikse kapasiteitsfaktor van die plant verder. Met behulp van die rotsbed energie berging kan die sekondêre siklus op aanvraag energie lewer nadat die son gesak het.

Die Brayton-siklus gasturbine beperk egter die lug se massavloei en sodoende die laaikapasitiet van die energie-stoor en sekondêre siklus gedurende periodes van hoë straling op die heliostaat veld. In vorige studies was 'n ontvangerstelsel wat die Brayton-siklus kan omseil en die rotsbed direk laai opgeteken en ondersoek. Die Hybrid Pressurised Air Receiver (HPAR) beoog om gelyktydig saamgeperste lug na die Brayton-siklus en atmosferiese lug na die energie-stoor te voorsien. Simulasies het bevind dat die termiese doelwitte van die rotsbed nie bereik kan word deur die ontvanger nie. Verskeie voorstelle om die warmteoordrag na die atmosferiese kant van die ontvanger te verbeter is gemaak, mees prominent die byvoeging van eksterne vinne aan die buise.

Die uiteindelike doel van hierdie studie is om eksperimenteel die stralings-vasvang- en warmoordrag-effek van hierdie toevoeging te bepaal.

In hierdie projek is 'n toetsontvanger ontwerp op grond van die voorstelle van vorige studies. Die ontvanger is by die ontvanger toetsfasiliteit van STERG aan die Universiteit Stellenbosch geïnstalleer. Verskeie toetse was uitgevoer in ‘n poging om die gedrag van die gewysigde HPAR te bepaal.

Die eksperimentele ondersoek het data gelewer waarmee toekomstige ondersoeke gevalideer kan word. Die omtrek-temperatuur verspreiding op geselekteerde buise, die volumetriese holte temperatuur, die hitte verwydering verhouding tussen die binneste en buitenste vloeier en die penetrasie diepte is vasgelê. Deur gebruik te maak van die toetsdata is 'n sensitiwiteitsanalise uitgevoer. Die sensitiwiteit van die ontvanger ten opsigte van die omgewings-effekte was beklemtoon.

Tydens die eksperimentele ondersoek het die ontvanger die vermoë getoon om die omtrek-temperatuurgradiënt op die buise te beheer. Hierdie beheer kan die termiese uitputtingsvermoë van die komponente moontlik verbeter. Die ontvanger het ook die vermoë om die verskillende energie-absorpsie kwantiteite van die twee strome te beheer bewys, wat beter beheer oor die ontvanger en siklus instaat stel. Laastens was die ontvanger redelik onsensitief vir eksterne winde tydens die toetse. Die ontvanger het die vermoë getoon om die konveksie-verliese vas te vang en oor te dra na die interne vloeier en sodoende die doeltreffendheid verder te verhoog.

Acknowledgements

"Research is what I'm doing when I don't know what I'm doing"-Wernher von Braun

I would like to thank everyone who helped me along the way in large and small contributions. In particular the following:

- Our heavenly Farther for blessing me with the opportunities and abilities to have conducted this research project.
- My parents and family for their continued support, prayers and understanding throughout the project.
- Dr. Hoffmann and Prof. Sebitosi for their guidance, insight and project funding which allowed me to do independent research.
- The mechanical workshop staff for constructing and installing the test setup.
- Fellow STERG members who gave helpful insights over coffee.
- The NRF for funding to complete this project.

Table of Contents

List of Figures

List of Tables

Nomenclature

Constants

$R_{air} = 287.08\ \frac{\mathrm{J}}{\mathrm{kgK}}$	Uneversal gas constant
$\sigma = 5.670 \times 10^{-8}\ \frac{\mathrm{W}}{\mathrm{m^2K^4}}$	Stefan Boltzmann constant

Variables

A	Area	[m^2]
c_p	Specific heat	[J/kgK]
d	Diameter	[m]
E	Youngs modulus	[Pa]
h	Convective heat transfer coefficient	[W/m^2K]
f	View factor	[-]
R	Thermal resistance	[W/K]
T	Temperature	[K]
P	Pressure	[Pa]
l_c	Characteristic length	[m]
$\dot{m}$	Mass flow rate	[kg/s]
Q	Heat transfer	[W]
q	Heat flux	[W/s]
k	Thermal conductivity	[W/mK]
DNI	Direct normal irradiation	[W/m^2]
v	Velocity	[m/s]
R_e	Reynolds Number	[-]
I_{ss}	Incident solar flux	[W/m^2]
L	Length	[m]
Nu	Nusselt number	[-]
dP	Differential pressure	[Pa]
t	Time	[s]
U	Heat transfer coefficient	[W/m^2K]
α	Absorptivity	[-]
α_l	Thermal expansion coefficient	[1/°C]
β	Venturi throat diameter ratio	[-]
ε	Emissivity	[-]
η	Efficiency	[-]
μ	Dynamic viscosity	[kg/ms]
ν	Kinematic viscosity	[m^2/s]

Subscripts

0	Initial
Abs	Absorbed
A	Air
Atm	Atmosphere
Avg	Average
Conv	Convective
Cond	Conductive
Cosine	Cosine reflectance
F	Fluid/fin
G	Gas
I	Initial
Int	Internal
loss/l	Heat loss from boundary typically to convection and radiation
O	Outer
Out	Outlet
Rad	Radiation
Reflect	Reflectance
S	Surface
SF	Solar Field
SB	Shading and blocking
Sky	Sky/ambient
Spill	Heliostat spillage
Tube/t	Tube
Use	Energy transported from the control volume

Abbreviations

CFD	Computational Fluid Dynamics
CSP	Concentrated Solar Power
DLR	German Aerospace Center
DO	Discrete Ordinates
FV	Finite Volume
GT	Gas Turbine

HPAR	Hybrid Pressurised Air Receiver
HPRS	High Pressure Receiver System
HTF	Heat Transfer Fluid
LCOE	Levelized Cost Of Electricity
LPRS	Low Pressure Receiver System
NPA	Non-Pressurised Air
PA	Pressurised Air
PSA	Plataforma Solar de Almeria
RTE	Radiative Transfer Equation
SASEC	Southern African Solar Energy Conference
SCRAP	Spiky Central Receiver Air Pre-heater
SG	Steam Generator
SolarPACES	Solar Power and Chemical Energy Systems
SU	Stellenbosch University
SUNDISC	Stellenbosch University Direct Storage Charging cycle
SUNSPOT	Stellenbosch University Solar Power Thermodynamic cycle
STERG	Solar Thermal Energy Research Group

Chapter 1

Introduction

1.1. Background to the research problem

In 2016 the G20 countries were responsible for 81% of the global CO_2 emissions. Of these emissions more than half of the fossil fuel related CO_2 emissions were generated by coal combustion. Further, it is estimated that one-third of the G20 countries' combined CO_2 emissions were generated by the power generation sector (Olivier *et al.*, 2017).

These global carbon emissions are causing the global climate to heat up which can potentially lead to catastrophic consequences. On 12 December 2015, the Paris Climate Agreement was negotiated and signed by 195 countries. This agreement seeks to deal with greenhouse gas emissions by means of mitigation, adaptation and finance and is set to start in 2020. A goal has been set on carbon emissions which aim to limit the global average temperature rise to below 2 °C above pre-industrial levels. The need to reduce CO_2 emissions more rapidly was highlighted in the IPCC, (2018) report on the impacts of 1.5 °C global warming above pre-industrial levels.

In order to meet these goals, the global dependency on fossil fuels will need to be reduced. This reduction can be achieved by using a network of carbon-lean and carbon-free renewable energy sources. Concentrated solar power (CSP) plants have the potential to play a major role in renewable power production at utility scale as CSP has the ability to provide dispatchable power by utilising thermal energy storage (TES) systems. This ability of CSP to provide dispatchable power from cost-effective storage is the largest advantage over other renewable sources, excluding hydro.

In a bid to further decrease the levelized cost of electricity (LCOE) it has been proposed to use air as working fluid for CSP power production and storage. This is planned to be achieved by the SUNDISC (Stellenbosch University Direct Storage Charging) cycle which makes use of a co-firing Brayton cycle with a solarised gas turbine and a packed rock bed TES

system that is charged by the exhaust gas of the Brayton cycle. The TES can be discharged on demand to feed energy to a Rankine cycle for power production at night. The further advantage of the SUNDISC cycle is that co-firing natural gas enables the system to be operational on days with an insufficient solar resource, thus increasing the annual capacity factor of the plant.

It has become apparent through investigation that there exists a need for a cost competitive, robust and thermodynamically efficient solar thermal receiver with air as working fluid which can be integrated into such a cycle. The receiver, therefore, needs to be able to satisfy the thermal, mass flow and pressure needs of the cycle.

1.1.1. Background to solar thermal power plants

CSP plants are important candidates to provide a major share of clean and renewable energy. Solar energy is of high quality at the source due to the high temperatures (Romero, *et al.* 2002). The solid angle and distance from the sun to the earth, however, makes it difficult to extract this energy and reach reasonable working fluid temperatures at the surface of earth. This requires CSP plants to rely largely on optical concentration methods.

There are two main CSP technologies that operate at utility scale namely: central tower plants and parabolic trough plants. In the case of central tower plants, left in Figure 1, a field of heliostats collects and concentrates the solar radiation on a heat exchanger at the top of a tower in the middle of the field. Obtainable concentration ratios, with which the receivers and subsequently the heat transfer fluids are heated, vary between 200-1000.

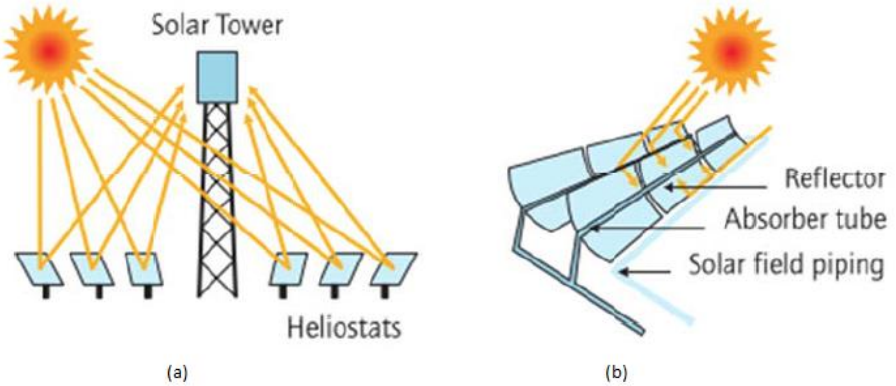

Figure 1: The two dominant utility-scale CSP technologies (International Energy Agency, 2010)

A parabolic trough plant, the right-hand image in Figure 1, uses long reflective parabolic troughs which produce a line focus, concentrating the incident radiation onto an evacuated tube solar collector. Concentration ratios are typically about 50-80. This relative low concentration ratio requires a larger field to generate similar operating temperatures than that of a central tower plant. Another advantage of a central receiver plant over parabolic troughs is that it does not require level terrain, increasing the possible locations of implementation. The plant size is chosen based on the economy-of-scale constraints with plants ranging from 10 to 200 MW.

The energy collected by the receiver is transferred into a heat transfer fluid (HTF). This HTF allows the harnessed solar energy to be used in a turbine and generator set similar to fossil fuel power plants which generally generates steam for a Rankine cycle.

Currently, most trough plants use synthetic oils at a maximum temperature of 350 °C and central tower plants use molten salts at 565 °C. Both these types of plants use steam generators to power the Rankine cycle (International Energy Agency, 2010). The energy quality of central towers is higher than that of trough plants, enabling towers to produce electricity more efficiently from superheated steam.

The higher quality of energy harnessed by central receiver systems has a large potential for mid-term cost reduction of electricity (Romero *et al.* 2002). This is achieved through the ability of central receivers to allow many intermediate power cycle steps, between the integration of a Rankine cycle up to Brayton cycles which uses gas turbines at temperatures of up to 1300 °C. The higher temperatures result in higher throughputs of more efficient cycles according to Romero *et al.* (2002).

The high efficiency and compactness of Brayton cycles with the added benefit of cost-competitive energy storage lead research towards developing cycles using air as working fluid. Air as thermal transfer fluid poses a list of challenges to overcome. Several studies have been carried out over the years and this study aims to contribute to the body of knowledge of central air receivers by testing a proposed air receiver experimentally.

1.1.2. The HPAR

Initially proposed by Kröger (2011), the SUNSPOT (Stellenbosch University Solar Power Thermodynamic) cycle is a combined cycle CSP plant which uses a rock bed as thermal energy storage to enable power

dispatchability, Figure 2 below describes the cycle layout. Heller (2013) identified that the turbine of the Brayton cycle is a bottle-neck by limiting the mass flow throughput to the rest of the system. During periods of high solar resource, some of the energy needs to be shed by defocussing heliostats due to this bottle-neck. This limits the charging of the thermal energy storage (TES), storage rock bed in Figure 2, which in turn limits the total dispatchable energy to the Rankine cycle.

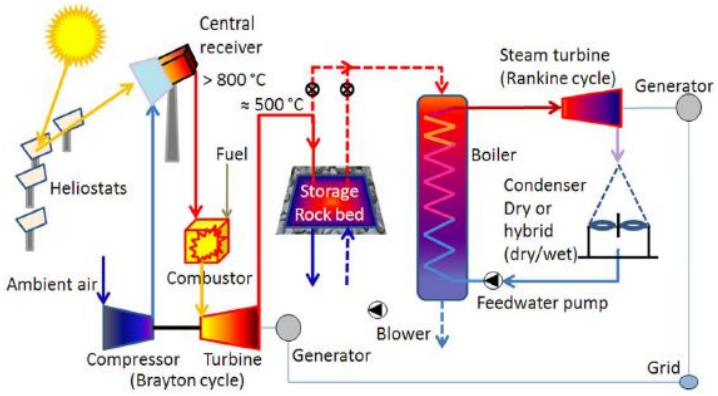

Figure 2: Schematic of the SUNSPOT cycle (Heller, 2017)

Heller (2017) proposed the so-called SUNDISC cycle to overcome the SUNSPOT shortcomings in terms of dispatchability and baseload capability by incorporating two receivers. For the SUNDISC system modelling performed by Heller, two receivers were used to achieve the dual charging. The two receivers chosen was the two most mature air receiver technologies which have demonstrated the ability to reach air temperatures of up to 1000 °C namely the DIAPR (HPRS) and REFOS (LPRS) (Heller 2017). The schematic in Figure 3 illustrates the system layout. The advantage of two receivers on a single tower is the reduction in shading and blocking losses year-round by creating two targets according to Heller.

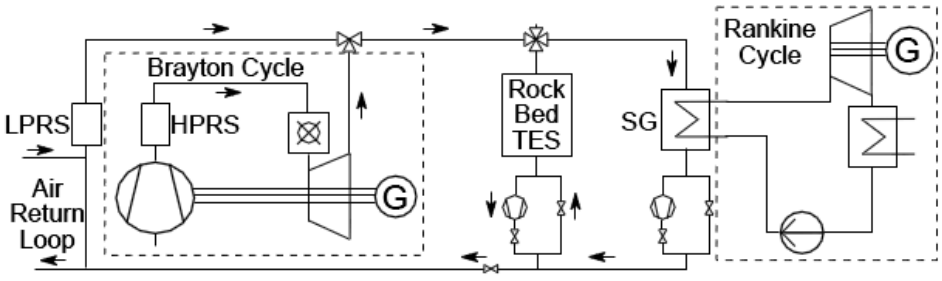

Figure 3: Schematic of SUNDISC cycle (Heller 2017)

The so-called Hybrid Pressure Air Receiver (HPAR) has the potential to satisfy the SUNDISC cycle requirements with a single target. This can possibly reduce the system cost and compared to a closed volumetric receiver more energy can be absorbed thus increasing the thermal efficiency according to Heller.

The HPAR concept has been proposed by Kretzschmar *et al.* (2013) and further refined by Heller (2017). The goal of Kretzschmar *et al.* (2013) was to develop a tubular cavity air receiver that can obtain the volumetric effect. The uniqueness of this receiver is the use of air flow into the receiver cavity to regain the convective losses from the aperture. As a result of this mechanism, the receiver has two air outputs (dual receiver) one at high pressure, from the tubular side and the other at atmospheric pressure, from the open volumetric cavity side. Furthermore, the induced air flow cools the front tubes thus extending the allowable flux intensity on metal tubular receivers.

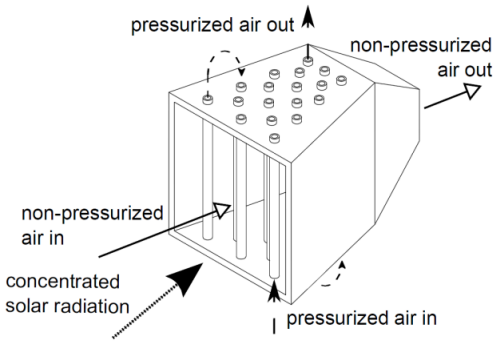

Figure 4: Sketch of the HPAR concept (Heller 2017)

As proof of concept Kretzschmar *et al.* (2013) constructed a staggered tubular receiver to investigate the effect of air flow into the cavity on the surface temperatures and the air temperature development in the receiver. Kretzschmar *et al.* (2013) further investigated the effect of substituting some of the tubes with quartz prisms to reduce the radiative losses to ambient and further increase the surface temperatures by increasing the depth of ray penetration. It was found that the induced flow successfully captures the convective losses to ambient. The findings resulted in further investigations into the HPAR at a research program at the University of Pretoria.

The dual pressure air receiver as proposed by Heller (2017) would allow for the TES to be charged throughout the day while the Brayton cycle is operating by charging directly from the low-pressure receiver and the exhaust of the Brayton cycle.

The dual pressure air receiver, therefore, has to be able to satisfy the requirements of the Brayton cycle and the TES. The goals set by Heller were 800 °C for the Brayton cycle and 524 °C for the TES. During simulation, the target thermal requirements of the TES could not be achieved. This is mainly due to the relationship and priority heating of the two air streams. The simulation and findings are discussed later in Chapter 2. Heller suggested the addition of radial fins to the tubes in an attempt to increase the receiver effectiveness and the unpressurised air outlet temperatures. An increase in heat transfer to the unpressurised air, however, relates to a decrease in heat transfer to the pressurised air stream.

The addition of radial external fins increases the surface area for heat transfer to the unpressurised air. Furthermore, the fins are expected to create micro-cavity effects which reduce the view factor from the base tube to the environment and thereby reduce the radiative losses. This reduction in view factor can in effect shade the base tube to all rays not falling perpendicular onto the tubes and thereby possibly affecting the absorption negatively. The fins are expected to transfer heat to the shadow side of the tubes by means of conduction, thereby reducing the circumferential temperature difference which reduces the fatigue caused by cyclic thermal stresses on the receiver tubes.

In this study, this suggestion is investigated experimentally. The addition of external fins has merit, however, the cost of increasing the heat transfer to the unpressurised air needs to be investigated. For Brayton cycle integration pressurised air needs to be heated in excess of 800 °C, therefore the internal fluid has the highest priority and the secondary flow should be regarded as a bonus. The cost of transferring more heat to the secondary fluid stream is a reduction in heat transfer to the primary cycle.

1.2. Research problem statement

The SUNDISC cycle requires a cost-effective, robust and efficient solar air receiver capable of heating pressurised air to Brayton cycle operating temperatures while supplying the TES and bottoming Rankine cycle with

all the excess energy. Heller (2017) performed a theoretical analysis of the system requirements and the ability of the HPAR to satisfy these needs. There exists no experimental backing to this work which can confirm the conclusions. This investigation was launched as a follow-up with the goal of evaluating the suggestions, assumptions and findings by means of experimental analysis.

The relevancy of the obtained data is of concern, thus an in-depth literature review was carried out in an effort to ensure the experimental setup will be able to answer the questions raised in previous work and be able to provide empirical data with which simulation work can be validated should a continuation of the work be carried out.

1.3. Research objectives

The objective of the research is the experimental investigation of the heat transfer capabilities of externally finned metal tubes in a high radiative flux environment. A tubular cavity receiver based on the design by Kretzschmar (2014) and further suggestions by Heller (2017) was constructed.

The purpose of the experimental setup is to provide data with which a simulation model of the receiver can be validated. It is far cheaper, time and money wise, to test various design changes and operating conditions in a simulation environment and therefore the need for validation data exists. The test receiver will be evaluated for the ability to provide useable data of system response in a 3-D environment during on-sun testing conditions.

Main research outcomes:

- Review the current tubular air receivers and find the most promising aspects of each relevant to the modified HPAR.
- Evaluate the effect of radial fins and induced flow on the circumferential temperature gradient.
- Evaluate the collection efficiency of a finned staggered metal tubular air CSP receiver.
- Capture the receiver thermal response with which future simulations can be validated.

1.4. Methodology and scope

The methodology used to investigate and answer the research question starts with the development of a finned tubular cavity air receiver based on a thorough literature review of the current and past technologies. Once all the limitations and pitfalls have been identified the concept is evaluated by heat transfer analysis in basic theoretical simulation models based on the existing theory. After which components were sourced, the experimental setup was designed, constructed, installed and tested.

Design and development of the receiver concept

The design process was backed by a thorough literature study tied with theoretical models of the proposed receiver geometries. The concept was generated based on limitations, complications and lessons learnt from previous studies in literature. The tube layout optimization would require discrete optimization with either ray penetration or induced flow intensity as the objective function. These objectives are in direct contrast and the effort to find a compromise with an exhaustive search was deemed beyond the scope of this study. The fin spacing selection was limited by the material and the machining capabilities.

As a result, three tube layouts and three fin spacing layouts were generated and evaluated with respect to radiation penetration depth, view factor and flow distribution. From this evaluation one layout with one fin geometry was selected for the experimental setup. The methods employed are discussed in Chapters 3, 4 and 5.

Development of a theoretical model based on heat transfer principles

It took about 4 months to source and construct one experimental receiver. This was the effect of the delivery time and the machining time of the specialised components. The finned tubes alone took 2 weeks to machine. This highlights the need to have data with which a simulation model can be validated in possible future studies.

A 1-D mathematical model was developed based on heat transfer and fluid mechanics principles to characterize the flow into the receiver. This model was used to estimate the effect of fin geometry on the fluid outlet temperatures of the receiver. This iterative solving mathematical model

done in MATLAB provides a fast characterisation of what can be expected in the receiver.

For the scope of this project, the analytical model will suffice. Modelling ray tracing and diffuse radiative heat transfer in 3-D in CFD software cannot be performed in parallel and as a result, a solution is very computationally expensive.

Experimental testing

The conceptual air receiver was manufactured, instrumented and installed on the square lattice tower on the solar roof laboratory of the Solar Thermal Energy Research Group (STERG) at Stellenbosch University. The heliostats of Helio40, a small experimental heliostat field presented in Appendix E, were used to concentrate the solar radiation onto the receiver.

The main objectives of the experimental tests were:

- To measure the circumferential temperature difference on selected tubes in the receiver.
- Measure the surface temperature distribution into the depth of the receiver and thereby evaluate the ray penetration.
- Measure the induced flow temperature distribution in the receiver to evaluate the volumetric effect of the receiver.
- Measure the heat removal relationship between the fluids in the receiver at various flow conditions.

Data analysis

The data needs to be analysed to extract the gathered experimental results with which the research questions are to be answered. The receiver response and sensitivities to the various variables need to be determined. The nature of the simulation models (1-D) has limited accuracy in predicting the response of such a complex 3-D receiver and therefore the results would be better suited to validate future studies.

Chapter 2

Literature Review

2.1. Introduction

This Chapter reviews background literature on the field of central tower CSP, the different types of receivers and the advancements that were made to date. It further underlines the need for the proposed study in air receiver technologies.

2.2. The solar Brayton cycle

The integration of a Brayton cycle in large-scale CSP systems is driven by several factors of which arguably the largest is the ability to run a bottoming Rankine cycle. Such a co-generation cycle increases the annual capacity factor and the total energy throughput. Thermal to electric efficiencies of over 50 % have been proven for co-generation cycles according to Kribus *et al.* (1999). For the bottoming Rankine cycle to operate at a meaningful output the thermal input required is >500 °C which puts a constraint on the Brayton cycle output. This output constraint requires the input to be in excess of 1000 °C (Allen 2010).

The more efficient power cycle, as opposed to steam Rankine, enables the use of smaller machines and thereby reducing the construction cost. Brayton cycle turbines can theoretically generate similar quantities of power to a far larger steam turbine. To extract these quantities of work from a smaller turbine requires the fluids to be at temperatures of >1000 °C compared to the 540 °C of a Rankine cycle. This higher temperature requirement creates the need for more exotic materials which are able to withstand the operating conditions. These materials increase the component cost and thereby the cost of the whole system.

According to Çengel & Boles (2011), the ideal Brayton cycle consists of an isentropic compression in the compressor, followed by a constant pressure heat addition and then isentropic expansion in the turbine. The thermal efficiency of the Brayton cycle is dependent on the pressure ratio between the compressor and turbine. The requirements of the Brayton cycle and

the sensitivities need to be kept in mind when designing a solarized gas turbine and receiver coupled system. Equation 1 represents the Brayton cycle efficiency relationship where r_p is the pressure ratio between the compressor and turbine and k the specific heat ratio.

$$\eta_{\text{th,Brayton}} = 1 - \frac{1}{r_p^{\frac{k-1}{k}}} \tag{1}$$

The incurred cost and technical challenges faced to compress hot air at atmospheric conditions necessitate that the heat be added to a pressurised fluid. This can be achieved by either tubular or closed volumetric receivers. The capability of solar energy to add the heat at nearly constant pressure paves the way for solarised gas turbine technology with possible co-firing of natural gas to reach the desired turbine temperatures.

In the case of receiver design, special focus is placed on the obtainable temperature gain in the fluid stream while the pressure drop needs to be minimised. Heller (2017) stated that the allowable pressure drop between the compressor and turbine stage for pressurised air receiver systems is commonly between 200 mbar to 300 mbar. In this investigation, the internal fluid heat transfer is not of concern and as a result, the allowable pressure drop is not part of the design objectives.

2.3. Air as working fluid

Air is an attractive choice as HTF for Brayton cycle CSP applications. The use of air is motivated by various advantages such as the ambient availability, environmentally friendly characteristics, absence of phase changes under working conditions, stability at high temperatures, ease of operation and maintenance (Heller 2013). Furthermore, air is an oxidant which enables combustion of natural gas to increase the energy quality of the HTF. Solarisation of a gas turbine enables the plant to operate at nominal capacity during periods of intermittent solar resource, thus enabling baseload supply irrespective of the solar conditions (Heller 2013).

In contrast to the attractive qualities, air has some drawbacks as a HTF, such as the low density and poor thermal characteristics. These drawbacks require the use of pressurized tubular and volumetric receivers to supply energy to the solarised gas turbine. The cost of compressing the air at elevated temperatures has led the research field to place the receiver between the compressor and turbine stage of the gas turbine.

The modified HPAR intends to use two air streams and therefore needs to maximise the heat transfer to both streams while minimising the pressure loss experienced as per Brayton cycle requirements.

2.4. History of air as working fluid

The use of air as working fluid for central receiver system (CRS) plants has been demonstrated since the early 1980's. During 1985-1986 at the Plataforma Solar de Almeria (PSA) facility, a metallic tube receiver was tested and found to be able to produce 2.45 kg/s of hot air at 9.5 bar and 800 °C outlet temperature (Romero *et al.* 2002). In 1987 a second panel with ceramic SiC tubes was tested at the facility with a mass flow rate of 0.48 kg/s at 9.3 bar achieving an outlet temperature of 1000 °C. Although the temperatures obtained was in the range of the Brayton cycle's requirements the capital cost involved and the low incident solar flux permitted by the tubes (lower than 200 kW/m^2) made it uneconomical to pursue the construction of such a plant (Romero *et al.* 2002). The allowable incident solar flux permitted by the tubes is theoretically increased in the modified HPAR by removing energy more efficiently from the receiver tubes. The ability to remove the heat from the outside surfaces, therefore, needs to be investigated in the experiment.

The rise of volumetric air receivers saw a renewed interest in air as heat transfer and working fluid. Volumetric receivers are highly porous structures which absorb the incident solar flux. The solar radiation is not absorbed on the outer surface but instead in the depth of the structure where radiative losses are less dominant. In such a receiver the air is forced through the porous structure and is subsequently heated by means of forced convection (Romero *et al.* 2002).

The measure of a good volumetric absorber is the ability to have the fluid leaving the absorber at a higher temperature than the irradiated side of the porous media (Romero *et al.* 2002). This phenomenon is called the volumetric effect and has not as of yet been demonstrated in a commercial receiver. A common problem experienced by volumetric receivers is a non-uniform mass flow distribution across the receiver. This can lead to hot and cool spots and which generates thermal stresses. To ensure the mass flow rate is evenly distributed specific design needs to be done, such as the addition of perforated plates in the porous media.

A variety of volumetric receiver prototypes have been tested and most demonstrate the ability to produce hot air at temperatures of 1000 °C with apertures of similar size to that of molten salt and direct steam receivers. Average operating fluxes of 400 kW/m^2 and peak flux values of up to 1000 kW/m^2 have been proven (Romero *et al.* 2002 and Ávila-Marín 2011).

The non-pressurised air side of the modified HPAR is, in essence, a volumetric receiver and the shortcomings of such a volumetric receiver therefore need to be addressed.

2.5. Thermal energy storage

Thermal energy storage serves multiple purposes in a CSP plant, setting it apart from other renewable energy systems. The main advantage of TES is the cost effective power delivery on demand to the grid and the ability to smooth out fluctuations in the demand. Other advantages include the ability to ensure steady system output over periods of intermittent solar radiation by supplementing the energy supply to the power block. In addition to demand matching, the hours of power block operation is increased which increase the annual capacity factor of CSP plants to higher than that of photovoltaic (PV) plants.

According to Heller (2013), the major properties defining TES systems in CSP are:

- The volumetric energy capacity
- Charge and discharge rates
- Maximum and minimum temperatures
- Safety and environmental impact
- Thermal and chemical stability for thousands of cycles
- Heat losses
- Quality of thermocline after charging
- Degradation of thermocline during idle mode
- Power requirements for charging and discharging
- Cost

The simplest and most efficient way of storing thermal energy harnessed by a CSP plant is by using the primary HTF as the storage medium. For

thermal storage in gasses to be effective the gasses need to be kept at condensed condition under high pressures which results in low volumetric energy capacity (Heller, 2013).

As mentioned in section 2.3., air has poor thermal properties which make storage a challenge for air Brayton cycle implementations. A solution is to use a packed rock bed as thermal storage. The rock bed storage is charged by pumping the high-temperature exhaust air from the Brayton cycle through the rock bed. The bed is fully charged once the rocks in the bed reach the inlet air temperature. When the energy is required to be dispatched, ambient air is drawn through the packed rock bed whereupon it heats up to power the secondary power cycle.

The most notable research at Stellenbosch University of rock bed TES studies was carried out by Allen (2010) and Laubscher (2017). A test plant was constructed by Laubscher on which charging and discharging tests were carried out. The main findings were that the TES constructed by Laubscher which had no thermal insulation of the bulk storage material should not be used in the CSP industry as it was not reliable or effective over long periods of storage. Based on these findings a further study was undertaken by Erasmus *et al.* (2018) in which thermal insulation is added to the rock bed amongst other enhancements. As of yet, the findings of the extended research have not been published.

The intended purpose of the non-pressurised side of the modified HPAR is to supply air at the required charging thermal conditions of the intermediate rock bed TES. The suggested addition of the external fins by Heller (2017) is directly aimed at increasing the heat transfer to the non-pressurised side and as a result, the effect thereof needs to be determined in the experimental study.

2.6. Receiver technologies

The following section covers a review of solar thermal plants with a central air receiver system based on articles by Romero *et al.* (2002) and Ávila-Marín (2011). The background review is followed by an overview of the different central receiver technologies, the advantages and pitfalls of each are identified as far as possible.

2.6.1. Summary of air CSP test plants

The high solar fluxes impinging on a central receiver ranging between 300-1000 kW/m^2 enable the receiver components to reach temperatures of up to 1000 °C, depending on the operating conditions. These conditions allow smaller receivers to be employed which operate at higher efficiencies. The higher component temperatures enable the implementation of this thermal energy into more efficient cycles and hybrid fossil fuel plants.

For a Brayton cycle such as the one to be employed in both the SUNSPOT and SUNDISC cycle an operating temperature of at least 800 °C for the working fluid is required (Romero *et al.* 2002). This temperature goal ensures that the exhaust temperature is high enough to efficiently run a bottoming steam Rankine cycle.

The use of open- and closed volumetric receivers coupled to the Brayton cycle with packed bed, rock or ceramic, thermal storage systems is the most promising setup which uses air as working fluid. These cycles have the potential of hybridization where combustion of natural gas is used to increase the temperatures further from 800 °C to the desired operating temperature of the gas turbine that is used. Projects that tested this cycle include SOLGATE, PS10 and Consolar (Romero *et al.* 2002).

This hybridization approach offers a solution to break the non-technological financial barriers to the large-scale deployment of solar electric technologies which in turn reduces the initial investment. These hybrid plants offer investors lower risks since the technology is proven. These plants are, however, classified as carbon-lean instead of carbon-free.

The PHOEBUS cycle was eventually installed on top of CESA-1 tower in Spain and operated by DLR and CIEMAT for nearly 400 hours between April and December 1993 and for shorter periods between 1994 and 1999. The plant had a 2.5 MW_t receiver and the most notable finding was that the receiver can reach air output temperatures of 700 °C with ease within 20 minutes of plant start-up (Romero *et al.* 2002).

The results of the PHOEBUS tests helped TSA (Technology Program Solar Air Receiver) to convince Abengoa to promote the first commercial air Brayton demonstration plant in a project named PS10 which started in 1999 and the goal was to connect 10 MW to the grid in Seville (Spain). The concept was however changed and the eventual PS10 had a saturated steam receiver instead according to Kaltschmitt *et al.* (2007).

In Table 1 a summary of the most prominent pressurised air receiver projects are presented. This survey on pressurised air receiver development was done by Lubkoll, *et al.* (2014).

Table 1: Updated summary of important pressurised air receiver projects (Lubkoll *et al.* 2014)

Project	Receiver	Receiver type	Temperature achieved	Project start
DIAPR	DIAPR	Volumetric cavity	1200 °C	1992
REFOS	REFOS	Volumetric cavity	800 °C	1996
SOLGATE/HTS	Two REFOS and LT stage	Volumetric cavity and tubular cavity	1030 °C	2001
SOLHYCO	SOLHYCO	Tubular cavity	800 °C	2006
SOLUGAS	SOLUGAS	Tubular cavity	800 °C	2008
SOLTREC	SOLUGAS and REFOS	Volumetric cavity and tubular cavity	-	2010
ETH Zürich	ALSTOM	Volumetric cavity	1200 °C	2009

2.6.2. Cavity receiver[1]

The use of a cavity to house the receiver has been demonstrated successfully over the years of receiver development. The cavity serves multiple purposes, the most important being the reduction of the two major losses namely convective and radiative heat loss (Lubkoll *et al.* 2014).

Convective heat loss is reduced by shielding the high-temperature components from winds and other atmospheric conditions. Further, the cavity geometry and depth reduces the view factor from the receiver components to the sky and environment and therefore reduces radiative losses.

A receiver that does not employ a cavity needs to overcome these losses in another way. The most effective method is to increase the heat removal efficiency of the receiver components which experience the largest energy losses. The increased energy extraction reduces the surface temperature and thereby the potential losses.

[1] Note that the term cavity receiver refers to any receiver technology which employs a cavity and does not refer to a specific receiver.

In the case of the modified HPAR the ability of the external induced flow to remove energy from the tubes and trap the convective losses is greatly dependent on the flow conditions. The addition of a cavity to increase the effectiveness of the forced convection over the tubes needs to be investigated and implemented.

2.6.3. Tubular receiver

Tubular receivers are the main competitor of volumetric receivers. The limitations of tubular receivers such as material stress and allowable incident flux, however, favour volumetric receivers for gas based HTF central receivers according to Ávila-Marín (2011).

In CSP plants incident radiation from the solar field falls unidirectionally onto the tubes, resulting in non-uniform circumferential absorbed flux and thereby a non-uniform circumferential temperature distribution. This thermal gradient on the circumference leads to non-homogeneous expansion and thus thermal stresses during thermal cycling. In boilers, the thermal cycles typically last between several days and months of operation and the effect of thermal cycling is not as severe. Tubular solar receivers on the other hand experience at least one thermal cycle per day. This higher rate of cycling poses a challenge to find a solution which increases tube life in this environment. The modified HPAR may provide some solutions in this regard. The magnitude of the thermal stresses can be reduced by ensuring a more uniform expansion of the components during thermal cycling.

In the case of air as HTF however, the tubular receiver needs to be re-evaluated and adjusted to facilitate efficient heat transfer to a HTF with low thermal capacity. Several enhancements are added to the tubes to overcome the challenge of ineffective heat removal, these enhancements are discussed later in section 2.7.

The most relevant tubular receiver is SOLHYCO (DLR 2010). For the SOLHYCO project of the DLR, innovative Profiled Multi-Layer tubes were developed to reduce the temperature difference on the circumference of the tube and thereby increase the heat transfer by improving the thermal distribution. These tubes consisted of Inconel outer copper middle layer and Inconel inner layer. The high conductivity of the copper was used to reduce the circumferential temperature. During tests, the circumferential tube temperature difference was reduced to within 80.9% of

the front temperature. The unequal expansion damaged the intermetallic connection during these tests and as a result, the tubes were never used in a receiver according to the final report summary of the SOLHYCO project to the European Commission (DLR 2010).

Solar-hybrid microturbine systems with cogeneration offer new possibilities in the electricity generation and heating and cooling industry. The SOLHYCO system development presented by Amsbeck, *et al.* (2008) is a 100 kW_e microturbine system which employs a receiver designed for air preheating of up to 800 °C at a pressure of 4.5 bar_{abs}. The receiver consists of multiple metallic tubes arranged in a cavity and connected in parallel as depicted in Figure 5.

Several heat transfer enhancements were investigated in a bid to maximize the receiver efficiency, these are discussed later in section 2.7. Wire-coil inserts were chosen to enhance the internal heat transfer by breaking the boundary layer and mixing the colder core flow with the warmer fluid at the wall interface. The wire inserts do not increase the heat transfer surface as the thermal contact between the coil and the wall is small. The inserts do however contribute to the pressure loss of the system and should therefore be optimised for.

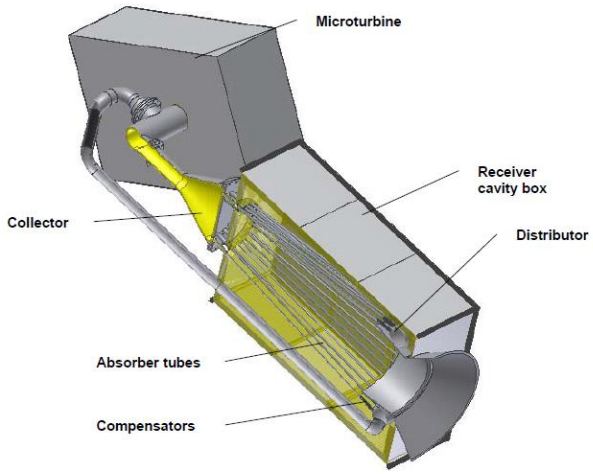

Figure 5: Half-section of the SOLHYCO-receiver (Amsbeck *et al.* (2008))

The predicted efficiency at design point of 77.7 % is low compared to that of a volumetric receiver. Amsbeck, *et al.* (2008) predicted that this value can be increased by decreasing the aperture area, a typical trade-off in the receiver design field. By decreasing the aperture area, the area with the highest radiative losses to the environment is reduced. For this to be

successful a secondary reflector is commonly employed to increase the incident flux density on the aperture. This higher incident flux intensity will allow the receiver to either obtain higher temperatures at the same operating point or allow higher mass flow rates at the same outlet temperatures.

The modified HPAR intends to use the induced flow and the fin geometries to achieve higher collection efficiencies and does not experience the same convection and radiation loss conditions. The aperture size needs to be kept reasonably small to ensure the effectiveness of the external flow. The addition of secondary reflectors can be beneficial in future studies, however, the optical losses of a secondary reflector need to be compared to the gain in flux intensity before implementation.

Another project which employs a tubular receiver to power a solar thermal Brayton cycle was carried out by Le Roux *et al.* (2011) at the University of Pretoria. The project investigated the maximum net power output of a recuperative open and direct solar thermal Brayton cycle with the aid of objective functions. The cavity receiver originally modelled by Le Roux *et al.* was based on the modified cavity receiver for a solar dish concentrator by Reddy and Kumar (2009). The receiver cavity was made up of wound copper tubing, similar to the SOLGATE LT multi-tube coil receiver, but with a smaller aperture to trap more re-radiation from the inner tubes.

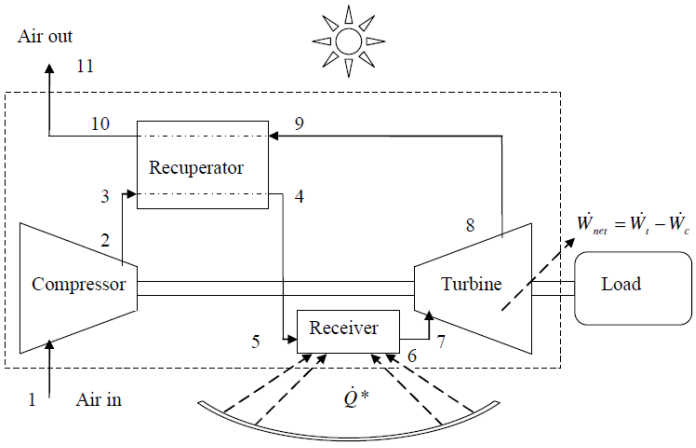

Figure 6: The open and direct solar thermal Brayton cycle with recuperator optimised by Le Roux *et al.* 2011

The tubular receiver employed by Le Roux *et al.* (2015) changed between the optimization study and the experimental setup. This was based on a receiver efficiency study which found that for the same cavity aperture and

insulation thickness the cavity geometry has almost no effect on the system efficiency (Le Roux *et al.* 2014). Furthermore, a coiled receiver at the operating temperatures required to power a solarised Brayton cycle is flexible to some extent which reduces the mechanical stresses. The modified HPAR does not incorporate a coil and has to accommodate for the thermal stresses in another way. The ability of the external fins and the induced flow to improve the differential circumferential expansion needs to be investigated in the testing.

Craig *et al.* (2015) presented a CFD analysis of a parabolic dish tubular cavity receiver. The findings were validated by the experimental receiver of Le Roux *et al.* (2015). Most notably the CFD analysis solved the Radiative Transfer Equation (RTE) using a Finite Volume (FV) method by employing the Discrete Ordinates (DO) method to solve the optical performance of the dish and receiver, from there the absorbed radiation is patched as a volumetric heat source onto the receiver. With this patch, a second FV simulation is carried out to solve the heat transfer to the internal fluid and heat losses from the cavity insulation.

Craig *et al.* (2013a) used this method to generate a 3-D simulation of the HPAR in which tube geometry layout optimisation was attempted. The objective function aimed to maximise the heat transfer between the incoming solar radiation and the heat transfer fluid. The problem of non-uniform external fluid flow which results in non-uniform heat transfer in the receiver was illustrated in that study. Another aspect relevant to this study was the complexity of the header system required. A simple to manufacture and effective header system is required. This method of Craig *et al.* (2013a) is considered computationally very expensive and the complex geometry of the modified HPAR increases the computational expense several times, highlighting the need for reliable experimental data with which to validate such a simulation.

From the SUNSPOT cycle originated another tubular receiver concept called the SCRAP (Spiky Central Receiver Air Pre-heater) receiver (see Figure 7 and 8). This receiver employs a number of novel central receiver concepts, yet it does not address the bottleneck problem inherent in the SUNSPOT cycle. The receiver uses a multitude of internally finned tubes in a semi spiked ball assembly (Lubkoll 2017). The spike concept is aimed at trapping incident solar radiation in the depth of the receiver by reflecting incident solar radiation to the tube bases.

During operation, the highest temperatures are expected to exist at the spike tips, in a bid to deal with the extreme fluxes jet impingement cooling is employed to reduce the tip temperature drastically. This heat removal serves a dual purpose, firstly it enables metal heat exchangers to be operated in higher incident flux than previously possible and secondly, it reduces the surface temperature of the components with the largest view factor to the environment thereby reducing potential radiative losses. Lubkoll (2017), predicted solar to thermal efficiencies exceeding 80 %.

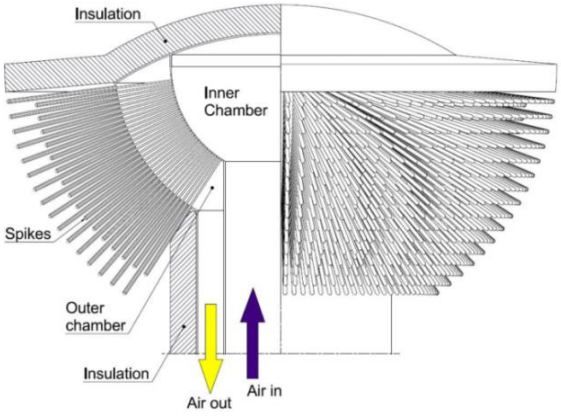

Figure 7: The SCRAP receiver concept (Lubkoll, 2017)

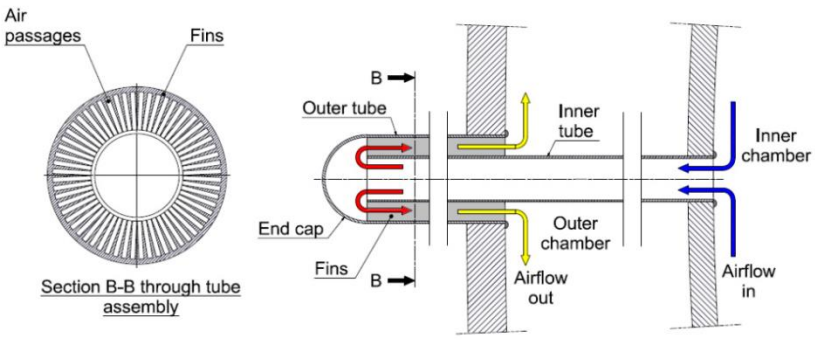

Figure 8: Internally finned SCRAP tube geometry (Lubkoll 2017)

The SCRAP receiver has drawbacks in terms of functionality in a commercial application. The absence of a cavity leaves the receiver extremely vulnerable to large convective losses during windy days. The aspect ratio of the tubes to the incident radiation leads to low wall fluxes on the length of the tubes compared to the tip. Manufacturability is

problematic from a cost and assembly point of view. Controllability of a full field application requires a complicated manifold system.

2.6.4. Volumetric receiver

Research and development of new receivers set out design goals such as simple, cheap and higher collection efficiency with better thermal properties. The development of volumetric receivers favoured smaller aperture size to minimize heat loss, thereby allowing even higher solar flux compared to tubular receiver technologies according to Ávila-Marín (2011).

The basic principles of volumetric receivers are:

- A multitude of porous shapes and foams made of metal, ceramic or other adequate materials allowing the concentrated radiation to be absorbed in the depth of the structure (Ávila-Marín (2011)).
- Concentrated solar radiation heats the material and at the same time a HTF passes through the heated volume subsequently heating up by forced convection.
- The true measure of a volumetric receiver is the ability to achieve the volumetric effect (achieve a higher outlet HTF temperature than the surface temperature on the irradiated side).

There are two main types of volumetric receivers namely open and closed volumetric receivers. The difference being a closed volumetric receiver has a quartz glass window at the aperture allowing the fluid to be pressurised. Figure 9 demonstrates the difference between tubular receivers and volumetric receivers and the HTF thermal development.

The addition of the quartz window and elevated pressure increases the heat transfer to and obtainable temperatures of the HTF by reducing radiative losses and increasing the fluid density. There exists a limit on the size of the quartz glass window and the allowable cavity pressure permitted by the glass.

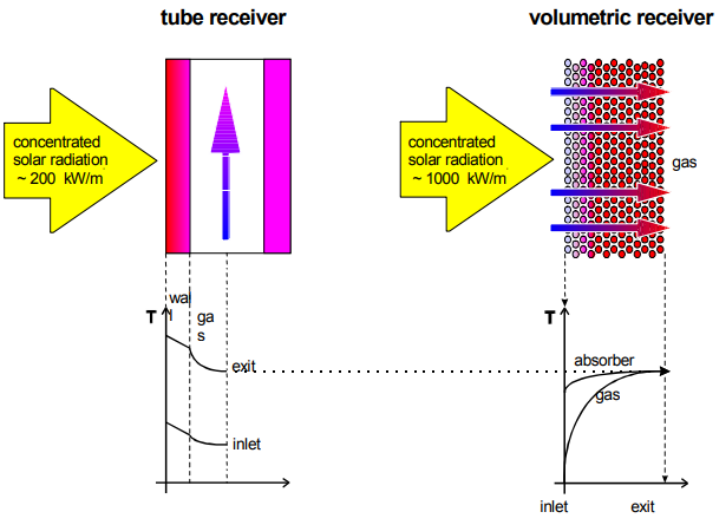

Figure 9: Comparative schematic of tubular and volumetric receivers (Fend 2012).

In an open volumetric receiver, atmospheric air is heated and will typically be used in a Rankine cycle where the air is fed to a steam generator. Closed volumetric receivers allow for integration with a Brayton cycle and combined cycle systems. As mentioned earlier the non-pressurised side of the modified HPAR is an open volumetric receiver and the objective of this study is to investigate the effectiveness of the external fins to increase the open volumetric side heat transfer. The experimental work needs to provide insight into the collector capabilities while overcoming the challenges of volumetric receivers.

2.7. Heat transfer enhancements for tubes

Heat transfer enhancements can take several forms and a great deal of research has been done on the improvement of heat transfer to and from solids and fluids. In this section a summary is done of the most relevant enhancements for tubular cavity receiver heat transfer based largely on a review by Siddique *et al.* (2010). Enhancements are divided into two sub-categories namely active and passive enhancements.

For the modified HPAR in this investigation, only external enhancements are used. The addition of passive internal enhancements such as wire coil inserts is an attractive solution which can potentially reduce the thermal gradients further.

According to Siddique *et al.* (2010) the mechanisms to enhance heat transfer can be any of the following:

- Addition of secondary heat transfer surface.
- Disrupting an unenhanced fluid velocity.
- Disrupting the laminar sublayer in a turbulent boundary layer.
- Secondary flow introductions.
- Boundary-layer separation.
- Delaying boundary layer development.
- Increasing of the temperature difference between the fluid and surface.
- Increasing the fluid velocity with passive methods.

2.7.1. Passive internal enhancement

Passive heat transfer enhancements refer to obstructions or surface alterations made which require no external input to enhance the heat transfer. Good heat exchanger design is driven by maximisation of efficient thermodynamic performance by promoting minimum entropy generation or minimum exergy destruction.

The most notable internal flow passive heat transfer enhancement is the addition of a wire coil insert to trip the flow and break the boundary layer. Grooves, spirals and dimples can produce similar effects, but the enhancement compared to the pressure loss needs to be investigated for the flow conditions and evaluated against the system requirement (Dewan *et al.* 2004).

2.7.2. Active internal enhancement

Active heat transfer enhancement requires an external power input to agitate the fluid. Examples of active enhancements are induced pulsation by reciprocating plungers or a magnetic field which disturbs the flowing stream (Dewan *et al.* 2004).

2.7.3. External enhancements

External heat transfer enhancements are commonly implemented in fluid-gas heat exchangers such as condensers. As with internal heat transfer enhancements, the heat transfer is increased by increasing the surface area. External fin addition to the tubes is a passive heat transfer enhancement. The use of external fins in an attempt to increase the volumetric effect was investigated analytically by Heller (2017) since it has

the potential to increase the outlet temperatures of the non-pressurised stream. The induced flow into the cavity of the modified HPAR is regarded as an active enhancement.

2.8. Past work done on the HPAR

As discussed in section 1.1.2. the HPAR concept was proposed and developed by Kretzschmar (2014). In the original rendition, copper tubes were used with no internal fluid in the experimental manifestation. The tubes were arranged in a staggered pattern which allowed the use of tube bank flow approximations to model the external fluid flow. A layout similar to the optimisation layouts by Craig *et al.* (2013a), which allows the rays to penetrate deeper and support the volumetric trapping capabilities, should be used instead.

During the simulation of the SUNDISC cycle development by Heller the HPAR was identified as a possible substitute for the use of two receivers. Heller estimated that the SUNDISC cycle will need to obtain 38 % of the required thermal energy from the pressurised air stream in the HPAR. This value was used to determine the fractions of heat transfer to the non-pressurised and pressurised air streams that the modified HPAR had to obtain if it is to replace two independent receivers. These fractions thus serve as a design benchmark for full-scale HPAR development and operation.

The HPAR has the unique ability to change the heat transfer ratio to the two streams by changing the operating conditions. This feature enables the system to theoretically operate at the highest system efficiency throughout the day. By shifting the energy distribution ratio between the two streams the Brayton cycle can be run at nominal operating point whilst the TES absorbs the difference. This controllability is investigated in the experimental results in Chapter 6.

Heller investigated the potential heat flux distribution and the outlet temperature of finned tube bundles analytically. For this, a simplified model for heat transfer on finned tubes in bundles has been developed based on correlations by Schmidt (2010). The model was directly dependant on the geometry and temperature assumptions made. In Chapter 4 the theory, assumptions and limitations of such a model is discussed.

Theoretical simulation of the HPAR suggested that even though the pressurised air (PA) requirements could be satisfied, the desired non-pressurised air (NPA) temperature could not be achieved declaring the NPA energy harvested in essence useless for cycle integration. Heller set forth to find possible solutions for this in three main forms namely: the addition of external fins on the tubes, the addition of quartz prisms or windows and the addition of a volumetric receiver at the back of the cavity.

The addition of fins indicated a drastic increase in the heat transfer to the non-pressurised air stream in comparison to un-finned tubes under the assumptions used by Heller (2017). The ability of the fins to trap the incident radiation was illustrated by a ray tracing simulation in Fluent where fin height of 20 mm and an unblocked tube length of 4mm resulted in a view factor of less than 5 % from the base tube to ambient according to Heller (2017). In section 3.5.2., a similar study was undertaken in the fin geometry selection process.

The model by Heller (2017) did however not account for higher absorption of solar radiation per row due to the increased effective diameter of the finned tube. To maintain the penetration of the solar radiation, the tubes in a row had to be spaced further apart, which in turn increases the view factors to ambient and decreases the effectiveness of the forced convection on the finned tubes. The non-pressurised air outlet temperature with this adapted geometry was considerably lower than in the other configurations.

The HPAR model by Heller (2017) used a cavity height of 2 meters which is quite large relative to tube diameter forming large vertical areas between the tubes. This can reduce the effectiveness of the induced flow significantly at low mass flow rates. The addition of separation plates or a smaller modular cavity needs to be considered to ensure the HPAR can indeed capture the convective losses.

The configuration in the simulation favoured the smallest fins required to achieve the desired pressurised air outlet temperature and the convective heat flux to the non-pressurised air stream. This limits the heat transfer to the non-pressurised air stream since the main goal is to heat the internal air.

Assuming that the fins do not affect the heat transfer on the inside of the tubes, the convective heat transfer to the pressurised air stream was only

adjusted by the increase in number of columns. Heller showed analytically that the implementation of external fins has the potential of satisfying the outlet conditions of the non-pressurised air stream. This will increase the receiver thermal rating by achieving higher temperatures.

The geometries of the finned tubes were crucially simplified for all radiation calculations to a tube with the effective outer diameter of the fin. This applied to the influx distribution and the view factor determination between surfaces. No micro-cavity effect of the fins could therefore be considered for radiation heat transfer. This assumption leads to false absorption and convection quantities which may lead to an overestimation in results. The same approach was used in Appendix H to model the modified HPAR tested in this investigation and it was found to overestimate the thermal response.

Both the addition of quartz prisms and a volumetric absorber theoretically show promising improvements. Heller (2017) estimated that the surface temperature of the first tube row can be kept below 600 °C which reduces the radiative losses, resulting in a receiver efficiency of up to 78 %. However, neither of the streams could achieve the desired design outlet temperatures at the same time. Should any or all of these improvements be used the manufacturability and cost competitiveness needs to be investigated and compared to using two independent receivers.

The experimental receiver in this investigation sets forward to try and assess the effectiveness of the fins and induced air to reduce the circumferential thermal gradient. The overall volumetric effectiveness and penetration depth is to be inspected as a secondary objective. And lastly, the ratio of harnessed energy between the two fluids at varying receiver efficiencies is to be determined.

2.9. Material considerations for solar receivers

Solar receivers are subjected to high non-uniform heat fluxes on a daily basis and thermal shock during periods of intermittent solar irradiance. This requires much consideration when selecting a receiver material. The material needs to possess a high creep limit to ensure a long working life under repeated thermal cycling. Heat transfer fluid temperature is directly related to surface temperature and therefore the higher temperature variation the chosen material can handle the better. Further, the material

needs to have good thermal properties, both thermally conductive and limited thermal expansion to reduce the effect of cyclic thermal stresses.

As mentioned in section 2.5.3 tubular receivers are prone to thermal stresses due to non-uniform circumferential temperatures. In the material considerations done by Heller (2016) Inconel 601 tubes were chosen as suitable material for tubular receivers based on the thermal properties.

Inconel is a family of austenitic nickel-chromium-based super-alloys which can sustain temperatures of up to 950 °C safely under pressure enabling high HTF temperatures. Further, it has a high melting point and low thermal expansion. Inconel alloys are oxidation- and corrosion-resistant materials well suited for service in extreme environments subjected to pressure and heat. Inconel is however expensive and a relatively poor thermal conductor with a thermal conductivity about 4-5 times less than that of carbon steel.

The high cost is one of the main driving factors behind the research into heat transfer enhancement of tubular heat exchangers. By increasing the heat removal from metal tubes the permissible flux intensity can be increased. The lower material cost, comparative ease of manufacturing and a higher thermal conductivity value of less exotic steels make it an attractive alternative if the thermal boundaries can be overcome.

This study is aimed at investigating the enhancement effectiveness to remove heat from the foremost tubes in the tubular receiver. The findings will contribute to the existing body of knowledge of high-temperature and high-flux metal heat exchangers.

2.10. Conclusion on literature review

Several aspects of the proposed receiver design have been reviewed. The first aspect was the limitations and advantages of air as working fluid. Air is a poor thermal transporter with low thermal capacity and low thermal inertia compared to liquids. Research has been carried out in the past to try and accommodate for these limitations. The past literature have been summarised in section 2.2 and 2.5. It seems that the general findings in early research were that air in a volumetric receiver has the potential to power such a cycle and that tubular receivers cannot obtain the required temperatures and mass flow rates.

In more recent studies the use of tubular air receivers has seen some renewed interest. This stems from the interest to use a solarised air Brayton cycle which requires pressurised air to be used as HTF. As a result, a cost-effective alternative to closed volumetric receivers is sought. In section 2.5 some other significant work was mentioned with the SOLHYCO project being the most notable attempt in recent times. The innovative design of SOLHYCO seems to be able to satisfy the goals to some extent. Tubular receivers however still lag behind open and closed volumetric receivers in terms of allowable incident flux intensity.

In section 2.6 the methods pursued to enhance tubular receivers are briefly reviewed. Both internal and external passive heat transfer enhancements show significant promise when optimised for the desired application. The problem faced by tubular solar receivers is an external heat management problem. A solution that can control the circumferential temperature distribution and thereby reduce thermal stress during cycling will improve the capabilities of tubular receivers for gasses greatly. The work done in this study aims to contribute to this body of knowledge.

This study flows from previous numerical studies in a bid to validate the enhancements suggested by Heller (2017) for the receiver proposed by Kretzschmar (2014). The validity of the modelling assumptions made is to be questioned using the results from the experimental modified HPAR.

Chapter 3

Design decision

The literature review was carried out with the goal of assisting the development of the experimental geometry. The objective of the receiver is to generate empirical data with which suggestions in previous studies can be investigated. To achieve this objective the receiver needs to be instrumented to provide data with reasonable accuracy and spatial resolution with which future models can be validated and assumptions verified.

Based on the literature review a generic design was compiled from the promising concepts. This chapter covers the assumptions made and the literature tie to the design manifestation.

3.1. Specifications

Most of the assumptions from literature are applicable to the modelling and not the experimental design since there are limited published experimental works similar to this receiver. The design was carried out with strong simulation and literature influenced decisions allowing the assumptions to be evaluated.

The design is a combination of the work done by Craig *et al.* (2013b), Kretzschmar (2014) and Heller (2017) and the 1-D steady-state simulation work. The theory and modelling approach is discussed in Chapter 4 and Appendix H.

A cavity with an included angle of 30° was chosen. This decision allows the receiver to be duplicated to form a 360° receiver for full field application, similar to the numerical work by Heller (2017). The cavity and aperture size can increase the convection trapping effectiveness of the induced flow at low flow rates, a possible solution to the problem pointed out in the geometry investigated by Heller (2017). It is assumed that this receiver can be used in a modular fashion. In future work, a 3-D model, validated by the findings of this investigation, can be used to estimate the performance of a 360° version by discretizing the full field into 12 sections.

Based on the findings by Heller (2017) it appeared that the HPAR cannot achieve the desired outlet conditions in one pass, however, small modular receivers in series may be able to reach the desired conditions. The experimental receiver was designed for the Helio40 field where most of the mirrors are close to perpendicular to the tower. The included angle of the cavity is expected to contribute to the heat transfer to the non-pressurised air by increasing the flow rate towards the back of the receiver.

The additions of fins, as discussed earlier, stem directly from the simulation work performed by Heller (2017). Heller approximated the fins as tubes with the same diameter as the fin tips, an approximation which avoids the micro-cavity effects. The same modelling approach was undertaken in order to compare the results to the experimental results to address the validity thereof.

The geometry of the fins was chosen based on estimations and limitations discussed later in this chapter. Three tube geometry layouts were generated and evaluated instead of doing an optimization study similar to that of Craig *et al.* (2013a).

3.2. Limitations

Due to manufacturing constraints and material restrictions in the finned tube market, it was decided to machine the fins from hollow bar instead of welding hundreds of external fins to stainless steel or carbon steel tubes. Welding would potentially lead to an increase in thermal resistance between the fin and the base tube. For the purpose of this study, the specific fin geometry was optimised within the manufacturing limitations.

In the intended environment, the fin tip is expected to be at the highest temperature and has to conduct the heat to the base tube resulting in the most expansion at the tip. By machining the fins from hollow bar it was ensured that thermal contact with the base tube is kept. The unidirectional heat flux from the incident solar radiation increases the circumferential thermal stress which can potentially further decrease the thermal contact between the fins and the base tube in the case of welding.

The chosen hollow bar has an outer diameter (OD) of 36 mm and an inner diameter (ID) 16 mm. For structural integrity, a wall thickness of at least 2 mm was chosen for the ‘base tube’. This wall thickness constraint implies that the maximum fin height is limited to 8 mm. The eventual

machined fins formed radial discs on the tubes. The fin geometry is depicted in Chapter 5.

3.3. Physical setup

In Appendix A the generated geometries are evaluated and the methods connect employed discussed. The final cavity geometry is depicted in Figure 10 at the end of this section. The x's indicate the location of the tubes where the temperature readings were taken. Radiator hoses are used to the manifolds in the desired flow path. An in-line water pump is used to circulate the water through the receiver at a low flow rate ($<6\ \ell/\text{min}$). This low flow rate, provided by the pump, ensured a large enough temperature gain in the water over the receiver to improve measurement accuracy. To reduce the water usage, a closed water loop incorporating a radiator to cool the water down to the desired inlet conditions was used. The experimental setup is discussed in Chapter 5. The heliostat field layout and characterisation can be found in Appendix E.

The water internal to the medium carbon steel tubes is expected to form a layer of oxidation which will reduce the internal heat transfer thus leading to higher tube surface temperatures than that of the simulated model. Fouling is one of the largest contributors to heat exchanger capacity reduction and effort is made to avoid this. However, for the purpose of this study, it will lead to an increase in the measured temperatures of the surfaces and therefore increase the thermal measurement accuracy. Testing was preceded by a period of commissioning during which the onset of fouling was expected to stabilise. The tests were all conducted within a relatively short period of time ensuring similar conditions.

The machined tubes were left untreated and surface oxidation was expected to form. Generally reflection is a major contributor to losses in solar receivers, however, in this iteration of the modified HPAR the reflection from the tubes was expected to in fact enhance the penetration depth. Table 2 compares the results of the ray tracing for different reflectivity values of the receiver. The simulated difference between the absorbed energy for painted and unpainted tubes supported the decision to not paint the surfaces.

A study by Yellowhair *et al.* (2015) at Sandia National Laboratories where the effect of staggered geometries and oxidation on increased light trapping

and effective solar absorptance was investigated supported the decision to leave the tubes untreated. The study concluded that the effective solar absorptance relative to a flat plate with an intrinsic material absorptance of 86 % could be increased to 92 % by geometry enhancements similar to the ones employed in the modified HPAR.

Table 2: Absorbed energy at the deepest tube for different surface coatings

Coating	Reflectivity (The Engineering toolbox 2018)	Power absorbed (W)
Pyromark 2500	0.05	103.86
Machined iron	~0.70	191.94
Oxidised iron	~0.30	118.62

The effect oxidation has on the receiver in the solar radiation spectrum is of concern. More diffuse oxidised surfaces have increased absorption and therefore increased harnessed energy. This is at the cost of reducing the penetration depth of the reflected solar radiation. The oxidation can be seen in Section 6.3.1, a visual inspection of the extent of the oxidation was performed after the environmental exposure during the testing.

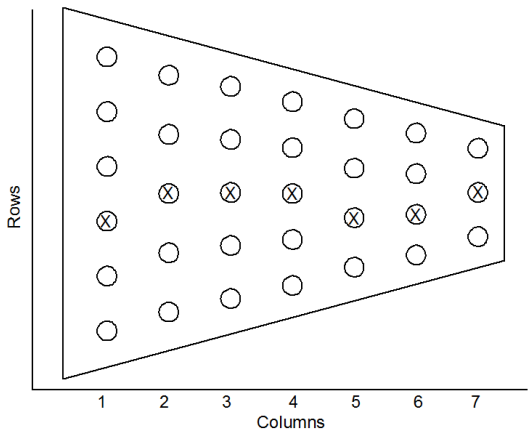

Figure 10: Cavity layout

3.4. Theoretical setup

A MATLAB model was implemented to characterise a portion of the experimental setup based on a list of assumptions. This MATLAB algorithm solves the tube surface-, internal fluid- and external fluid temperature as outputs for the chosen approximation of the receiver. This

model, which can be found in Chapter 4 and Appendix G&H, uses similar theory and assumptions as Heller (2017) and Kretzschmar (2014).

The MATLAB theoretical simulation model includes conduction and convection heat transfer as well as radiation losses to the ground via view factor implementation. This model was used to predict system behaviour for variations in the fin height, spacing, tube length, and internal fluid path. Lastly, a model to compare the effect of two different internal heat transfer media was generated. The model accuracy and assumption validity was evaluated using the experimental results for water as internal fluid. The model validity evaluation can be found in Appendix H.7.

Heat transfer correlations from A.F. Mills *et al.* (1999) and Çengel *et al.* (2015) were used to describe and quantify the heat transfer mechanisms in the test problem. Figure 11 below illustrates the simulated layout onto which the view factors and estimated flow rates of the full receiver are projected. The layout of Figure 11 can be propagated 360° to form a full field receiver. The relative position is incorporated in the view factor to the environment.

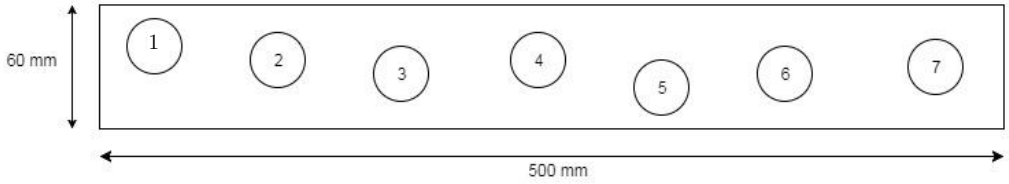

Figure 11: Geometry layout of the analytical model used in MATLAB

3.5. Design simulation work

This section covers the work done and the methods employed to evaluate the different design iterations. All of the evaluation simulations in this section was performed in ANSYS 18.2 and based on the assumptions of published works reviewed in Chapter 2. These were investigative simulations and not full-scale system response estimations. The findings of the simulations are discussed in Appendix A.

3.5.1. Assumptions

Based on the paper by Grobler, (2015) the Helio40 installation can achieve an average heat flux distribution of 30 kW/m^2 with good aim strategies

during the summer months. This value was used to evaluate the performance in terms of radiation penetration of the generated designs. For the penetration modelling of the incident radiation, the computationally expensive Discrete Ordinates radiation model of ANSYS fluent was used. In an attempt to reduce the computational times the geometry was simplified to 2-D tube layout (Appendix A).

A directional radiation of 30 kW/m^2 was applied to the inlet boundary of the cavity, assuming all incident radiation is parallel from the small heliostat field. For a reliable flux mapping in the 2-D cavity, the DO model was discretized into 180 angular divisions at each impact. This process was repeated for all the generated geometries after which the incident radiation on the tube columns was compared.

The resulting flux distributions can be seen in Appendix A. The next objective was to do a Finite Element analysis of the tubes at the temperature loads to check the structural integrity. This is important in the case of internal pressure. The process is briefly discussed in Appendix B.

3.5.2. Radiation penetration/trapping

The radiation penetration of the three generated layouts, presented in Appendix A, was compared to one another. The macro volumetric/cavity effectiveness to trap radiation was evaluated for the layouts. The depth of penetration and quantity absorbed by the tubes was the measure of effectiveness as discussed in Appendix A.

The next step was to investigate the micro-cavity effect of the fin addition. The measure of radiation trapping capability was the view factor from the base tube to the environment. The incident radiation rays are assumed to be parallel to the fins and therefore the spacing doesn't impede penetration. The surface of the base tube is assumed to reflect and radiate diffusely, for this the view factor becomes a significant factor. A lower view factor to the environment, therefore, enables the fins to trap more heat radiation.

For the fin spacing study, finned tubes with 3 mm, 4 mm and 5 mm spacing were generated and the view factor evaluated using the S2S radiation model of ANSYS 18.2. These different fin spacing were

determined by the available parting tool sizes at the workshop. The resulting view factor to ambient for each is listed in Table 3.

Table 3: View factor from the base tube for different fin spacing

Fin spacing	View factor
3 mm	0.042156
4 mm	0.059476
5 mm	0.067257

Manufacturing constraints resulted in 1 mm fin thickness. Thinner films will possibly increase convective heat transfer and thicker fins conductive heat transfer since thicker fins have a larger cross-sectional area for conductance. The heat transfer to the internal fluid is the main objective of the modified HPAR and therefore the 4 mm spacing was chosen given that it is a trade-off between penetration area (spacing vs fin thickness) and low view factor. Too small spacings will decrease the thermal losses by decreasing the view factor of the radiative losses from the base, at the cost of decreasing the radiation penetration.

The view factor of a chosen fin spacing can be reduced by increasing the fin height. The flow velocity of the air through the fins and therefore the convective heat transfer is dependent on the fin spacing and therefore needs to be taken into account when performing the radiation penetration investigation. Taller fins would require the flow to penetrate deeper and travel further between the fins. This can potentially become a problem when the fin height to spacing ratio is high since relatively low flow velocities are experienced in the modified HPAR. Boundary layer thickness and flow displacement increase as the flow rate decreases. This growth of flow displacement thickness forms a flow restriction which reduces the convective heat transfer between the fins.

A quick estimation of boundary layer growth and displacement thickness for laminar flow over a flat plate can be performed with the Blasius boundary layer solution (Çengel 2014). The displacement thickness can be found by integrating the Blasius solution Eq. 2 to find Eq. 3.

$$\delta = \frac{4.91x}{\sqrt{Re_x}} \tag{2}$$

$$\delta^* = \frac{1.72x}{\sqrt{Re_x}} \tag{3}$$

3.5.3. Temperature distribution on a tube

Tube temperature distribution was approximated in the simulated theoretical model as well as in a simulated static thermal analysis carried out in ANSYS 18.2. This was done for worst case scenario boundary conditions to predict failure modes and establish safety margins during operation.

The 1-D model produces a mean tube temperature for the circumference of the control volume. Using a Fourier series approximation for the circumferential incident radiation the 1-D surface temperature can be extended to a 2-D surface temperature analysis. The more accurate 2-D analysis is however still not as accurate as a 3-D approximation.

3.6. Conclusion on design decisions

Several factors were assigned different weights in the receiver design process. The objective of this study is to provide empirical data to address and assess the suggestions and assumptions made by previous studies and provide data with which future work can be validated.

Other factors that weighed in on the eventual design included material and manufacturing constraints, cost and the results of the various investigative design simulation work done. As a result, the modified HPAR in this study incorporates various suggestions from past HPAR related work and some new features such as the layout and manifold system.

The simulation and comparison of different layouts are discussed in Appendix A. The fin spacing decision was based on the manufacturing constraints and selected based on the view factor from the base to the environment.

Chapter 4

Theory

The following chapter covers the theory used to develop an analytical model of the receiver. Several model variations were created based on different assumptions. These conservative 1-D models, discussed in this chapter and Appendix H, are used to quantify the expected temperature response during operation. All of the models were used as design tools. Using these models the receiver sensitivity to various factors are demonstrated and the design evaluated.

The experimental receiver operates at changing conditions and rates which are measured and used to evaluate the theoretical model accuracy. Once validated, the model can be used to make more accurate predictions of the behaviour of similar systems.

4.1. Mathematical equations

The following section covers the mathematical correlations used to estimate the system response. Several assumptions and approximations were made to generate this theoretical model representative of the receiver test setup. The models are based on and adapted from the simulation done by Kretzschmar, (2014), Duffie *et al.* (2006) and Heller (2017).

In order to characterise the thermal behaviour of the receiver in question an energy balance, focussing on the following energy transfer mechanisms needs to be solved:

- Solar radiation absorption and reflection
- Internal forced convection to the internal fluid stream
- External forced convection from the tube and fin surface to the air stream
- Radiation heat transfer between the tubes, fins and the sky.
- Conductive heat transfer in the metal tube and fin circumference

The assumptions based on which the simulation was carried out are listed in Appendix H.

4.1.1. Conductive heat transfer

Conductive heat transfer through a tube wall occurs in the axial, radial and circumferential direction. The assumptions employed in the 1-D simulation only accounts for conduction in the radial direction, the other two directions are assumed in equilibrium. This is important to note since one of the research objectives is specifically investigating the circumferential temperature gradient. Axial conduction would increase the model to 2-D and circumferential conduction to 3-D. Each added dimension increasing the complexity significantly. This is the main driving force behind the 1-D simulation implementation.

Conductive heat transfer is calculated from Fourier's law of heat conduction.

$$\dot{Q}_{\text{cond}} = -k_{\text{tube}}\, r\, \frac{d}{dr}\left(r\frac{dT}{dr}\right) \tag{4}$$

The boundary area of the solid over which the conduction occurs is denoted as A. The thermal conductivity k of the material is evaluated at the surface temperature at the midpoint of the tube height in question.

4.1.2. Convective heat transfer

Convective heat transfer is the largest contributor to heat loss/transfer at lower temperatures when compared to that of radiative heat transfer. Convective heat transfer is characterised by the fluid conditions over a body and can be grouped into sub-divisions which all employ the same theory with variations. Convective heat transfer is characterised by Equation 5

$$\dot{Q}_{\text{conv}} = h\,\text{A}\,(T_{\text{s}} - T_{\text{f}}) \tag{5}$$

The sub-divisions are natural convection, external- and internal forced convection. As the names stated internal forced convection occurs inside ducts and external forced convection occurs by induced flow over a surface. Natural convection is driven by the buoyant flow of heated gas that rises from a surface creating a flow circulation of cooler more dense fluid moving into the resulting space. In this investigation, the induced flow is assumed to negate the effects of natural convective flow as was

demonstrated by Kretzschmar (2014). Therefore only internal and external forced convection is modelled.

The heat transfer coefficient is a function of the thermal conductivity of the fluid (k), the flow conditions over the surface (Re and Pr) and the characteristic length (L) travelled along the surface. The Nusselt number (Nu) is commonly used as the non-dimensional form of the heat transfer coefficient.

$$Nu = \frac{hL}{k} \tag{6}$$

4.1.3. Radiative heat transfer

Air as HTF is completely transparent and as a result, does not participate in radiative heat transfer. Heat loss from surfaces at elevated temperatures by means of radiation is a major contribution to losses of central receivers. The radiative heat transfer from a surface is dependent on the surface characteristics of absorptivity, reflectivity and transmissivity.

Radiation between two objects is characterised as a function of the view factor f_{ij} between the objects, the emittance ε, the Stefan-Boltzmann constant σ and the 4^{th} order temperature differential. From Eq. 7 it can be deduced that the radiative heat transfer can be reduced by reducing the view factor and reducing the temperature difference.

$$\dot{Q}_{\text{rad}} = \varepsilon f_{ij} \sigma \text{A}(T_1^4 - T_2^4) \tag{7}$$

The net heat flux on a surface receiving solar radiation can be formulated by a surface energy balance presented in Eq. 8.

$$q = \varepsilon E_{\text{b}} - \alpha_{\text{s}} G_{\text{s}} - \alpha G \tag{8}$$

Where G_s is denoted as the solar radiation, the irradiation term G includes all the radiation from the sky and other objects and E_b is the emitted radiative losses from the surface.

In the case of the experimental receiver tested the receiver cavity is angled 25° below horizontal. This rotation effectively looks at the heliostat field and therefore a radiative heat loss to the environmental temperature would be a more accurate representation. The environmental temperature is assumed to be the same as the ambient temperature.

4.1.4. Tubular concentrated solar energy collector approximations

The following section covers the theory from Duffie *et al.* employed by Kretzschmar (2014). It was expanded in this investigation by manipulating the surface areas to account for the use of finned tubes.

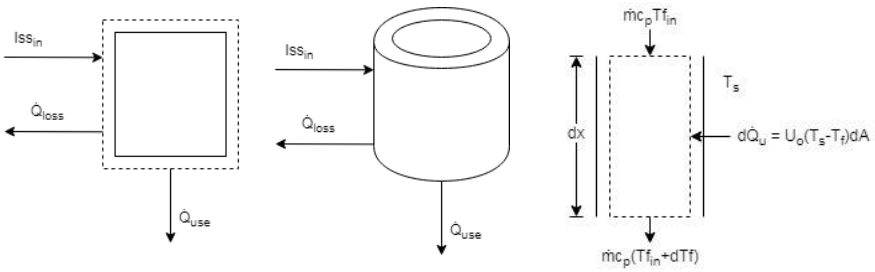

Figure 12: Control volumes with external energy balance (left and centre) and Control volume of the internal energy balance and energy transfer (right) (Basson *et al.* 2018)

For a 1-D model, the energy balance on the control volume is summed as the left diagram depicts in Figure 12 with the solar irradiance flowing into the control volume and the losses out. This control volume energy balance formulation is based on published work (Kretzschmar, 2013, Duffie *et al.,* 2006). The energy transferred to the internal working fluid is termed the used energy since it is transported over the control volume boundary from one control volume to the next and in that sense lost/used.

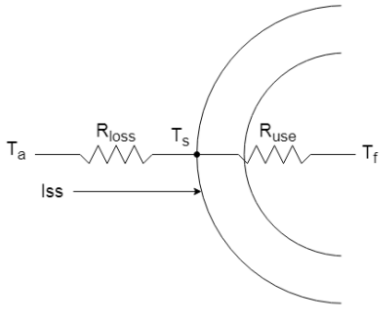

Figure 13: Global thermal resistance diagram (Basson *et al.* 2018)

The heat loss term is a function of the temperature difference between the tube surface and the air flowing over it. An overall loss coefficient is approximated to represent the convective and radiative losses as one term.

The incident solar radiation (Iss) intensity is the net incident radiation absorbed on the surface based on the assumed surface absorptance and

reflectance. In Appendix H the determination of Iss intensity for the various models is discussed.

$$\dot{Q}_{\text{use}} = A_{\text{t}} Iss - \dot{Q}_{\text{loss}} \tag{9}$$

$$\dot{Q}_{\text{loss}} = U_{\text{loss}} A_t (T_{\text{s}} - T_{\text{a}}) \tag{10}$$

$$\dot{Q}_{\text{use}} = A_t [Iss - U_{\text{loss}} (T_{\text{s}} - T_{\text{a}})] \tag{11}$$

$$\dot{Q}_{\text{use}} = U_{\text{int}} A_{\text{t}} (T_{\text{s}} - T_{\text{f}}) \tag{12}$$

The equivalent heat transfer resistance to the internal fluid is defined as an overall heat transfer coefficient to the internal fluid:

$$U_{\text{int}} = \left[\frac{D_{\text{o}}}{h_{fi} D_{\text{i}}} + \frac{\left(D_{\text{o}} \ln \left(\frac{D_{\text{o}}}{D_{\text{i}}} \right) \right)}{2k} \right]^{-1} \tag{13}$$

The internal heat transfer coefficient for heating fluids is calculated with the Dittus Boehlter equation based on developed internal pipe flow correlations:

$$Nu = 0.023 Re^{0.8} \text{Pr}^{0.4} \tag{14}$$

Nu for Re<2300 was taken as 4.63.

The internal fluid heat transfer coefficient can be obtained using the Nusselt number.

$$h_{fi} = \frac{kNu}{D_i} \tag{15}$$

Substituting Eq. 12 into Eq. 11 and simplifying

$$\dot{Q}_{\text{use}} = A_{\text{t}} \left[Iss - U_{\text{l}} \left(\left(\frac{\dot{Q}_{\text{use}}}{U_{\text{int}} A_{\text{t}}} + T_{\text{f}} \right) - T_{\text{a}} \right) \right] \tag{16}$$

$$\dot{Q}_{\text{use}} = A_{\text{t}} F' [Iss - U_{\text{l}} (T_{\text{f}} - T_{\text{a}})] \tag{17}$$

F' was termed the collector efficiency function by Duffie *et al.* (2006). This function can be used as a measure of collector heat transfer efficiency with which collector geometries can be compared directly. The terms used in the formula, in this case, are applicable on tubular receivers.

$$F' = \frac{\frac{1}{U_l}}{\frac{1}{U_l} + \frac{D_o}{h_{fi}D_i} + \frac{D_o \ln\left(\frac{D_o}{D_i}\right)}{2k}} \tag{18}$$

The energy transported into and out of the control volume in Figure 12 (right) is presented by Eq. 19. The energy balance is simplified by integrating along the control volume. Using the inlet and outlet boundary conditions of temperature the simplified equation is found (Eq. 22).

$$\dot{m}c_p\left(\frac{dT_f}{dx}\right) = F'\left(Iss - U_l(T_f + T_a)\right)\pi D_o \tag{19}$$

$$\int \frac{1}{\left(\frac{Iss}{U_l} + T_a\right) - T_f} dT_f = \int \frac{F'\pi D_o U_l}{\dot{m}c_p} dx \tag{20}$$

$$T_f(x)|_{x=L} = T_{fo} \tag{21}$$

This simplified equation allows one to determine the internal fluid temperature gain with no knowledge of the surface temperature.

$$T_{fo} = -\left[\left(\frac{Iss}{U_l} + T_a\right) - T_{fi}\right]\exp^{-\frac{F'\pi D_o U_l x}{\dot{m}c_p}} + \left(\frac{Iss}{U_l} + T_a\right) \tag{22}$$

Alternatively, it can be written as:

$$T_{fo} - T_{fi} = \left[\left(\frac{Iss}{U_l} + T_a\right) - T_{fi}\right]\left\{1 - \exp^{-\frac{F'\pi D_o U_l x}{\dot{m}c_p}}\right\} \tag{23}$$

The next step is to determine the energy transported out of the control volume by the internal flow. The energy transported is evaluated at the inlet conditions. This approximation is sufficiently accurate for small control volumes since the temperature gain is small and the average therefore close to the initial temperature.

$$\dot{Q}_{use} = A_t F_R[Iss - U_l(T_{fi} - T_a)] \tag{24}$$

F_R in Eq. 24 was termed the heat removal factor by Duffie *et al.,* (2006). This parameter can be used when selecting a heat transfer fluid. A heat transfer fluid with good heat transfer properties will have a F_R value close to 1 and a poor thermal fluid will score closer to 0.

$$F_R = \frac{\dot{m}c_p}{U_l A_t}\left\{1 - \exp^{-\frac{F'\pi D_o U_l x}{\dot{m}c_p}}\right\} \quad (25)$$

The external thermal losses per meter are determined with the following equation (Eq. 26). T_a refers to the external fluid temperature and for the experimental setup T_∞ is taken as the environmental temperature since the receiver is tilted 25° below horizontal. Using Eq. 26 and Eq. 10 U_{loss} can be updated.

$$\dot{Q}_{loss} = h_w \pi D_o (T_s - T_a) + f_{ij}\sigma\epsilon\pi D_o (T_s^4 - T_\infty^4) \quad (26)$$

It is assumed that the energy gained by the external fluid is equal to the convective loss from the tube surfaces. The radiative losses and reflective/absorption losses are therefore the only "real" losses of the receiver. This equation is updated to account for finned tubes with porosity approximations for the solar penetration and fin conduction efficiency. The methods of implementing the absorption is presented in Appendix H By including the radiative losses in the overall heat loss, which is used to determine the energy gained by the fluid, the re-radiation is incorporated in the energy balance.

A new overall heat loss coefficient can be determined from the combined surface thermal loss function presented above. This set of equations is solved iteratively per control volume until the overall heat loss coefficient of each control volume converges to within an error margin.

4.1.5. Flow

The internal flow analysis is coupled to the heat transfer theory and has been discussed in section 4.1.4. The external flow conditions were estimated at each tube and the air properties re-evaluated after each tube interaction.

The flow was approximated as flow over a cylinder of similar hydraulic diameter to that of the fin tips, with the assumption that most of the flow moves around the finned tubes and not through the fins. This assumption was supported by a low flow rate simulation of staggered finned tubes. As a result, the characteristic length of fully developed flow over a cylinder which is equal to the diameter of the fin tips was used.

It was assumed that the internal flow is fully mixed in the simulation. This assumption implies that all of the fluid in a control volume is at the same temperature. This assumption is sufficient for the 1-D model employed in this study. The effect of boundary layer growth in 3-D is expected to play a major role in the circumferential temperature gradient.

4.1.6. Stress

The experimental manifestation with water as internal fluid instead of pressurised air negates the need for pressure vessel code and stress evaluation in this investigation. Further, the addition of the external fins can be seen as additional reinforcement of the base tube. A detailed stress analysis needs to be carried out should one use high-pressure air at elevated temperatures. Appendix B discusses such an evaluation in brief.

By reducing the thermal stresses due to non-homogeneous wall temperature, early failure of tubular receivers due to fatigue can be reduced (Rodríguez-Sánchez *et al.* 2013). One of the goals of this investigation specifically tackles this problem by increasing the energy harnessing efficiency and reducing the circumferential thermal gradient.

Thermal stresses originate from the restraint of thermal expansion in a structural member. In this case, the non-uniform circumferential temperature may lead to non-uniform expansion of the tubes thus inducing thermal stress. This stress is further concentrated at zones of sharp geometry change such as the roots of the fins.

Thermal fatigue is induced normally at elevated temperatures causing fluctuations in the thermal stress experienced by the material (Callister and Rethwisch 2011). The magnitude of thermal stress at a temperature change ΔT is dependent on the coefficient of thermal expansion α_l and the modulus of elasticity E of the material. Equation 27 can be used for an axially constrained structure.

$$\sigma = \alpha_l \mathrm{E} \Delta T \tag{27}$$

Figure 14 depicts the thermal stress growth relationship of a restricted material to an increase in temperature. Thermal stress can therefore be reduced by allowing the member to expand and contract unhindered or ensuring that the whole member is as close as possible to uniform thermal conditions. An increase of 100 °C of a constrained member equates to a 250 MPa stress.

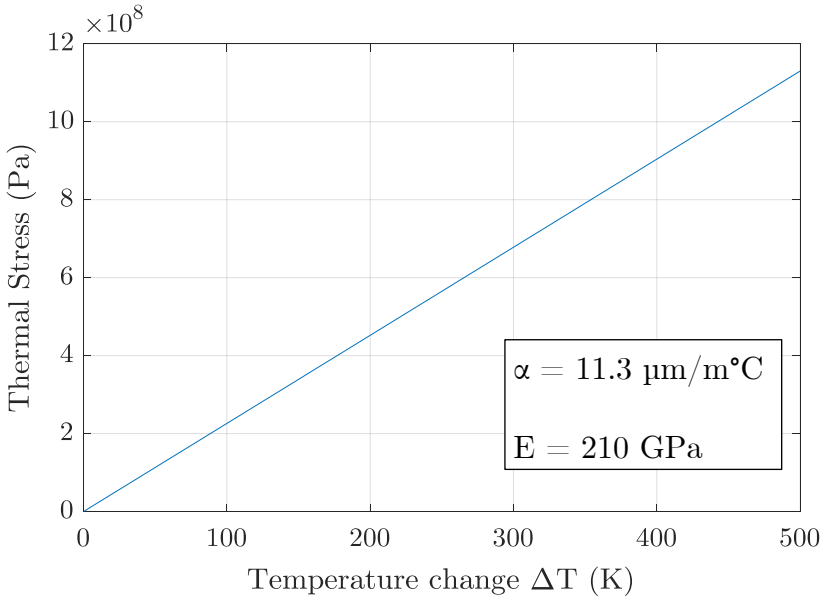

Figure 14: Thermal stress and temperature increase relationship for 1040 Steel with restricted thermal expansion

4.1.7. Creep

Temperature loads over extended periods of time have the tendency to change the material properties and geometry by reducing the ultimate tensile and yield strength. These changes play a role in the onset of creep. Several studies have been carried out to investigate the effects of temperature and loads on creep and material properties. The results of some of these tests can be found in Shigley's Mechanical Engineering Design 10^{th} edition (Budynas and Nissbett 2015) in the form of trend graphs relating temperature and strength properties change.

Further tests were done on long period creep under a constant load and constant temperature. The resulting creep curve display three distinct stages, the first stage exhibit elastic and plastic deformation with a decrease in creep rate towards the end, the second stage exhibit a constant minimum creep rate caused by an annealing effect. During the third stage, the specimen area starts to reduce, further increasing the true stress toward eventual failure.

In the case of a tubular receiver, the differential circumferential temperature load leads to a variation in thermal expansion which increases the cyclic thermal stress in the members.

4.1.8. Thermal shock

Thermal shock is a major concern in CSP receiver operation and measures are taken to avoid thermal shock. These methods include start-up strategies where heliostats are added gradually after a period of receiver inactivity and preheating with the internal fluid. Another method to reduce the risks of failure due to thermal shock is to use materials with good thermal shock resistance values.

The thermal shock resistance of materials can be expressed as the ratio between the fracture strength of the material σ_f, the thermal stress and the conductivity k.

$$TSR = \frac{\sigma_f k}{E \alpha_l} \tag{28}$$

From Eq. 28 it can be deduced that an increase in thermal conductivity will increase the thermal shock resistance. Further, if the Young's modulus is reduced by heat treatment during operation the thermal shock resistance will increase.

4.2. Simulation overview

A number of 1-D models were generated, based on the theory discussed in section 4.1, in order to estimate the receiver behaviour. The following subsections cover an overview of the simulation work performed. The detailed discussion of the models, methods and errors can be found in Appendix H.

4.2.1. Simulation setup

The following assumptions were used for the steady-state 1-D modelling of the receiver

- No axial conduction and axis-symmetric wall temperature.
- The 7 tubes are arranged in a row with slight offset implemented in the view factor and penetration correlation factors.
- Radiative heat transfer between tubes cancel out.
- The cavity walls do not participate in the heat transfer.
- The non-pressurised air temperature is perfectly mixed after each tube row.

- Incident radiation is absorbed on a cylinder approximation based on the geometry of the fins (larger surface area to convection than to radiation).
- Fin efficiency is incorporated to account for conduction to the internal fluid.
- No temperature losses occur in the manifold system.

4.2.2. Modelling methods

For the simulation work three models were created, each with a different implementation of the solar heat flux onto the tube surfaces. One model uses ray-tracing flux projection data as input and the other two models estimate the incident radiation distribution based on field modelling, penetration depth approximations and flux profile assumptions.

The models all use water as internal fluid for the evaluation purposes, once the model accuracy is established the internal fluid can be changed with ease. For all of the models, the view factor to ambient of the tube columns was generated with the S2S radiation model in ANSYS Fluent 18.2.

4.2.3. Modelling similarities

Both Heller (2017) and Kretszchmar (2014) modelled a similar type of receiver geometry. Similar methods to those models were used in this investigation to implement the theory in 1-D. The same trend of surface temperature decrease into the depth of the receiver was predicted as observed in the experimental campaign by Kretszchmar (2014).

In the investigation carried out by Heller (2017) the tubes into the depth of the receiver gradually increased surface temperature up to the material limit. In that study, the layout was optimised for penetration and surface temperature. This strategy predicted that the internal fluid temperature goals can be reached, however, at the expense of the external fluid temperature which falls short of the TES charging requirement.

Both the models employed by Heller (2017) and Kretszchmar (2014) used approximations for staggered tube flow conditions. In this investigation it was assumed that the flow is fully mixed before reaching the next tube, thereby negating the need for staggered tube approximations. The geometry and spacing is not periodic in the radial direction and therefore a staggered approximation will be wrong more often than right.

4.2.4. Computer algorithm

All of the analytical models are based on the same solving algorithm. The algorithm starts by obtaining/estimating the incident radiation on the theoretical model aperture. From there the theory presented in section 4.1 is solved iteratively per control volume throughout the receiver representation until sufficient convergence is reached. The flow diagram is presented in Appendix G.

4.3. Conclusion on theory employed

The most applicable theory to designing, characterising or evaluating the modified HPAR was discussed. Sections 4.1.6-4.1.8 was not critical to the work performed in this study, however, when designing a receiver for commercial operation these factors all play a role in the receiver life. The novel design of the HPAR is expected to reduce the fatigue to some extent.

The accuracy of a 1-D model to approximate the response of a complex 3-D receiver is limited to the validity of the assumptions. The accuracy of the models employed is discussed in Appendix H.

Chapter 5

Experimental work

Based on the findings of the literature review and the numerical investigation of the various components an experimental receiver was constructed, instrumented, installed and operated for several hours. This chapter covers the details of the experimental investigation.

5.1. Experimental design

The experimental setup was designed and instrumented to address all the questions set forth in the study objectives. In order to ensure that data of high accuracy and quality is obtained the measurement methods and locations was of equal importance to the geometry.

The first design decision was the overall size of the receiver cavity. The Helio40 heliostats have a focus area of ± 1 m^2 with a peak in the centre thereof and a Gaussian distribution towards the edges, depending on the aiming strategy and the reflected mirror image. A receiver aperture of 400x400 mm was chosen for a number of reasons. Firstly, the smaller area enables the receiver to harness only the peak of the flux concentration. Secondly, an aperture smaller than the heliostat focus area ensures an even flux distribution on the aperture is obtainable even in the case of drifting of heliostat tracking. Thirdly, a smaller aperture increases the effectiveness of the forced convection, since the flow distribution is easier to control, and thereby the heat removal from the tubes at the aperture which in turn reduces the losses. The penalty for using a smaller aperture is increased spillage from the heliostat field which in essence wastes potential collectable energy. For the purpose of the investigation, the spillage reduction was not as important as ensuring that the whole receiver is irradiated evenly.

The finned tubes are welded to the headers and tack welded to the holes in the locator base plate. Thermal expansion and stresses are of concern in receiver design and operation. At the expected operating temperatures it is not a concern as predicted by the stress analysis.

A steel mesh is fitted to the back of the cavity to mix the bulk fluid before the exit section. A centrifugal blower is located in-line at the back of the cavity which induces the air flow into the cavity. This blower further mixes the flow before sending it along the tailstock where the flow measurement device is located at a significant distance for flow to fully develop.

The internal water flow is operated at temperatures below boiling throughout the cavity. This is achieved by continuous temperature measurement and controlling the incident irradiation with the heliostat control. An in-line low flow rate pump is fitted to the inlet of the receiver to circulate the internal water. To save water a closed loop cooling cycle was constructed using an air-cooled radiator and a 20 ℓ reservoir to complete the circuit before the water is reintroduced to the pump at a lower temperature, the implications of this cooling cycle is discussed in the results section.

5.2. Experimental constraints

There were several major constraints on the experiment namely accessibility, geometry and material.

The experimental setup is situated on an 18 m high square lattice tower which does not have closed walls protecting the walkways from incident irradiation. As a result, the experimental setup cannot be accessed during the tests to do inspection should a sensor malfunction. The location further required the data to be transferred over a greater distance which limited the data acquisition and transfer rate.

The fin geometry was constrained by the standard size of the hollow bar and the manufacturing limitations. These were fairly easy to take into account in the design. The material limitations in terms of stresses and strains were investigated using a FEM model. In the expected operating conditions yielding and rupturing was estimated to be highly unlikely. The process and the results overview is presented in Appendix B.

Temperature loads over extended periods of time have the tendency to change the material properties and in extreme cases the geometry by reducing the ultimate tensile and yield strength. These changes play a role in the onset of creep. The experimental tests were conducted for a short period and at temperatures well below the tempering temperature of the

tube material. Based on the operating conditions, the onset of fatigue was considered highly unlikely.

Temperatures of more than 100 °C in the non-pressurised air are predicted to be achievable which puts a constraint on the extractor fan lifetime. The bearings and the electrical components are exposed to these high temperatures which degrade the components more rapidly than normal conditions. This limitation highlights the importance of fluid mover cooling during operation.

5.3. Experimental setup

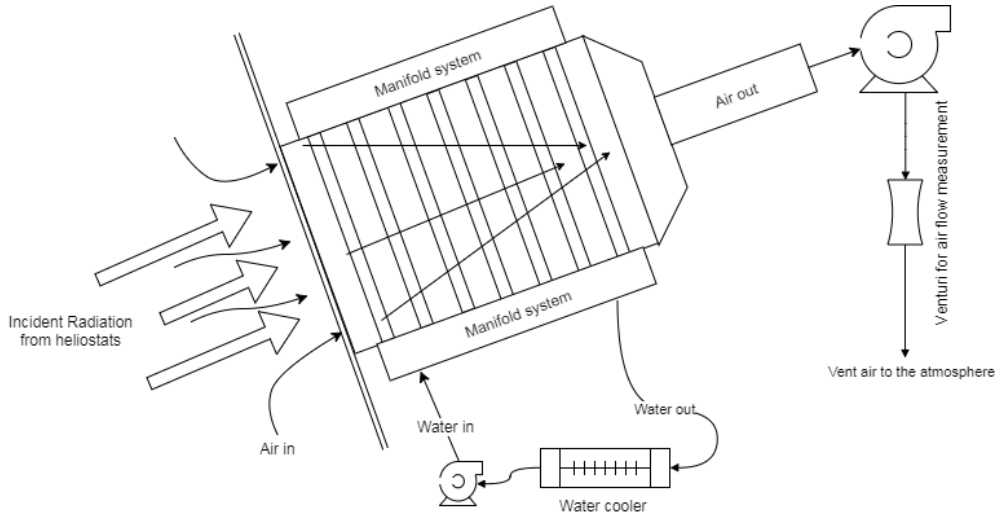

Figure 15: Experimental schematic

The schematic in Figure 15 describes the overall experimental setup, the manifold system connects all the tubes per column in parallel as can be seen in the right-hand side of Figure 16. Ideally, the coolest fluid is pumped to the frontal tubes to reduce the surface temperature and thereby the radiative losses. From there onwards, the flow follows a serpentine path deeper into the cavity increasing the cavity temperature towards the back. This is aimed at supporting the volumetric effect and reducing the radiative losses.

For the experimental testing of the heat-trapping effectiveness of the addition of the external fins the chosen internal fluid was water. Water was chosen to avoid pressurised risks and the ability to simulate an internal fluid with higher heat removal capability than the external fluid. The higher thermal capacity of water results in lower internal fluid

temperature gain and as a result influences the cavity temperature distribution significantly by dampening the thermal variations.

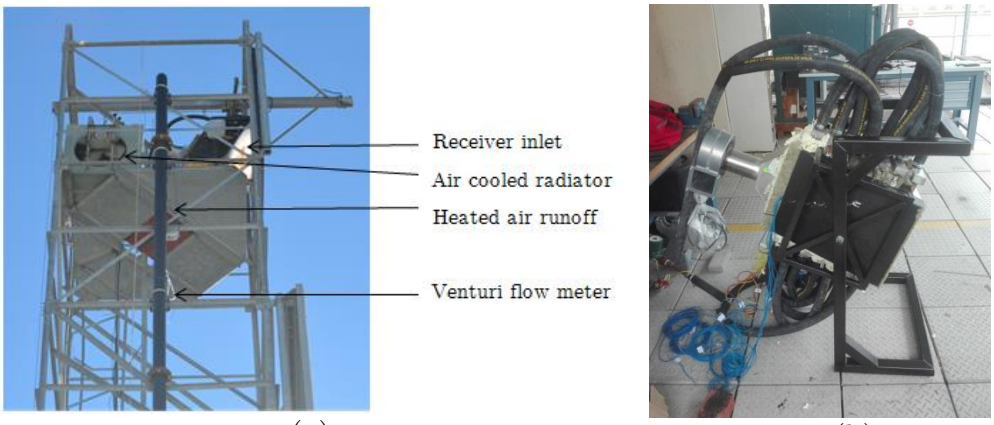

(a) (b)

Figure 16: Experimental setup final layout in operation (a) and the manifold system assembly (b)

It was decided in the installation process to connect the columns of tubes in a spiral fashion, instead of serpentine, flowing from the front to the back towards the middle where it leaves the receiver (Figure 16b). This is aimed at ensuring an evenly distributed internal fluid property and heat transfer. The overall experimental setup is shown in Figure 16a. In future work, the effect of different flow paths of the internal fluid can be investigated numerically with a model validated by the findings of this study.

5.4. Experimental instrumentation

The location and accuracy of the data acquisitioning devices were purposefully selected in order to gather the best data from the test receiver. The experimental instrumentation chosen to capture the data is listed below along with the instrument location, accuracy and importance.

5.4.1. Instruments used

Various instruments were used to gather the different measurements. The most important measurements used to quantify a CSP receiver are temperature, pressure, mass flow rates and incident energy.

When measuring air temperatures in an open volumetric receiver it is important to ensure the thermocouple is shielded from direct irradiation. Special care was taken to locate the air side thermocouple junction tips in the shaded zone behind the tubes.

Care was taken to ensure the surface temperature thermocouples make contact with the surface to be measured. Sheathed thermocouples are used throughout the receiver for its ability to protect the signal wires from environmental damage. Thermal paste was used to enhance the thermal contact with the tube surfaces. This is a good practice in error avoidance to enlarge the contact area of the spherical tip of sheathed thermocouples with the surface. The thermal paste used has a thermal conductivity value of 0.9 W/mK which is $\pm$30 times higher than that of an air gap highlighting the importance of good thermal contact. The film of thermal paste is thin, minimising the thermal resistance and ensuring that the thermocouple does not read false measurements.

For the surface temperature measurements Type K thermocouples are used and for the air and water temperature measurements Type T thermocouples are used.

The mass flow rate of the internal and external fluid is an important measurement to quantify the amount of energy absorbed by the receiver. An energy balance can be performed using these values with which the collection efficiency can be estimated. For the air-flow external to the tubes, a Venturi flow meter is used with pressure taps at the throat and upstream. A silicon piezoresistive differential pressure sensor is used in combination with a Type T thermocouple at the Venturi to determine the density and the mass flow rate of the induced air flow.

The internal water flow is measured with a magnetic core, rotating impeller, external casing hall-effect sensor. The flow rate from the circulation pump is controlled with a valve upstream of the pump to choke the flow to the desired flow rate. The accessibility limitation of the experiment forces the flow rate to be set and kept constant for the duration of the test.

Accurate measurement of the incoming radiation and environmental conditions are critical to the accuracy of the solar to thermal efficiency and radiation penetration results. Minutely data from the Sonbesie weather station located on the roof of the Civil Engineering building next to the testing facility was used to provide accurate environmental values on the day of testing. The incident radiation on the receiver was estimated based on the Helio40 field performance.

5.4.2. Instrument location

Temperature measurements in the cavity are of main concern in this investigation. Specifically the cavity temperature distribution and the finned tube surface temperature distribution.

The front and back tube surface temperature are measured at one location on a tube in each column to assess the development of the temperature and characterise the radiation penetration into the cavity. These selected tubes are marked in Figure 10. This temperature difference is used as a measure of the effectiveness of the addition of the external fins and the operating condition.

Along the side walls, several thermocouples are used to measure the volumetric cavity temperature development. The temperature of the water is measured before and after the receiver in order to quantify the energy absorbed by the internal fluid of the receiver.

A total of 26 thermocouples are used inside the cavity. Fourteen thermocouples measure the surface temperature and twelve measure the cavity temperature. Three thermocouples at different immersion depths in the air runoff are used to measure the average temperature of air leaving the cavity. The outlet temperature thermocouples are located after the centrifugal blower to ensure proper mixing has occurred. One thermocouple is located upstream of the Venturi nozzle to determine the air density for mass flow rate estimations.

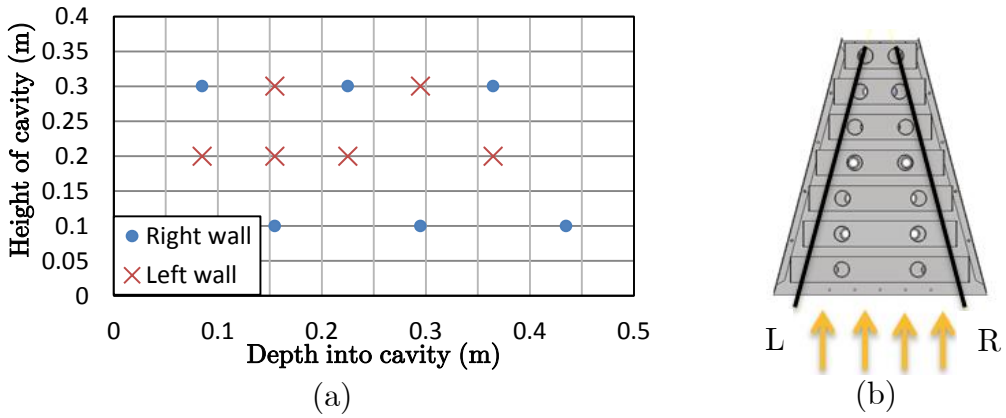

(a) (b)

Figure 17: Thermocouple location in the cavity (a) and top view of the receiver (b)

Figure 17 graphically depicts the location of the Type T thermocouples in the cavity. Left and right wall refer to the cavity walls when viewing the receiver from the heliostat field indicated in Figure 17b. All the

thermocouples on the right wall penetrate 50 mm towards the central axis of the receiver. This ensures that the boundary layer temperature is not measured but rather the bulk fluid temperatures close to the wall. The first two left wall thermocouples at 0.2 m height are situated in the centreline of the receiver and the other four are situated 50 mm away from the left wall.

5.5. Experimental limitations

The experimental setup had several limitations influencing the range of the obtainable data which had to be overcome. The first of which is the heliostat field which consists of 1.83×1.22 m mirrors which are relatively flat. These small heliostats enable a heliostat field to obtain a relatively small focal point without the need for expensive curved concentrating mirrors. The benefit of small heliostats is that a high concentration ratio can be obtained by increasing the number of heliostats instead of the curvature. The test laboratory has a total of 12 operational heliostats which allows for a reasonable quantity of solar heat flux on the experimental receiver aperture with a low peak flux. A heliostat field characterization study based on ray tracing and a visual inspection can be found in Appendix E.

The energy quality of a solar receiver is highly dependent on the incident flux intensity and the modified HPAR even more so. Two approaches can be used to determine the incident energy and therefore the collection efficiency of the receiver.

The first approach is to quantify the incident flux on the receiver aperture which can be done in several ways of which three is discussed. The first method is to measure the flux distribution on the receiver aperture with a scanning calorimeter which the facility does not have. The second method assumes a Gaussian distribution of flux profile, using a thermal imaging camera the peak is determined and the variance on a cross-section is measured. This peak and variance is input into the Guassian function. From there the distribution can be generated and the average incident flux determined. The third method which is widely used is flux mapping with a SSD camera and a calorimeter. The calorimeter is typically positioned in the centre of a white Lambertian target onto which the heliostats are focussed. A picture is taken and the light intensity per pixel of the image is scaled relative to the point of the calorimeter, the scaled distribution is then updated with the intensity measured by the calorimeter.

The second method of determining the collection efficiency lumps the whole system efficiency together by comparing energy incident on the heliostat field to the harnessed energy. This efficiency is lower than the thermodynamic efficiency but is sufficient for the purpose of this investigation since it takes all the losses of the field into account without having to determine them individually.

At the time of the investigation, there was no equipment to measure the incident flux profile and intensity on the receiver test facility. To develop such a system was considered outside the scope of this study and therefore the overall solar to thermal efficiency was used instead. This is characterised as the ratio of harnessed energy to the incident solar irradiance that falls onto the heliostat field aperture. The objectives are not to measure the collection efficiency but instead the quantities absorbed in the two fluids. This method will result in lower field efficiencies since the aperture of the receiver is smaller than the focal image of the heliostats and therefore the spillage portion is increased further.

5.6. Error analysis

In order to provide reliable results, all sensors were calibrated and the calibration error noted. With the error margin of all measurements taken into account, the accuracy of the various measurements can be assessed. The main measurements are temperature, flow rate and pressures. The incident flux on the aperture was estimated from ray-tracing. The individual sensor error analysis can be found in Appendix D along with the selected calibration curves. The overall system measurement error was estimated to be 4.96 %.

5.7. Conclusion

The experimental setup discussed in this section was designed and instrumented to meet the objectives set for this study. The heat removal relationship of the two fluids relative to the maximum available power on the heliostat field was chosen as measure of receiver operation instead of collection efficiency. Future studies can use the data to validate assumptions and expand the knowledge of the HPAR by parametric analysis.

Chapter 6

Experimental results

Several tests were conducted in order to ensure repeatability and generate reliable data with which future studies can be validated. These tests ran for several hours at a time to capture ramp-up, steady-state and ramp down responses. A total of 34:45 hours of testing was carried out over a period of a month.

In this chapter, the most significant observations are highlighted and discussed. The objectives of acquiring data with which to validate the modelling performed by Heller, (2017) and address the assumptions and conclusions are discussed in this section.

6.1. Results

The receiver test facility has limited obtainable flux intensity which relates to lower temperature operating conditions in comparison to the intended use of the full-scale receiver. As a result, the data in this test is suited to validate future theoretical models. Based on the data with surface temperatures of below 100 °C it is, however, hard to draw accurate conclusions on the expected behaviour at surface temperatures in excess of 900 °C. Thermal radiation is a function of the fourth power of the temperature difference between the surface and the environment, which relates to a radiative loss magnitude difference of ±97 times between experimental and Brayton integration required temperatures.

In order to characterise the response of the receiver during operation the operating conditions were varied and the responses logged. The receiver is exposed to seven variables during on sun testing of which two were controlled. These uncontrolled variables are changes in inlet conditions of both the fluid streams and the controlled variables are the respective fluid flow rates.

The following tests were conducted in the experimental period:

- Half and full heliostat field to compare the effect of flux intensity
- Windless and windy days to assess the convective loss trapping abilities
- No induced flow into the cavity (single fluid receiver operation)
- No internal fluid (pure volumetric receiver) to investigate the external convection and conduction heat transfer with no internal heat removal
- Variation in both the internal and external fluid simultaneously and independently

6.1.1. Circumferential temperature difference

The ability to control the circumferential temperature difference is a major advantage of the modified HPAR over other tubular air receivers. The addition of the external fins is expected to contribute to the reduction in the thermal stresses potentially extending the fatigue life of the receiver. During the tests by Kretzschmar, (2014) the surface temperature difference for unfinned tubes was not measured and as a result, there are no comparable data to measure the heat transfer improvement of the fin additions.

The circumferential temperature similarity is defined as the shadow side surface temperature divided by the irradiated side surface temperature. There exists no literature on the circumferential heat transfer of tubular heat exchangers by induced flow in CSP applications, so instead comparative values to judge the enhancement from the PML tubes of SOLHYCO and published circumferential temperature similarity for molten salt CSP receivers was used. During tests the PML tubes could obtain a claimed 80.9% circumferential similarity for an internal air receiver (DLR 2010), no value was included for the eventual tubes used in the receiver which was not PML. In the article by Rodríguez-Sánchez *et al.* (2013) the similarity for a traditional tubular salt receiver is in the range of 65%.

$$\Delta T_{circ} = \frac{T_{back}}{T_{front}} \tag{29}$$

The thermal response for a single test is illustrated in Figure 18. A sensitivity analysis of the influence of the different variables is conducted

in section 6.2.2. The first portion is when the heliostat field has not been added, the sharp decrease in circumferential temperature similarity is the effect of the heliostat field focal point moved onto the receiver. The temperature differential is a function of several factors of which the location is the largest. The location of the tube determines the amount of energy incident onto the irradiated surface which increases the difference. Further, the tube location determines the induced flow conditions which reduce the difference. The first tube experiences the largest circumferential radiation intensity difference and the least amount of forced heat transfer from the induced flow. Furthermore, the first tube is exposed to the largest radiative and convective losses. During this test, the largest gradients and variations are experienced by the first tube. The circumferential similarity demonstrated the ability to improve from 60 % to 70 % based on the variation of induced flow conditions.

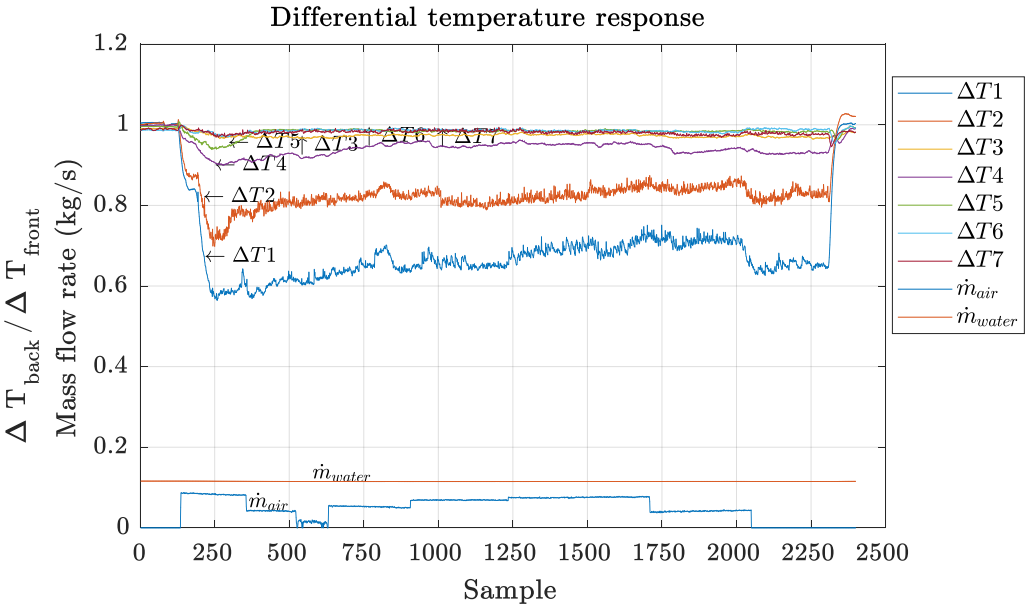

Figure 18: Circumferential temperature response 18 July 2018

The second tube column experiences slightly less direct irradiance combined with an increased velocity of the induced flow, both of which contribute to the reduced circumferential temperature gradient of 78 %-85 %. The effect and effectiveness of the fin addition and induced flow is best illustrated at this location. Tube column 3&4 are situated behind column 2, the direct irradiation is therefore shadowed making these tube columns reliant on reflected radiation scattered by the upstream tubes, radiative heat transfer between tubes and the external convective heat transfer. The effects of these modes of heat transfer are assumed to be

fairly uniform on the circumference. The similarity of 95-98 % on tube column 4 is attributed to the reflected radiation penetration and the external fluid conditions.

Tube column 5 is geometrically situated at an offset from columns 2-4 and therefore is exposed to some direct irradiance. At this stage, the induced flow is well mixed and the wedge shape of the cavity has increased the flow velocity to almost twice the inlet velocity, enabling more effective heat transfer. Throughout the duration of the test, the circumferential similarity was kept at 98 %.

The surface temperatures of the last two columns are only dependent on the internal and external fluid and as a result, the ratio is at almost 100 % throughout.

In the sensitivity analysis, the effects of the variables on the variation in these values are discussed. From this data, it can be concluded that the receiver is able to demonstrate the ability to control the circumferential temperature similarity by variation in the external fluid. This severs a dual purpose: firstly, it removes heat from the irradiated side of tubes which has the highest view factor to the environment and therefore experiences the most radiative losses and secondly, it reduces the non-uniform expansion which can potentially extend the tube fatigue life.

6.1.2. Cavity temperature distribution

Using the twelve thermocouples located in the cavity an interpolated 3-D thermal volume was rendered in order to provide insight into the overall cavity thermal conditions. This 3-D interpolated distribution can be sliced at locations of interest to yield a 2-D contour of the thermal distribution at that location.

The complex nature of the receiver geometry made it hard to accurately capture the overall thermal conditions since the flow conditions and paths of the induced flow are expected to determine the local hot and cool spots. It was originally assumed that the receiver will exhibit symmetrical thermal conditions and as a result, some thermocouples were situated on the one wall and the others at different locations on the other wall to increase the spatial resolution of the volumetric thermal conditions data.

The location-specific flow and thermal conditions proved to be problematic since the heliostat field is not symmetrical relative to the aperture and as a

result, the right wall received more radiation, increasing the temperature of the flow along the wall. Furthermore, the spillage by the heliostat field heated the plate surrounding the aperture effectively preheating the inlet temperatures at the aperture circumference while a cooler core flow is expected to be drawn into the centre of the aperture. Appendix E discusses the heliostat field limitations experienced. It is noteworthy that the surfaces at the receiver aperture demonstrated no observable hotspots when imaged with an infrared camera. This suggests that the flow does mix well enough to overcome the non-uniform inlet conditions.

The interpolated thermal distribution at the right wall of the cavity, in Figure 19, illustrates this high temperature preheated condition from the spillage as discussed earlier. From the vertical contours, it is interpreted that the flow mixes well and that the effect of heat rising to the top of the receiver is suppressed by the induced flow.

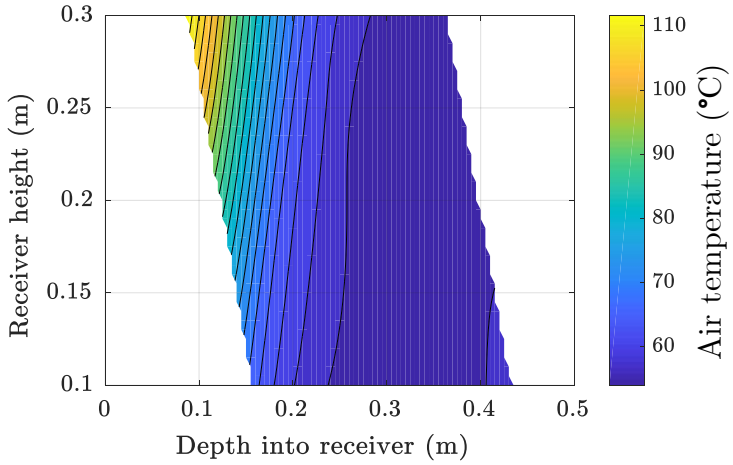

Figure 19: Interpolated cavity temperature distribution at the right wall

The contours on the left wall (Figure 20) exhibit higher core temperatures and cooler wall temperatures. From this contour, the absence of heat rising to the top of the cavity, observed in Figure 19, is confirmed. The warmer core flow conditions observed demonstrates the challenge of non-uniform thermal conditions experienced by volumetric receivers. The incident irradiation on the tube surfaces of CSP receivers generally forms a Gaussian distribution with a peak at the centre if aimed properly. This flux concentration on the receiver aperture centre leads to peak surface temperatures measured at the centre of the tube height, resulting in warmer core temperatures in the volumetric receiver. A similar condition is

expected to be experienced at the right wall. This could not be confirmed due to the lack of thermocouples on the centreline of the right wall.

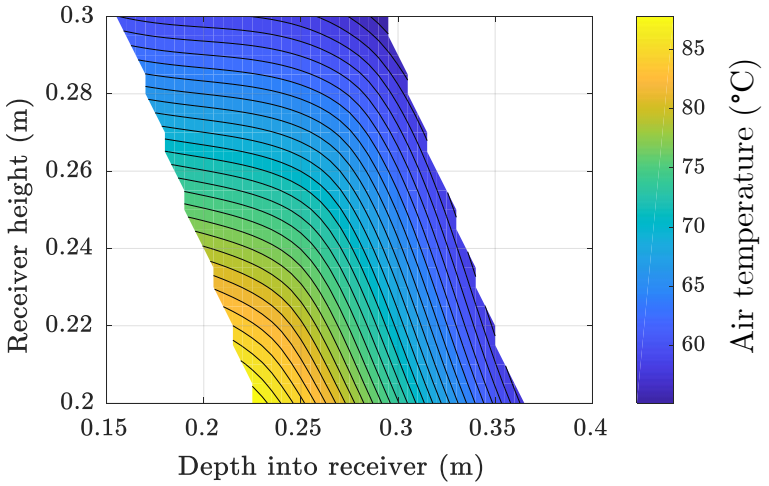

Figure 20: Interpolated cavity temperature distribution at the left wall

The transient response of the cavity temperature distribution was captured for all the tests with which future simulations can be validated. Some of these tests can be found in Appendix F.

6.1.3. Heat removal relationship

In order to quantify the effect and effectiveness of the fin addition to the tubes a heat removal study was conducted. The relationship of heat removal by the two fluid streams is compared for all the tests. The heat removal term includes mass flow rate, specific heat at the immediate fluid conditions and the relationship between outlet and inlet conditions for each sample. The heat removal for different tests was normalised to enable direct comparisons between tests. The normalising methods and constants are discussed in the sensitivity analysis in section 6.2.

The system efficiency exhibits a linear relationship between the two heat removal quantities, which enables linear interpolation between the points. In Figure 21 the resulting data plot is produced. The linear relationship is demonstrated by the straight line contours. The plot in Figure 21 demonstrates the ability of the receiver to shift the heat removal quantity from the one fluid to the other at constant system efficiency, thus confirming the intended ability to bypass the Brayton cycle bottle-neck as intended by Heller.

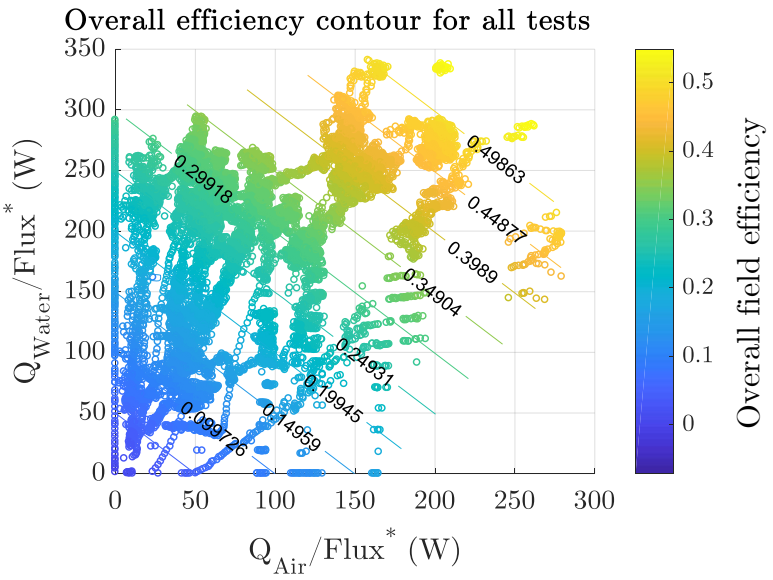

Figure 21: Scattered data plot for all the tests with system efficiency contour lines

The y-axis represents the internal fluid and the x-axis the external. During periods when a cycle bottleneck is experienced a control system, which keeps the energy absorbed by the internal fluid constant, will enable the receiver to move horizontally on the contour plot in Figure 22. This is expected to increase the receiver efficiency while harvesting the excess energy. The TES inlet requirement is, however, temperature oriented and not energy quantity. This may require the receiver to be operated at less efficient conditions to achieve higher outlet temperatures of the non-pressurised side.

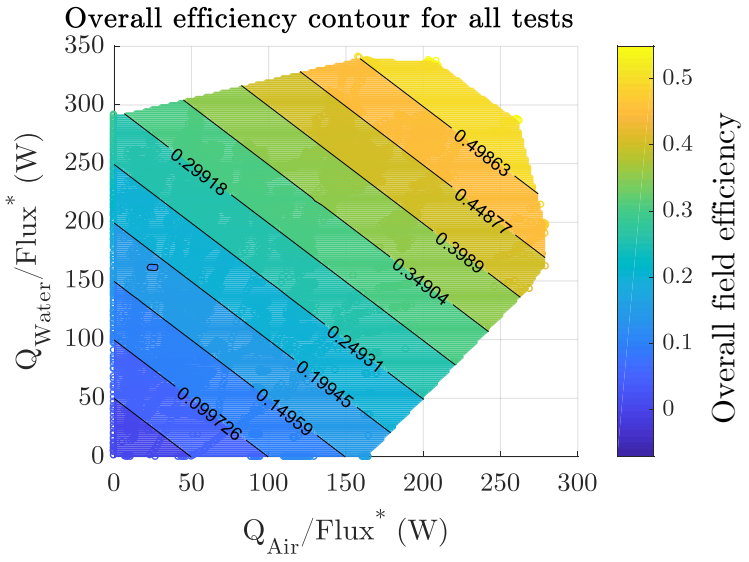

Figure 22: Efficiency contour for all tests of the modified HPAR

From the gradient of the contour lines it can be interpreted that the relationship between external and internal heat removal for the test receiver is inversely proportional for constant efficiency operation. Furthermore, the challenge of inversely proportional heat removal by the two fluid streams faced by the modified HPAR is highlighted.

In order to obtain higher outlet temperatures at a constant mass flow rate in one fluid a reduction in mass flow rate in the other fluid stream is required. Priority will be assigned to the internal fluid during operation of the SUNDISC cycle which will require the secondary fluid stream to be operated at low mass flow rates in order to meet the TES charging requirements. These low mass flow rates are expected to reduce the receiver efficiency significantly by rendering the effects of the secondary fluid flow insignificant.

6.1.4. Surface temperature distribution

The radiation penetration is geometry dependent. In order to assess the extent of the radiation penetration a surface temperature distribution investigation was used. The same behaviour, as discussed in section 6.1.1., can be observed in Figure 23. The tubes with a large difference between the front and back side experience more incident irradiation than the tubes with almost uniform front and back side temperatures. Using the inlet, outlet and the two thermocouple temperature readings between tube column 1&2 and 2&3 a spline was fitted to connect the centreline air temperature development.

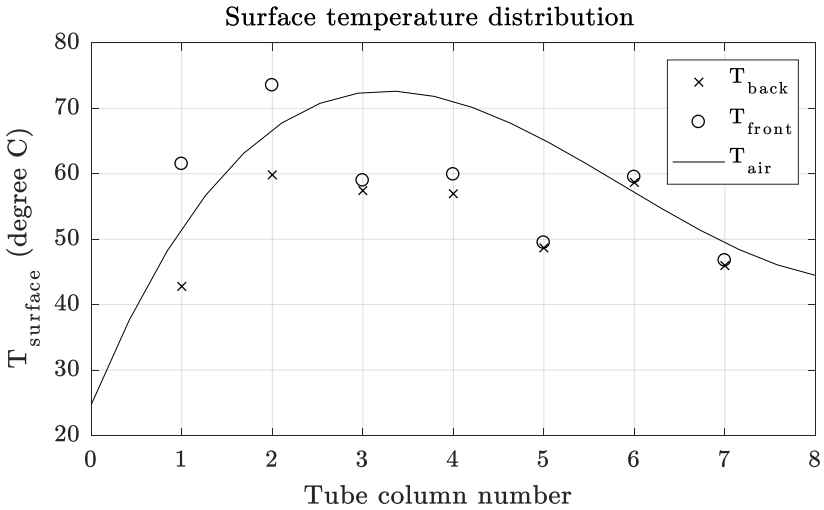

Figure 23: Measured temperature distribution at steady-state on 18 July

The water was cycled in a 1-7-2-6-3-5-4 path which proved to result in a good average fluid temperature development. This highlighted the effect of radiation penetration in terms of differential front and back temperatures. This flow path did not support the volumetric effect by flowing in a serpentine path into the depth of the receiver and thereby moving the warmest fluid to the back.

The external fluid leaves the cavity at a lower temperature than the surface temperatures at the aperture, thus not achieving the volumetric effect. The second column is at a higher temperature than the first column which is indicative of ray penetration, ray trapping capability and improved flow conditions. The second tube row has a smaller view factor to the environment and reradiates to the shadow side of the first tube row. The inability to achieve the volumetric effect is partly due to the non-optimised tube layout and partly the internal flow strategy. Literature of receivers demonstrating the volumetric effect during design point operation could not be found.

6.1.5. Pure tubular volumetric comparison

As discussed in the previous section the receiver could not demonstrate the volumetric effect, as defined by Ávila-Marín (2011), during dual fluid tests. In order to assess the volumetric effectiveness of the staggered tubular cavity with the micro-cavities formed by the fins, the receiver was operated with no internal fluid. The only comparable data to this was the tests by Kretzschmar, (2014). Kretszchmar constructed and tested a much smaller unfinned staggered tubular receiver (the original HPAR).

The experiment of the modified HPAR and the original HPAR could not be compared directly due to several differences. In the original HPAR, the tubes were staggered with constant offset throughout, the heliostat field was symmetrical with respect to the aperture and limited data is available of the thermal distribution in the receiver cavity. The data is limited by the number of thermocouples used as well as the relatively short operating times. The induced air mover was only permitted to operate with fluid temperatures below 40 °C and as a result, the tests were terminated before steady-state operation was reached.

The porosity of the volumetric side of the dual receiver was selected to compare the two test receivers. For this comparison, the porosity of a tubular volumetric receiver is defined as the combined open area for every slice of the cavity per column. The porosity as defined in equations 30

and31 assigns a value of tube density viewed from the front to the back of the receiver.

$$\eta_{\mathrm{open_i}} = \frac{\mathrm{A_{open}\ (m)}}{\mathrm{A_{totalslice}\ (m)}} \tag{30}$$

$$\eta_{open_{receiver}} = \eta_{\mathrm{open_i}} * \eta_{\mathrm{open_{i+1}}} * \cdots * \eta_{\mathrm{open_{n-1}}} * \eta_{\mathrm{open_n}} \text{ for (i: 1: n)} \tag{31}$$

A larger open porosity ensures deeper radiation penetration and the convective surface area to aperture area ratio is indicative of the trapping and convective heat transfer ability of the receiver. The original HPAR was more densely packed which ensured good mixing of the external fluid at the cost of penetration depth. The modified HPAR tested in this study had significantly larger open porosity than the original HPAR enabling deeper ray penetration. The addition of the external fins increases the surface area ratio of the modified HPAR by 5.64 compared to a hypothetical unfinned equivalent while halving the open porosity. This is expected to increase the harnessing effectiveness of the receiver significantly. Table 4 compares the volumetric characteristics of the original HPAR, a theoretical modified HPAR with the same dimensions as the modified HPAR in this study with the exception of not having fins and the experimental modified HPAR from this study.

Table 4: Volumetric comparison of HPAR concepts

Receiver	Open porosity to the back	Surface area/aperture area
HPAR	0.11 %	11.30
Modified HPAR with fins	2.155 %	28.35
Modified HPAR without fins	4.238%	5.03

During on-sun testing steady-state operation at aperture tube surface temperatures of 480 °C was achieved for the modified HPAR, while maintaining a steady outlet air temperature of 118 °C at 0.056 kg/s. As a single fluid receiver, the modified HPAR could not demonstrate the volumetric effect either. This inability to achieve outlet temperatures at higher temperatures than the surface temperatures at the aperture is largely the result of insufficient radiation penetration.

The air temperature development in the cavity does demonstrate the ability to remove heat from the tubes at the aperture and transfer this gained heat to tubes deeper in the cavity. For this convective heat transfer to be effective, the spacing between the tubes needs to be close enough to

mix the fluid flow adequately, this contrasts radiation penetration which prefers open porosity. Kretzschmar, (2014) suggested and demonstrated in tests that the radiation losses can be reduced and penetration be increased by replacing aperture tubes with quartz prisms.

Having operated the receiver as a pure open volumetric receiver the effect and effectiveness of the staggered finned tube cavity is demonstrated in Figure 24. The incident power per mass flow rate is determined by dividing the estimated incident power on the aperture by the mass flow rate of the induced air into the receiver. During the tests, the receiver posted collection efficiencies of up to 78 % as a volumetric receiver. These efficiency values confirm the effectiveness and ability of the finned tubes to trap incident radiation and losses.

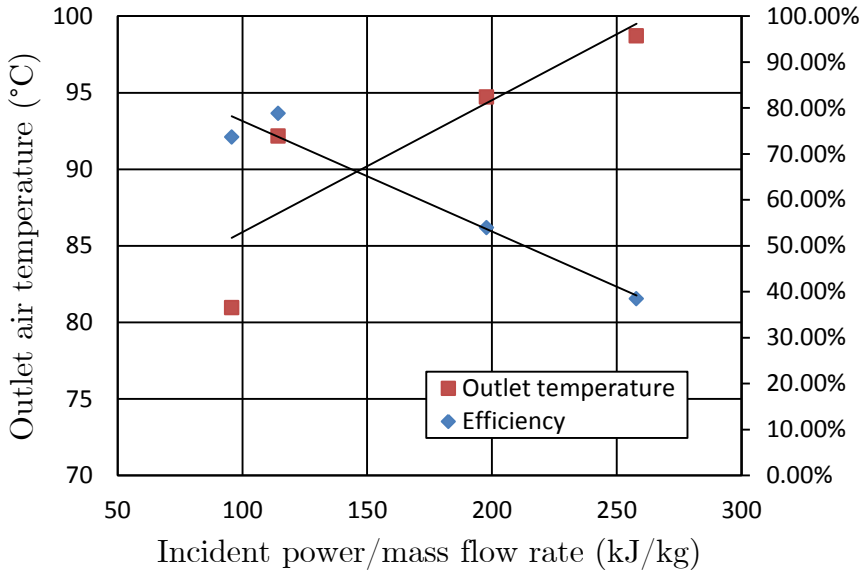

Figure 24: Volumetric receiver performance of the modified HPAR

6.2. Sensitivity analysis

During tests, the receiver was exposed to a number of controlled and uncontrollable variables which yielded so-called 'real-world/on-sun' transient operation data. In order to determine the effect of the variables on the receiver operation and to compare the impact of each variable relative to the others, the variables had to be non-dimensionalised. Normalising the data of all the tests enabled comparison of the heat removal effectiveness over a range of operating conditions. The

standardisation constants selected for the experimental data is presented in Table 5.

Table 5: Standardisation constants

Variable	Standardisation constants
Temperature	298 K
Pressure	101 325 Pa (1 atm)
Mass flow rate	1 kg/s
Irradiance	1000 W/m^2
Area	1 m^2
Wind velocity	1 m/s

The non-dimensionalised form of the variables is presented in equations 32-36. The irradiance normalisation ($Flux^*$) normalises both the radiation intensity as well as the heliostat field aperture for the tests. This method proves to be good for small flat heliostats where the intensity is directly proportional to the number of heliostats. Using this approximation the data can be extrapolated to approximate larger field sizes.

$$T^* = \frac{T}{298\text{K}} \tag{32}$$

$$P^* = \frac{P}{101325\text{Pa}} \tag{33}$$

$$V^*_{wind} = \frac{V_{\text{wind}}}{1\left(\frac{\text{m}}{\text{s}}\right)} \tag{34}$$

$$Flux^* = \frac{DNI}{1000\left(\frac{\text{W}}{\text{m}^2}\right)} \times \frac{\text{A}_{\text{heliostatfield}}}{1\text{m}^2} \tag{35}$$

$$\dot{m}^* = \frac{\dot{m}}{1\left(\frac{\text{kg}}{\text{s}}\right)} \tag{36}$$

The heliostat field efficiency in terms of blocking and shading, spillage, and cosine losses is encompassed in the overall system efficiency, which is combined with the receiver collection efficiency. The steady-state data was compared for all the tests to determine the sensitivities to the various variables. Both a multiple linear and multiple non-linear regression analysis was used to approximate and compare the sensitivity to the variables. The form of the non-linear equation (Eq. 37) was chosen for the ability to be transformed to the linear domain using a natural logarithm.

Multiple non-linear:

$$\eta_{\text{system}} = C \times e^{\left(\text{a}_0 P^* + \text{a}_1 \dot{m}^*_{\text{air}} + a_2 \dot{m}^*_{\text{water}} + \text{a}_3 T^*_{\text{airin}} + \text{a}_4 T^*_{\text{waterin}} + \text{a}_5 Flux^* + \text{a}_6 V^*_{\text{wind}}\right)} \tag{37}$$

Multiple linear:

$$\eta_{\text{system}} = a_0 P^*_{\text{atm}} + a_1 \dot{m}^*_{\text{air}} + a_2 \dot{m}^*_{\text{water}} + a_3 T^*_{\text{airin}} + a_4 T^*_{\text{waterin}} + a_5 Flux^* + a_6 V^*_{\text{wind}} + C \quad (38)$$

6.2.1. Overall system efficiency sensitivity

The coefficients in Table 6 were determined by fitting the steady-state response of overall system efficiency to the variation in the variables. The coefficient of determination (R^2) for 4459 observations of steady-state data was higher for the linear regression than that of the non-linear regression and as a result from here onwards it will be accepted as the sensitivity analysis tool of choice as it could better account for variance.

Table 6: Coefficients of the regression functions

	Linear	Non-linear
a_0	0.701	2.044
a_1	1.558	4.916
a_2	0.781	6.472
a_3	-2.284	-0.615
a_4	2.925	-5.077
a_5	-0.012	-0.005
a_6	3.75e-4	-0.002
C	-1.144	6.832
R^2	0.971	0.831

The atmospheric pressure has a positive effect on the system efficiency. An increase in atmospheric pressure relates to a density increase of the air which relates to an increase in heat removal capability of the external fluid. Increasing the mass flow rates and thereby the heat removal also has a positive influence on the system efficiency in both linear and non-linear regression analysis's, the efficiency is directly related to the heat removal by the streams. The variation in mass flow rate of the external fluid has a larger influence than that of the internal water according to the analysis.

A decrease in ambient temperature and thereby the inlet conditions in both cases points towards higher system efficiencies since the thermal gradient between the surfaces and the heat removal fluid is larger. Increasing the receiver flux intensity slightly decreases the overall efficiency since losses tend to increase with larger field sizes. The effect of wind was found to be negligible in comparison to the other variables during the tests, confirming the ability of an HPAR to capture the convective losses at the test conditions.

In the data sample analysed an increase in inlet water temperature relates to a strong increase in overall efficiency rating. This is suspected to be the effect of an increase in surface temperatures which can support larger quantities of heat transfer to the external fluid. During tests, the convective heat transfer was significantly larger than the radiative losses which support this observation. Notably, the two regression analyses show disagreement on the effect of the inlet water conditions. At intended operating conditions for the SUNDISC cycle the effect of radiative losses will be significantly more severe and as a result, lower inlet fluid conditions is expected to increase the receiver efficiency.

6.2.2. Circumferential temperature difference sensitivity

Having established in the previous section that the multiple linear regression analysis best predicts the system sensitivities with regards to variations in the seven variables the effect of the variables on the circumferential thermal gradient could be established. A test was selected in which both the internal and external fluid mass flow rates were varied to better capture the effects.

The tests included start-up, transient, steady-state operating and cool down periods. The data presented in Table 7 is based on a total of 2777 observations made. As before the variables were non-dimensionalised enabling the analysis results to be directly compared between the tests. The magnitude and sign of the coefficient once again determine the effect of the variable relative to the rest.

Table 7: Circumferential differential temperature sensitivity

	dT1	dT2	dT3	dT4	dT5	dT6	dT7
Intercept (C)	-40.046	-5.379	9.509	9.928	8.053	12.919	25.234
$Flux^*$ (a_5)	-0.114	-0.030	0.005	-0.002	0.005	0.015	0.028
V^*_{wind} (a_6)	-0.009	0.001	0.001	-0.001	-0.003	-0.001	0.002
P^* (a_0)	44.848	7.916	-7.331	-7.800	-5.482	-9.710	-22.975
T_{airin} (a_3)	3.078	2.421	-1.091	-0.102	0.838	1.423	-0.098
$\dot{m}^*_{air}$ (a_1)	1.226	0.366	0.276	1.004	0.488	0.561	0.200
$\dot{m}^*_{water}$ (a_2)	-0.704	-0.236	-0.044	0.060	-0.454	-0.054	-0.360
T_{water} (a_4)	-4.098	-3.163	-0.306	-1.073	-2.555	-3.846	-1.932
R Square	0.488	0.407	0.725	0.706	0.807	0.657	0.663
Standard deviation	0.046	0.018	0.005	0.013	0.007	0.016	0.012

The coefficient of determination of the variables to the circumferential temperature difference is below 0.5 for the first two tubes, deeper into the cavity more acceptable values are found. The low R^2 values for the first

two tubes can be attributed to a lack of information with regards to the radiative properties of the fins in terms of reflection, re-radiation, conductance and absorptance. The first two rows exhibited more variation, as demonstrated in Figure 18, since these tubes were exposed to larger variations in inlet conditions.

For all the circumferential temperature difference cases the variation in circumferential temperature difference is influenced positively by the induced air flow rate and negatively by the internal fluid mass flow rate. The variation in the internal flow was limited and the negative influence may only be specific to this analysis and an result of the regression analysis used. The induced air flow thus demonstrates the ability to move heat to the shadow side of the tubes by means of forced convection between the fins.

The absence of passive inserts to the inside of the tubes leads to unmixed internal fluids at the experimental conditions. This unmixed fluid flow is suspected to form a non-circumferentially uniform thermal boundary layer. This boundary layer formation is suspected to contribute to the circumferential temperature difference.

The coefficient of the atmospheric pressure is the largest in every test since a change in pressure relates to an increase in density and thereby better heat removal by the external fluid. The atmospheric pressure is not expected to change significantly during operation and can technically be omitted from the regression analysis.

The effects of the different variables are location specific and the sensitivity of each observed tube should be accessed individually.

6.2.3. Fin height sensitivity

To assess the effect of the fins a parametric study was undertaken using the experimentally corrected 1-D model. This model, based on the theory in Chapter 4, and the errors thereof can be found in Appendix H. In this sensitivity investigation the fin height and mass flow rate was varied and the results thereof compared in Figure 25.

The fin height was varied from 0 m (no fin) to 0.01 m (maximum fin height possible before the tubes make contact in the experimental setup). The mass flow rate of the external fluid was varied between 0 and 0.105 kg/s (the operating range of the experimental receiver). The outlet

air temperature contours are presented in Kelvin. In order to achieve higher external fluid outlet temperatures the fin height needs to be increased and the flow rate decreased. Fin height increase relates to more heat transfer area and lowered flow rate to increased temperatures at the same total energy removed.

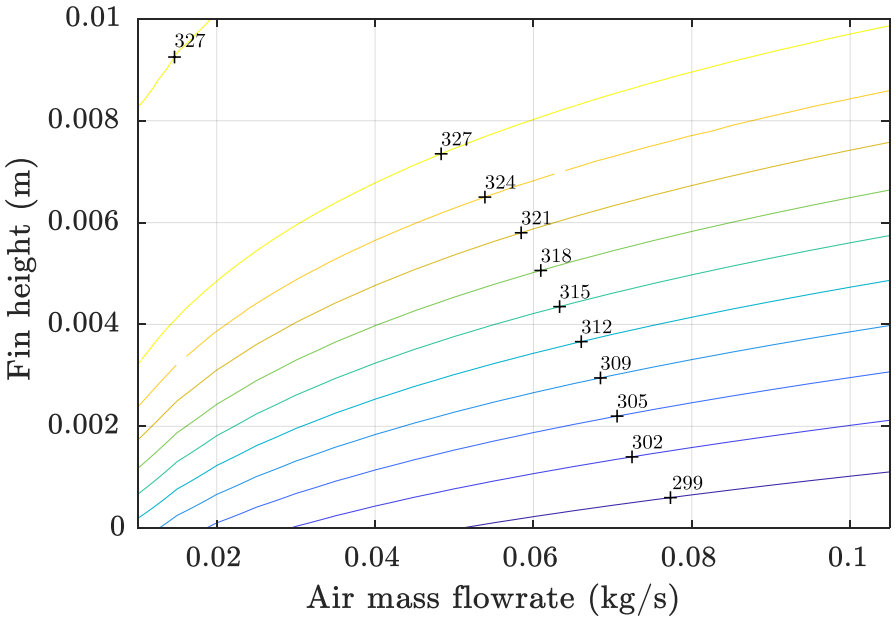

Figure 25: Contour of fin height and mass flow rate relationship to outlet air temperature

6.3. Experimental observations

This section discusses observations made during the period of experimental testing. The observations were divided into two distinct divisions, namely operating observations and physical observations.

6.3.1. Operating observations

During the experimental campaign a total of 34:45 hours of testing was conducted during which 37 data points were collected every 4 seconds. These included start-up, transient, steady-state, interruptions and shut down of the receiver operation. The surface and external fluid temperature response to heliostat de-focussing and refocusing was relatively fast. The thermal inertia of the internal fluid in the closed cooling loop, however, increases the time until steady state operation is reached.

The following graphs illustrate the system response on the 18th of July 2018, other significant test observations are presented in Appendix F. The

gradual changes in the temperature values of the surfaces can be attributed to the change in the external fluid flow rate. The sudden decreases at times with constant induced air flow are attributed to heliostat tracking errors such as focal point drift.

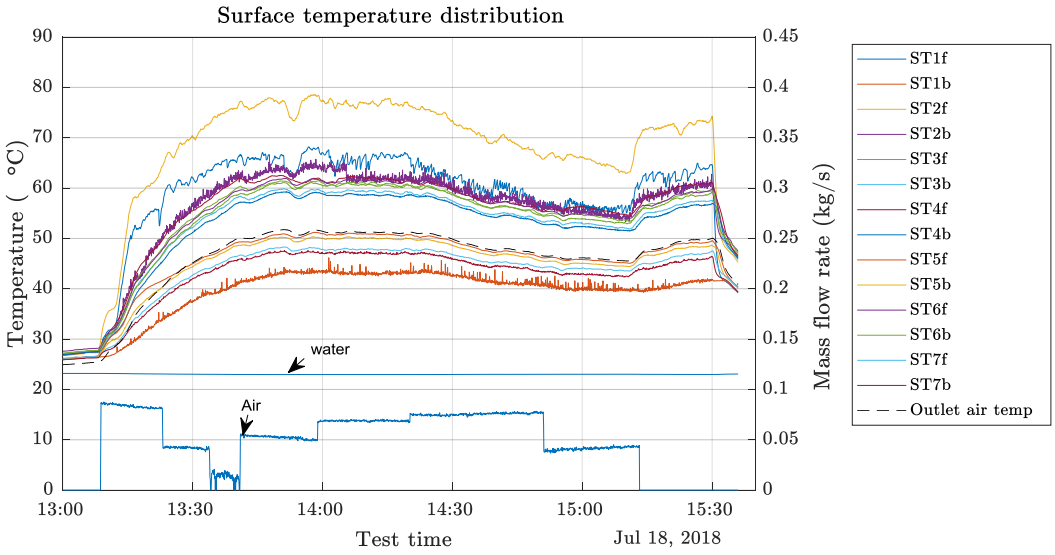

Figure 26: Surface temperature distribution data for 18 July

The surface temperature distribution in all the tests experiences a smoother trend than the cavity air temperatures. This is the result of the higher thermal inertia of the metal surfaces and the internal fluid in comparison to the non-pressurised external air.

Furthermore, in all the tests it can be observed that the cavity temperatures reach equilibrium in a shorter time than the surface temperatures. This is an artefact of the experimental setup which incorporates a closed loop, air cooled, water cycle which has to reach a thermal equilibrium with the environment. This can potentially be improved by decreasing the volume of the cooling cycle or increasing the cooling ability of the radiator. The best case scenario would be to have the system connected to a large source.

The sharp peaks in the air mass flow rate values are the result of the pressure transducer zero shift error correction and measurement error at low flow rates. The blower used to move the air into the cavity has a limited pressure rise capability. This required the Venturi design to minimise the pressure loss. The pressure measurement error can be

reduced by increasing the flow rate or decreasing the throat diameter thereby measuring a larger pressure differential.

The receiver demonstrated robustness to the minor variations in induced flow rate. This behaviour is expected to be amplified at Brayton cycle preheating material temperatures due to the linear increase relationship of convective heat transfer and differential temperature between the surface and induced air.

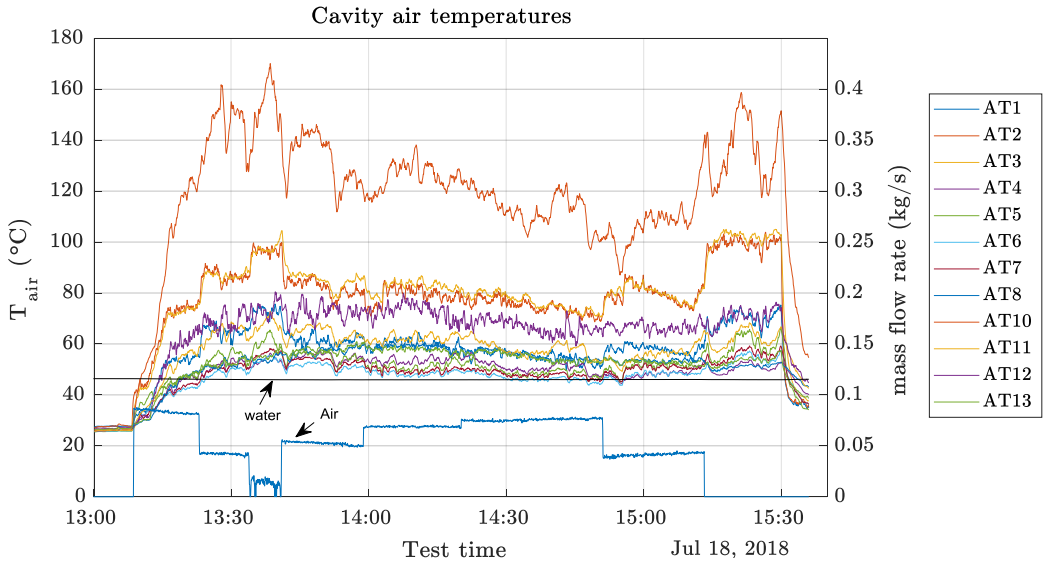

Figure 27: Cavity air temperature development data for 18 July

For the non-pressurised air to reach the desired outlet conditions for combined cycle integration, the surfaces at the back of the receiver need to be at a higher temperature. This illustrates the need for increased radiation penetration and operating strategies supporting the volumetric effect.

The large temperature measurement experienced by AT2 is attributed to a stagnant hotspot on the shield plate in the vicinity of the receiver aperture. The heliostat field focal point is larger than the aperture and the spillage subsequently heats the shield plate to temperatures of up to 300 °C which in turn preheats the induced air flow temperature before it enters the cavity. The effect of prolonged spillage and high-temperature exposure can be observed in Figure 28 where the paint on the shield plate has been discoloured.

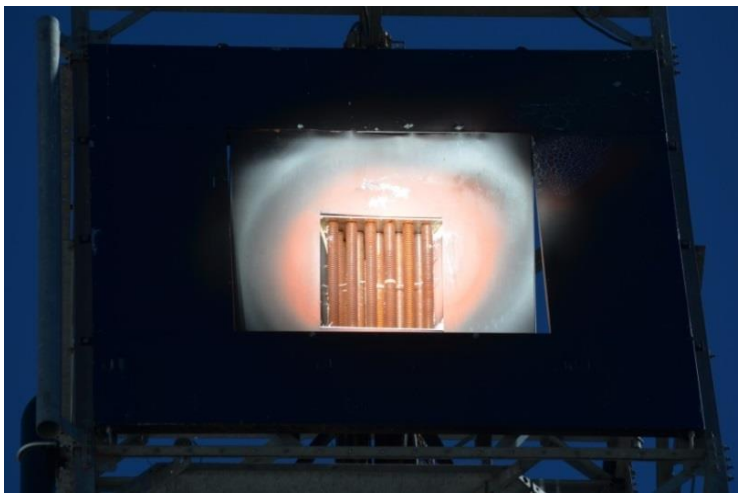

Figure 28: Shield plate paint discolouration during operation

The side walls of the cavity were painted black, to simulate the re-radiation from neighbouring tubes in a larger receiver, instead of a reflective surface coating which could enhance the depth of penetration into the cavity. This side wall of the cavity was heated significantly by the incident radiation from the heliostats not falling perpendicular onto the aperture.

6.3.2. Physical response to testing

Internal fouling resistance needs to be taken into account when designing a heat exchanger. Different fluids contribute different thermal resistances due to fouling. Compressed air has a fouling resistance value of 0.35e+3 $[W/m^2K]^{-1}$ and the water used in the experimental setup has a fouling resistance value of 0.2e+3 $[W/m^2K]^{-1}$(Mills and Ganesan 2009). These values were used to increase modelling accuracy. The experimental testing was conducted in a short period of time after a period of commissioning. As a result, it was assumed that the effects of fouling remained constant for the tests.

Externally the onset of surface oxidation increases the surface solar absorptance which is beneficial (Yellowhair *et al.* 2015), the surface emissivity does however also increase by more than double. To reduce the increased radiative losses the surfaces with higher view factor to the environment needs to be cooled more effectively. Ideally, the tubes close to the aperture will have a higher reflectivity, increasing penetration depth, whilst tubes deeper in the cavity will have increased absorptivity.

The oxidation before and during tests are depicted in Figure 29. In the test where the receiver was operated as an open volumetric receiver, the surface temperature of tubes at the aperture rose to more than 700 K. The darker discoloration of the oxidation observed Figure 29b was during this test.

(a) (b)

Figure 29: Oxidation observed after some time of exposure to the environment and incident radiation from the heliostat field (a) Low temperature and (b) High temperature

6.4. Conclusion on experimental work

The experimental results were documented in this section with regards to the circumferential temperature difference, the cavity thermal conditions, the heat removal relationship between the two fluids and the volumetric capability of the staggered finned tubes. This was followed by a sensitivity analysis of the receiver behaviour with regards to environmental influences. Lastly, some experimental observations were discussed

The experimental campaign yielded data which can be used to validate future simulations of the modified HPAR. The setup was able to demonstrate the effectiveness of the receiver to capture the incident radiation, reduce the circumferential thermal gradient and resist the convective losses to wind over the aperture.

The experimental results highlighted the challenges faced by CSP receivers in terms of component control. The modified HPAR demonstrated good controllability by means of mass flow rate variation. The test further demonstrated the ability of the design to control the material temperatures by the secondary fluid stream, an alternative solution to the PML tubes in the SOLHYCO project which obtains similar results.

Chapter 7

Conclusions and recommendations

The experimental investigation undertaken gathered data on the thermal behaviour of the modified HPAR with external fins added to the tubes. The tests were conducted at the STERG roof laboratory on the receiver test tower for a total duration of 34:45 hours.

Conclusions:

All of the objectives of the study was met. A review of the current tubular air receivers was done and the relevancy to the modified HPAR was discussed in the literature chapter. The effect of the radial fins and the induced flow was measured in the experimental work.

The data was analysed to determine the sensitivities of the experimental modified HPAR to variations in the operating conditions. The collection efficiency of the modified HPAR in the Helio40 test laboratory was measured and evaluated in the results chapter. The receiver thermal response for the duration of all the tests was captured to enable the validation of future simulations and studies.

Key findings

The induced flow demonstrated the ability to trap the convective losses without a need for a closed cavity. In the sensitivity analysis, it was found that the receiver in the tests was fairly insensitive to wind loads. The potential to obtain constant efficiency receiver output by means of variation of the two fluids was demonstrated in the tests.

The induced flow and added external fins demonstrated the ability to reduce the circumferential temperature gradient, potentially reducing the effect of the cyclic thermal fatigue commonly experienced by central receivers. This could enable metal tubular receivers to operate in higher incident flux environments than previously possible.

The HPAR concept, in general, showed the potential to solve the thermal requirements and eliminate the bottle-neck problem of the SUNDISC

cycle. However, the relationship between the two fluid streams is inversely proportional, thus an increase in energy transferred to one relates to a decrease in the other. The available mass flow rates at the desired conditions are of concern in the case of a commercial receiver. If a lower temperature requirement exists at the plant, the non-pressurised air stream can potentially meet that need. Through modelling by Heller (2017) the modified HPAR receiver has demonstrated the ability to reach the desired temperatures of the internal pressurised fluid.

For successful Brayton cycle integration, the material temperatures in the receiver need to be in excess of 800 °C during operation to ensure the desired outlet temperatures can be met. The goal to find a receiver capable of achieving these material temperatures with minimum one start-up and shut-down per day for 25 years is of higher importance than high receiver efficiency. In this regard the modified HPAR demonstrated the ability to better control the receiver temperature distribution which can potentially extend the fatigue life of tubular air receivers.

Recommendations:

The experimental behaviour could be reproduced, within a margin of error, by a simple numerical model, confirming the ability of the theory to predict the system response. Based on this finding a potential future 3-D simulation model can be validated with the experimental results. Such a model will, however, be computationally expensive due to the complexity of the finned tubular geometry of the modified HPAR.

With the cost of PV being significantly lower than CSP the goal to compete by day appears futile. The focus should rather be on penetrating the market segment which is out of reach for PV, namely the evening and morning peaks. For this the TES charging should be maximised during the day, thus shifting the priority of the HPAR to heat the NPA.

As suggested by Heller (2017) another option is the addition of a wire mesh volumetric receiver similar to that developed by Nel (2017) at the back of the cavity to increase the NPA outlet temperature to the required TES charging temperature. In such a setup the tubes are arranged with larger open porosity to increase the penetration depth.

The addition of a volumetric receiver at the back of the cavity which is sparsely populated is in a sense not an HPAR, but instead two

independent receivers in the same cavity. This begs the question whether two independent receivers in close proximity should be used instead and the heliostat field focus be varied between the two as required.

The substitution of the bottoming Rankine with an organic Rankine cycle can be investigated in the future as an alternative. The organic Rankine cycle can generate electricity from low to medium temperature heat sources making it a good candidate for integration with the rock bed TES and the non-pressurised air output of the modified HPAR.

Appendix A: Geometry design results

As mentioned in the main body of the report three design layouts were generated and evaluated by doing a 2-D DO simulation of the layouts in ANSYS Fluent 18.2 to determine which of the three designs have the best radiation penetration values.

Based on the paper which was presented to SolarPACES 2013 by *Craig et al.* (2013), in which a layout optimization study for the HPAR was carried out, the trend was to have an oval shape of the tube layout with large spacing in the front and smaller spacings toward the depth. One such a design was generated as depicted on the next page.

Kretzschmar (2014) used a staggered arrangement for the experimental setup, similar to the staggered arrangement in conventional heat exchangers. This helped to characterise the air flow development by using correlations for tube banks in induced flow. There exists limited data with regards to radiation penetration into the depth of tube banks.

The nature of volumetric receivers is to have the porosity decrease gradually into the depth. The staggered layout was generated as a non-standard spacing staggered arrangement with the first two columns set to absorb most of the temperature and create a radiation heat loss barrier for the deeper tubes. From the third column onward the layout was designed to condition the flow and force the flow to move towards the receiver centre line and mix before exiting the receiver.

In the design modelled by Heller (2017) the open porosity was kept constant for different fin geometries. Heller chose a generic design which featured the first couple of tubes in line and the offset occurring deeper. This design was aimed at having the highest tube temperature at the back of the receiver, thereby creating the volumetric effect. Arguably this was the best design from the three literature designs mentioned, however the flow mixing in the first rows will be ineffective and hot spots may occur. To replicate this design to some extent and drawing from nature a spiral layout for the tubes which increased tube density toward the depth was designed.

For the practicality of the construction, it was decided to position the tubes in columns which can be connected to a manifold.

Geometry considerations:

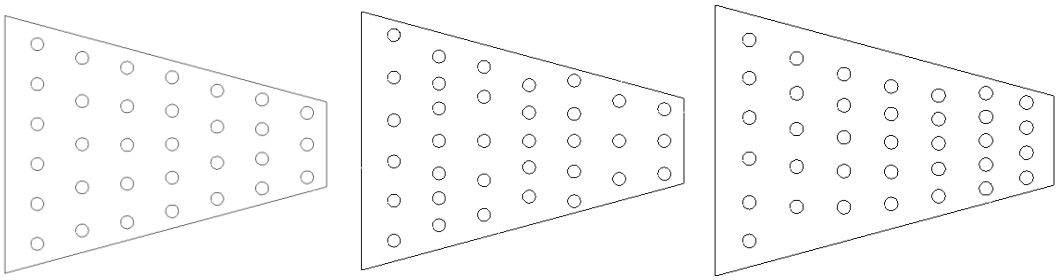

Staggered layout Oval layout Spiral layout

The radiation penetration simulation as discussed earlier was carried out for the three layouts depicted above.

In an attempt to better visualise the difference in the absorption capabilities of the tubes the average absorbed heat flux per tube column was taken and plotted in Figure 30. This was assumed to be an acceptable measure since the average flux per column is a directly comparable value of quantity absorption for each receiver layout at that depth of penetration. It is important to keep in mind the number of tubes in the row of the receiver under investigation. More tubes will result in a lower average even though a larger quantity of energy is absorbed in the row.

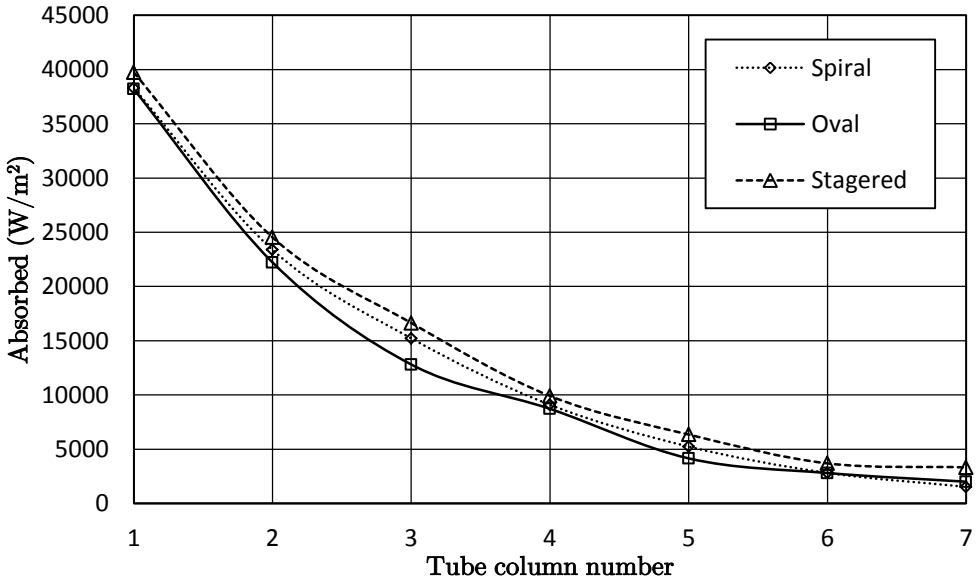

Figure 30: Average absorbed flux per tube row

The plot in Figure 31 indicates the average deviation from the mean circumferential absorbed flux. A large deviation indicates peaks in the absorbed flux (direct impact). A lower average deviation is indicative of better circumferential absorption which is a result of reflected and re-radiation between tubes. The oval layout exhibits a wavy distribution towards the back of the receiver which can be attributed directly to the variation in tube numbers per row.

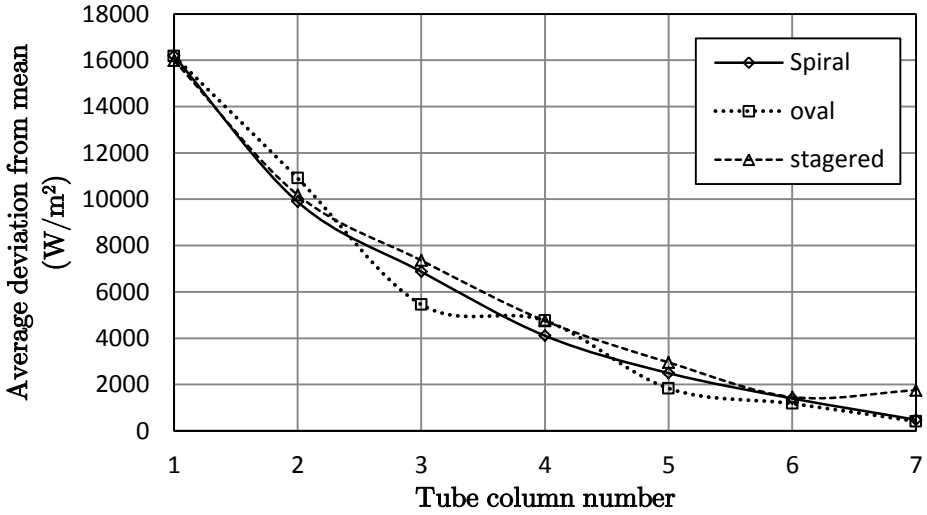

Figure 31: Average deviation from the mean

In Table 8 the results, depicted in the graphs, of the radiation penetration and absorption investigation is summarised numerically. From the values obtained it can be concluded that the staggered arrangement is the best layout of the three in terms of overall power absorbed.

Table 8: Summary of the radiation absorption capabilities of the different cavity layouts

	Average absorbed flux (W/m^2)							
Row	1	2	3	4	5	6	7	
Spiral	38305.82	23384.45	15225.23	9096.658	5239.924	2818.103	1531.019	
Oval	38200.07	22225.11	12811.42	8718.709	4151.122	2803.474	2002.544	
Staggered	39742.01	24532.71	16638.9	9910.156	6350.959	3693.058	3326.79	
	Total average absorbed per row (W)							Total
Spiral	12937.85	2938.576	1913.259	1143.12	658.4682	354.1333	153.9148	12937.85
Oval	13260.05	3910.046	1609.931	1095.625	521.6453	211.3769	150.9883	13260.05
Staggered	13672.65	3082.871	2090.906	1245.347	638.468	371.2667	250.834	13672.65
	Average deviation from the mean (W/m^2)							
Spiral	16186.18	9886.814	6870.666	4105.257	2490.489	1398.789	479.5605	
Oval	16180.82	10907.36	5448.829	4757.65	1834.203	1176.175	408.1806	
Staggered	15991.75	10186.41	7357.571	4748.418	2953.027	1458.944	1752.792	

In future work an optimization of the discrete locations of the tubes can be done which will build on the work done by (Craig *et al.* 2013). That is however beyond the scope of this project.

Figure 32 depicts a comparison of the incident radiation distribution in the cavity for the three different arrangements. The top left figure is that of the staggered arrangement. The top right figure is that of the oval arrangement and the bottom figure is of the spiral concept. The density of the tubes in the oval arrangement is observed to reduce the incident radiation penetration in comparison to the staggered and spiral arrangement for an identical inlet boundary condition.

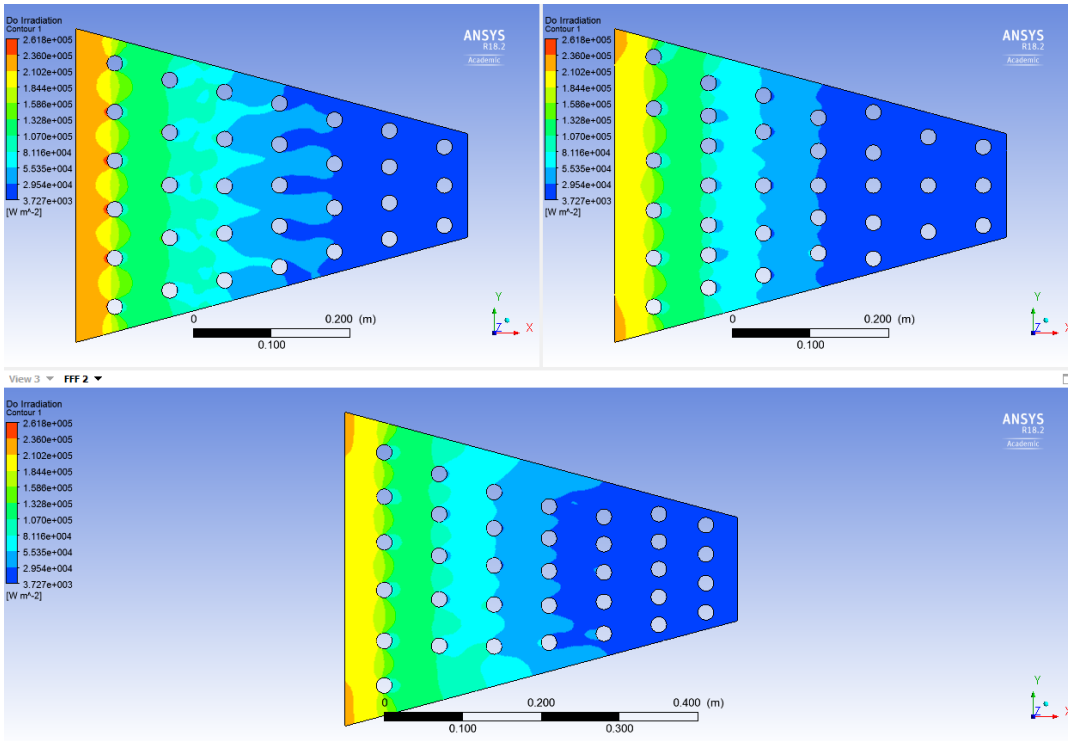

Figure 32: Radiation penetration mapping in the three proposed cavity layouts

Appendix B: Thermal stress analysis

Tube failure/rupture with 700 K fragments has the potential to seriously harm structures and people. The temperature distribution in Figure 33a was obtained from a worst case scenario 3D DO simulation. In the simulation, 60 kW/m^2 incident radiation (twice the intensity capability of the Helio40 field according to Grobler (2015)) was applied in the negative x-direction to a single finned tube to ensure maximum effect. To further amplify this stress analysis it was assumed the tube has atmospheric air internal and external which minimises the heat removal, thus yielding a worst-case scenario prediction.

The eventual experiment had water as internal fluid which greatly decrease the surface temperature due to the higher heat removal. This obtained temperature distribution depicted in the Figure 33a was imposed as a boundary load to obtain the thermal stresses present in a generic tube of this geometry (Figure 33b).

This 3-D DO simulation was set up with 10 by 10 theta and phi division discretizations for each impact. Due to the computationally expensive nature of the geometry, this was sufficient for a preliminary investigation.

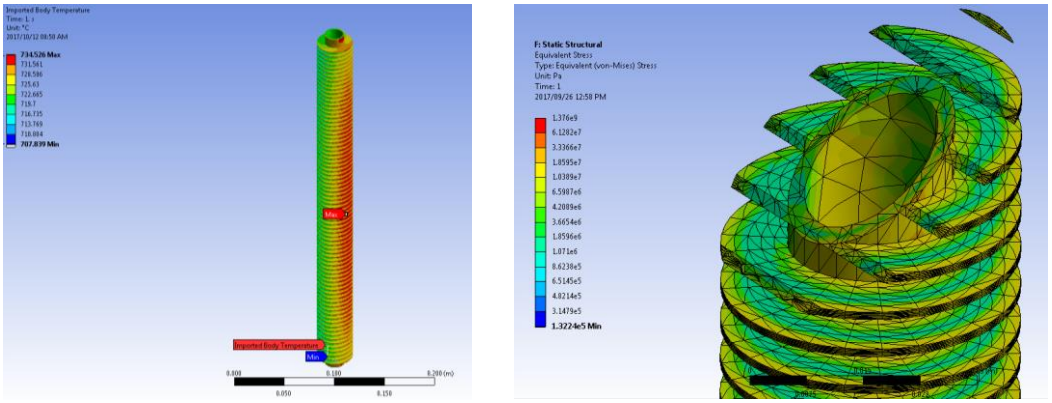

(a) (b)

Figure 33: a) Temperature distribution on a finned tube in worst case scenario 2 times the incident flux and b) Stress distribution on the circumference of a finned tube in the unidirectional radiation environment

For the static structural analysis a worst case scenario, where there is no heat removal internal to the tubes, was assumed. The ends are supported

in a fixed position, limiting the banana effect of the non-uniform expansion of the tube due to the non-uniform heat load. The stress concentrations can be found at the points where the tubes are fixed to the supports. The highest observed stress is more than the yield strength of the material.

This peak stress is a compressive stress generated by the boundary condition which restricts thermal expansion. The higher than yield strength stress is however acceptable since the constraint is restricting expansion and thus restricting rupturing of the tube.

As discussed in section 4.1.6. the magnitude of thermal stress increases significantly when expansion is restricted. The predicted thermal load on the surface is then in the vicinity of the predicted surface temperature from the MATLAB model at the simulated conditions.

The experimental manifestation of the receiver has the tubes spot welded into position in clearance fit holes in the locator plates. This clearance and spot-welds should allow for expansion and contraction of tubes during operation.

Appendix C: Experimental procedures

Operating procedure:

1. A minimum of four hours prior to climbing the tower an email from the work item leader must be sent to the relevant persons in charge of the roof lab.
2. Indicate that the test is about to take place, hanging a sign and activate the warning lights at the roof lab.
3. Start the data logger and check that all the sensors are active.
4. Start the water circulation system.
5. Check for water leaks and that the water system is running.
6. Turn on blower on desired setting.
7. Calibrate the heliostats on the calibration target individually.
8. Move heliostats onto the receiver and track.
9. Run the test for the desired time.
10. Defocus the heliostats when done.
11. When the all the heliostats are defocussed the pump and fan can be shut down once the surface temperatures dip below 50 °C. This will ensure that the water does not boil and damage the system with pressure build up
12. Stop the data loggers.

Appendix D: Calibration data

D.1 Calibration error estimation

The most important measurement for this investigation is the relationship between the flow rates and the temperature distribution in the receiver cavity. The temperature measurements are carried out by type-T and type-K thermocouples which have an uncertainty of +-1 °C or +-0.75 % (whichever is greater) and +-2.2 °C or +- 0.75 % (whichever is greater) respectively.

The thermocouples were connected to a National Instruments data logger. The National Instruments data logger (cDAQ-9174) with two NI 9213 temperature cards fitted has a reported error range of +-1°C for both the type-T and type-K thermocouples. The combined root sum square uncertainty at the maximum expected temperatures of 100 °C for air and 400 °C for the surfaces are $\sqrt{(1^2) + (1^2)} = \pm 1.41℃$ for type-T thermocouple readings and $\sqrt{3^2 + 1^2} = \pm 3.162\,℃$ for the type-K thermocouples. The thermocouples were calibrated over the range of operation with a FLUKE 9142 dry well calibrator.

The ambient temperature measurement was obtained from the weather station. The weather station has a CS215 temperature and relative humidity probe with an ambient temperature measurement accuracy of ±0.4 °C (Campbell Scientific 2009) in the range of 5 °C to 40 °C installed. The weather station has minutely data resolution.

For the air mass flow rate, a Venturi flow meter is used with pressure and temperature sensors to determine the flow rate and density. The volumetric flow rate is measured with a differential pressure transducer which is connected to the pressure taps at the Venturi throat and upstream. The MPX2100 series differential pressure transducer used has a reported ±0.25 % linearity over the full-scale voltage span of 0 to 40 mV (Freescale 2009) which relates to ±0.1 mV.

The pressure transducer was connected to the data logger and calibrated against a Betz micro-manometer which has a reading accuracy of ± 0.04 % over the range 0 – 5000 Pa (ACIN 2016) or ± 2 Pa. The calibration curve for the pressure transducer and data logger over the operating range can

be found in Figure 36. The pressure transducer provided an analog voltage signal to a NI 9213 card and data logger which has typical offset error of 4 µV, corresponding to ±5.062 Pa at the measured system sensitivity of 1.26 kPa/mV. Therefore the combined uncertainty of the pressure drop measurement is $\sqrt{2^2 + 5.062^2} = \pm 5.442$ Pa

The Venturi calibration curves can be found in Figure 34. The discharge coefficient was determined experimentally and the final error between the measured and calculated flow rate was ±1.45 % or ±0.001798 m^3/s at full range of the centrifugal blower.

For the water flow rate, an Arduino flow Hall-effect sensor was used. The sensor measures the number of rotor rotations when water flows through the rotor which is connected to a magnetic core. 4.8 pluses per second correspond to 1 ℓ/min. The specification sheet claims a 3 % uncertainty of the flow measurement. When calibrated and compared to a timed filling of a 5 ℓ container a measurement error of only 1.8 % was observed. Taking into account the human error, in terms of timing, it can be concluded that the estimated error of 3 % is reasonable which relates to ±0.21 ℓ /min at maximum operating flow rate during experiments. The calibration curve can be found in Figure 37 along with the correction function based on the error analysis. The flow sensor measures and logs the flow rate at 1 Hz. Post-processing of the 1 Hz resolution provides a better average over longer periods by using a mean fit.

The DNI measurement from the weather station is made with a Kipp and Zonen CHP 1 pyrheliometer which has an expected daily uncertainty of < 1 % (Kipp and Zonen 2018).

Table 9: Summary of experimental measurement errors over full range operation

Measurement	Error % on full range
Type-T thermocouple	0.705 %
Type-K thermocouple	2.635 %
Pressure measurements	2.268 %
Air flow rate	1.450 %
Water flow rate	3.000 %
DNI Error	1.000 %
Overall error	4.968 %

D.2 Calibration curves

The Venturi flow meter was calibrated relative to a bellmouth inlet. A bellmouth is an inlet device which provides flow conditioning from a large reservoir with a virtual zero beta ratio, and therefore close to zero flow losses. Using a differential pressure transducer the difference between ambient and throat pressure is measured with which the flow rate can be determined. The following equations from Cengel and Cimbala (2014) was used to determine the flow conditions in a bellmouth.

$$\frac{P_1}{\rho g} = \frac{P_2}{pg} + \frac{V^2}{2g} + \frac{K_l V^2}{2g} \tag{39}$$

$$P_1 - P_2 = \rho V^2 \left(\frac{1}{2} + \frac{K_l}{2}\right) \tag{40}$$

$$V = \sqrt{\frac{dP}{\rho * \left(\frac{2}{2} + \frac{K_l}{2}\right)}} \tag{41}$$

With $K_L = 0.03$ for a well-rounded inlet and the density of air on the day was 1.184 kg/m^3.

Using the measured flow rate the Venturi discharge coefficient can be determined using the following equations from Figliola and Beasley (2011) assuming slight compressibility of the air.

$$Q = CEA_0 Y \sqrt{\frac{2dP}{\rho}} \tag{42}$$

$$E = \frac{1}{\sqrt{(1-\beta^4)}} \tag{43}$$

$$\beta = \frac{d_0}{d_1} \tag{44}$$

$$C = \left(\frac{Q}{A_0 Y}\right) \sqrt{\frac{\rho(1-\beta^4)}{2dP}} \tag{45}$$

Using this method the discharge coefficient (C) of the Venturi was determined to be 0.763173 with an average error of ±1.445 % in the range of Reynolds numbers 4.62e+4 to 1.66e+5.

The discharge coefficient determined by testing is notably lower than published values, it was however assumed accurate for a machined unit at the given flow conditions. The Venturi dimensions are given in Figure 35.

During experiments, the air mass flow rate is determined based on the density of the air at the Venturi and the differential pressure. The density is a function of the fluid temperature and the volumetric flow rate a function of the differential pressure over the Venturi flow sensor.

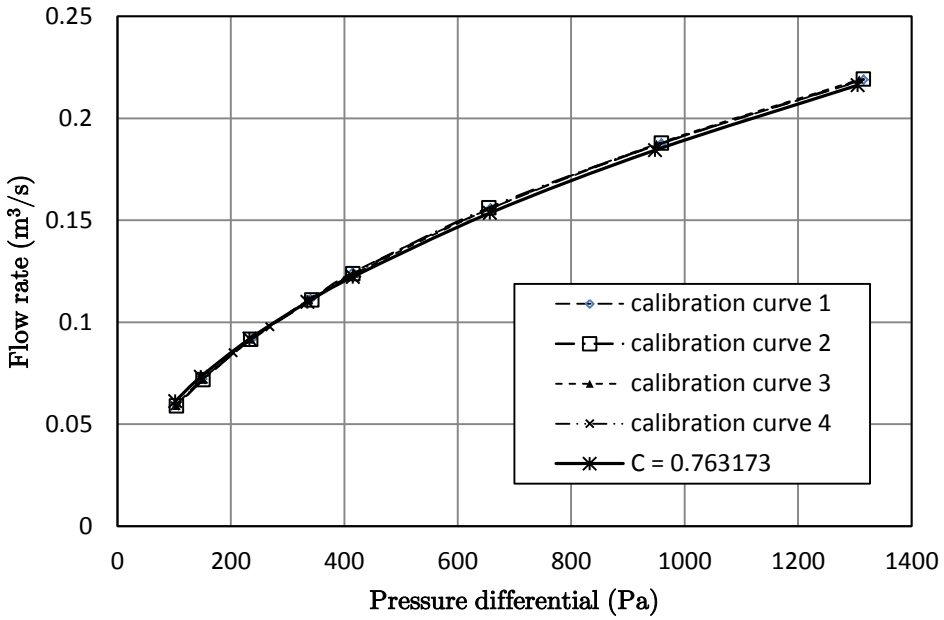

Figure 34: Venturi calibration curve

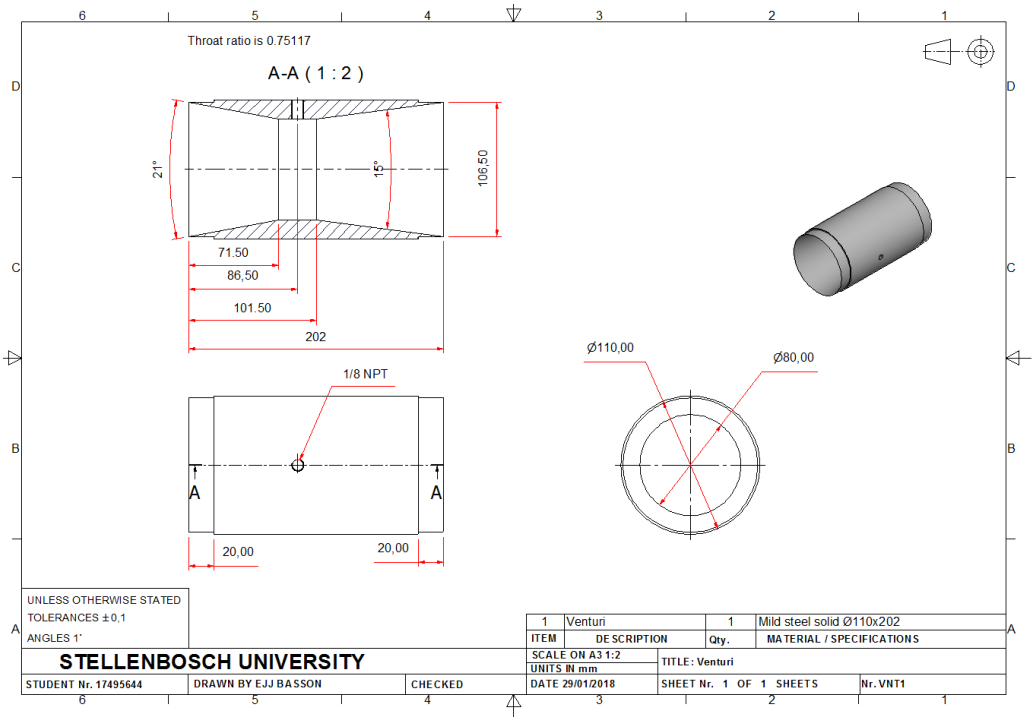

Figure 35: Venturi design dimensions

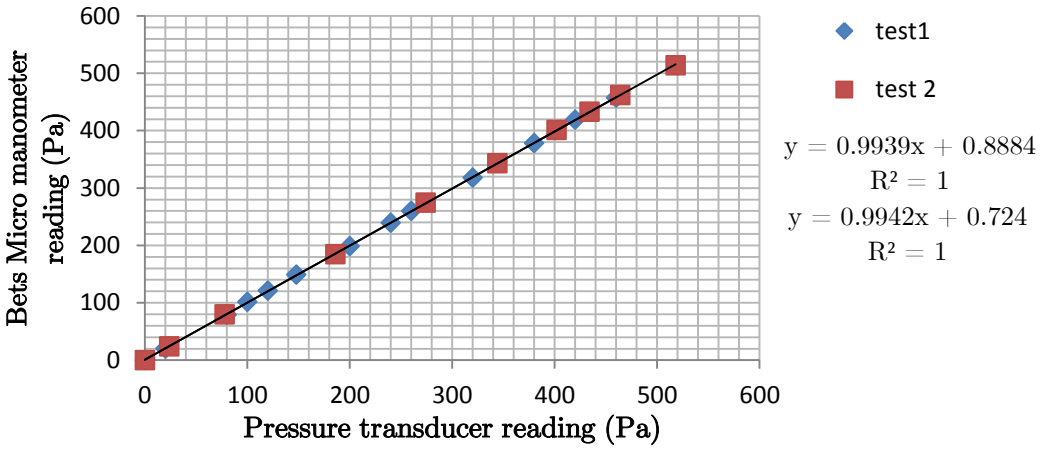

Figure 36: Pressure transducer calibration curve

Flow rate calibration curves of the hall-effect sensor flow meter.

For the calibration of the Hall-effect flow sensor, the sensor was connected in line with a water source. The water source was adjusted to provide a steady flow rate. The flow was then measured by timing the filling of a 5 l container. The 5 l volume mark was determined with a measuring beaker.

By using 5 l instead of 1 l, the timing uncertainty is decreased thereby improving the time-averaged flow rate accuracy. The following curve was generated correlating the positive displacement measurement to the Hall-effect sensor measurement. A linear trend line was added to determine the correction factor needed in the range of operation.

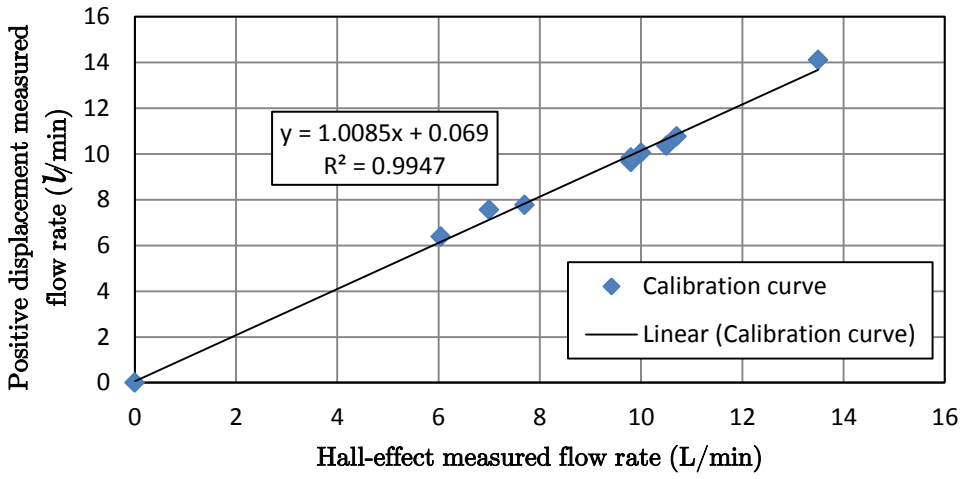

Figure 37: Hall-effect flow calibration curve

Appendix E: Heliostat field characterization

During testing, it was observed that the receiver shield plate indicated in Figure 42a, is almost completely illuminated. As mentioned in Section 5.5. at the time of the experimentation, there was no device capable of measuring the incident flux intensity. To consolidate this shortcoming a visual inspection was launched where the individual heliostat reflected images were photographed on the Lambertian target. This visual inspection was compared to Tonathiuh to provide some insight into the fluxes experienced.

E.1. Heliostat field geometry observations

The heliostats are numbered and grouped into two groups namely the pod and the roof (Figure 38). The pod was an early prototype of the eventual Helio100 heliostat development project and as a result, most of the heliostats on the pod are unique with small design differences. The roof heliostats were constructed later and all are based on the same design. The roof heliostats all have a similar reflected image as opposed to the variations in the images of the pod. This is illustrated later in this Appendix.

Figure 38: Heliostat layout as viewed from the receiver

The pod heliostats are spaced closer together and are situated almost perpendicular in front of the tower, resulting in a smaller focused image on the receiver since all the beams run close to parallel. It would seem that the pod provides higher quality focus than the roof heliostats which are spaced wider and over the relatively short distance to the receiver has an angle of almost 15° between Helio 7 and 12. However, in Figure 38 it can be observed that the pod is susceptible to shading and blocking losses when the sun moves closer to the tower, reducing the image quality.

E.2. Thermal distribution analysis

In an attempt to compare the observable focal image with the image produced in the Ray-tracing simulation thermal imaging was considered. A fluke infrared camera was used to measure the temperature variance on the receiver face and reconstruct the focal image on the aperture in such a way. Unfortunately, due to safety concerns, the readings could not be done close to the receiver and as a result, the spatial resolution is rather poor as can be observed in Figure 39.

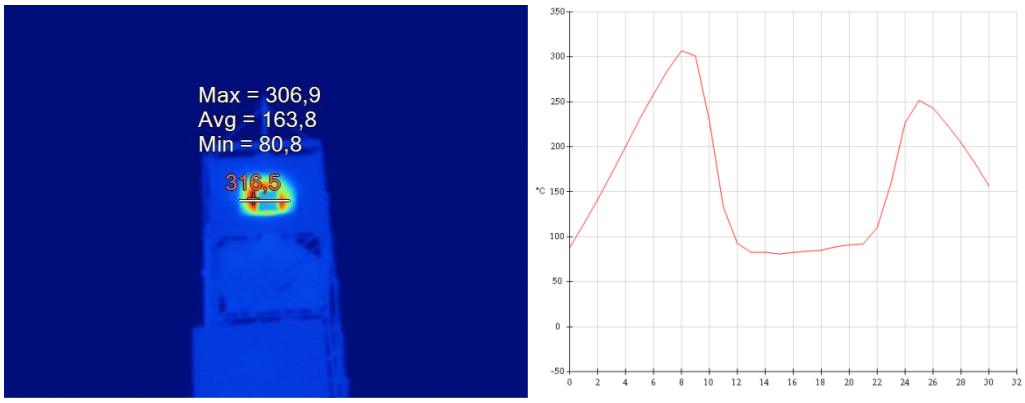

Figure 39: Thermal image of the spillage (left) and the graph of temperature intensity (right) on the selected line

E.3. Ray trace focal image

The following flux maps were generated at the times of photography of the images in the next section. The overall dimensions and the aiming accuracy can now be compared to increase the accuracy of the estimation. Table 10 lists the various area efficiencies defined by the available power on the aperture (POA) divided by the total theoretical power incident on the field aperture. $\eta_{SF} = \frac{POA}{DNI \times A_{SF}}$

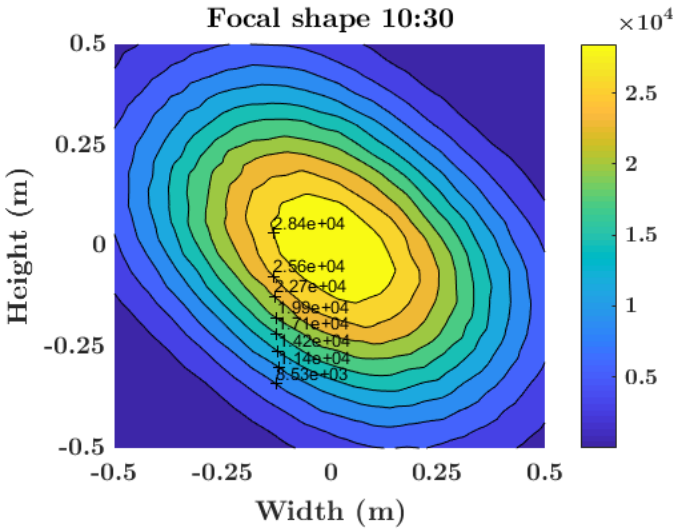

Figure 40: Predicted focal image 10:30 (E.4.)

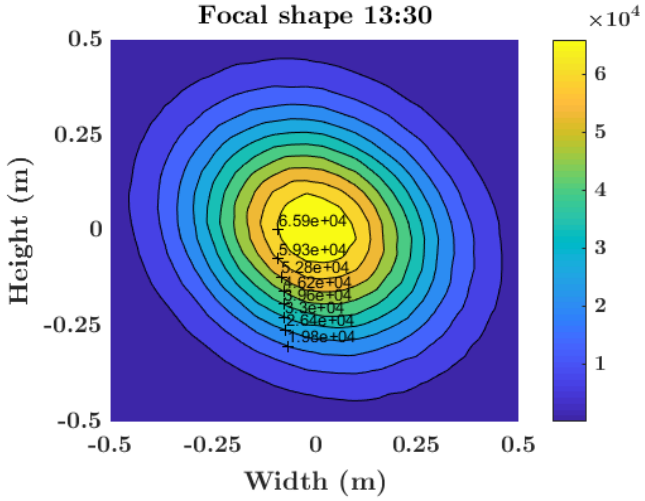

Figure 41: Predicted focal image 13:30 (E.5.)

Table 10: Solar field efficiency comparison onto the different areas

TIME	10:30	13:30
DNI	850 W/m^2	890 W/m^2
$\eta_{\text{2x2 m area}}$	0.608	0.803
$\eta_{\text{1x1 m area}}$	0.544	0.779
$\eta_{\text{0.4x0.4 m area}}$	0.186	0.363

E.4. Image comparison analysis

The zone of overexposure was determined for the image projected by the heliostats. The camera was used at the same settings for all the photographs per session to facilitate comparison. The exposure was not adjusted to provide a gradient from the maximum as it was not required for visual post-processing. This method resulted in the whole overexposed

area having a value of 1, thus outlining the peak flux area with no information on the intensity.

All of the overexposed areas were captured to be perfectly white. Using Microsoft paint the overexposed area was marked and is shown later in this Appendix. The crosshair dimensions, as well as the overall dimensions of the calibration target, can be observed in Figure 42b. The calibration target is situated about 4 meters below the receiver which leads to some distortion in the reflected image between the calibration target and the receiver. The peak of the focal point, however, is assumed to remain in the same area.

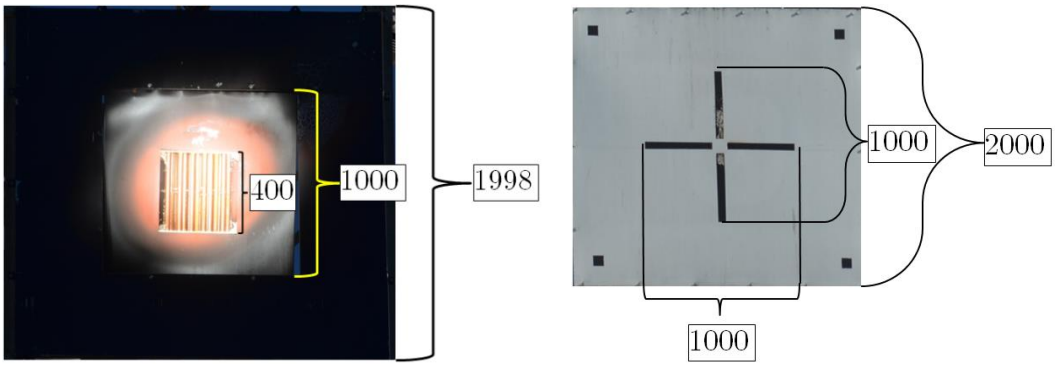

Figure 42: Heliostat focus locations: a) Receiver interface and b) Calibration target (all dimensions in mm)

In the following section, the various focal images at different times of day are presented. The eastern heliostat field has large cosine losses at the start of the day which reduces until sunset, where the sun was almost behind the tower. This continuous decrease in cosine losses suggests an increased performance of the heliostat field as the day progresses.

This is however not necessarily the case since the shading and block losses start to increase from solar noon onwards. Further, the cosine effect decreases the focal image size. This stems from the nature of the heliostats, being manufactured from flat mirrors which were bent into a semi-parabolic shape. As the cosine losses decrease the focal image size increases which result in more spillages when operating a small receiver aperture. This decreases the desired heliostat field performance somewhat. The change in focal image shape and size can be observed on the following four pages. Using the crosshair as length scale the overall area of the reflected light can be estimated.

E.4. Heliostat focal image shape at 10:30 am on 02/08/2018

Helio 1

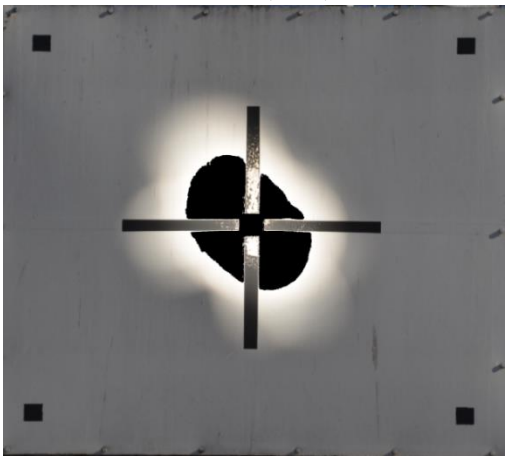

Helio 4

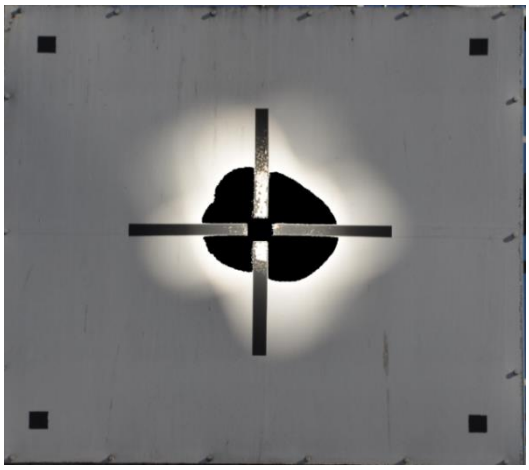

Helio 2

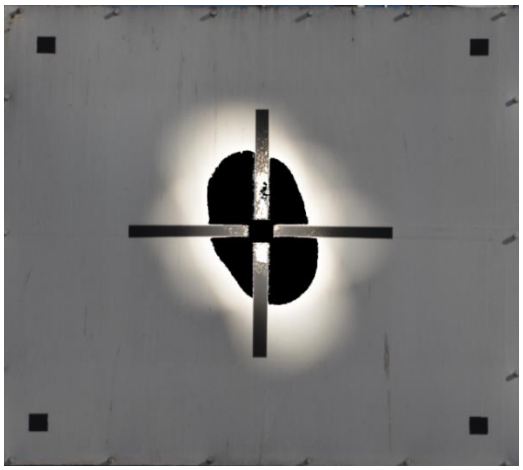

Helio 5

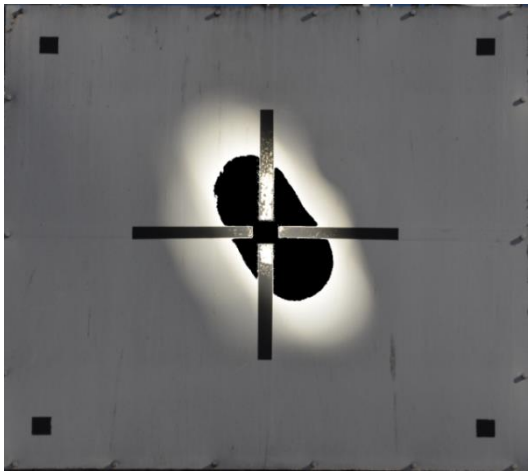

Helio 3

Helio 6

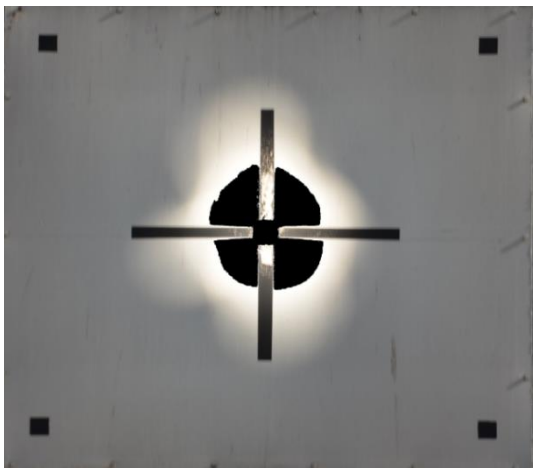

Helio 7

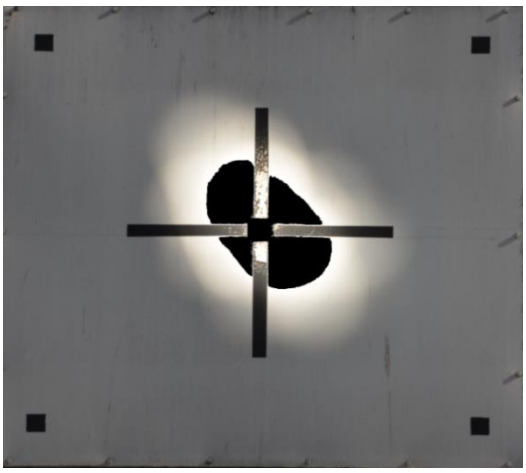

Helio 10

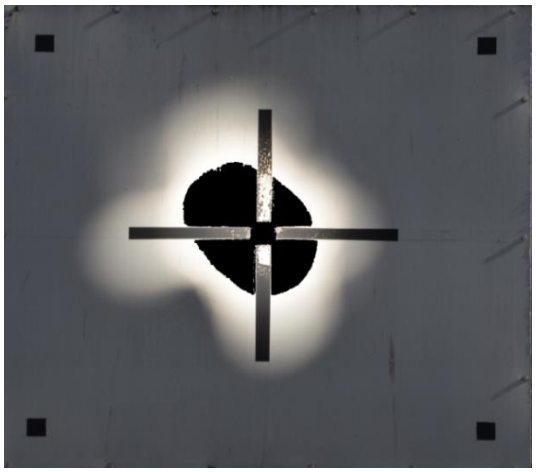

Helio 8

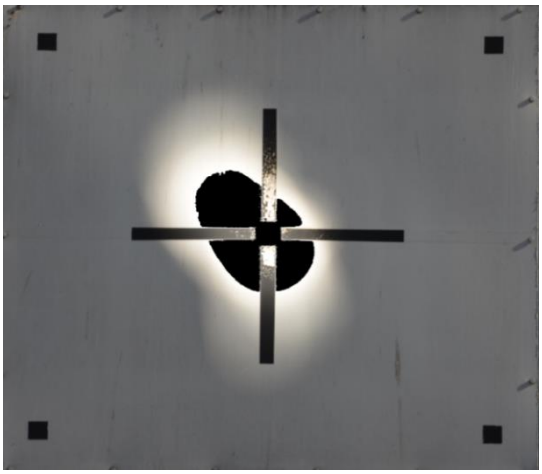

Helio 11

Helio 9

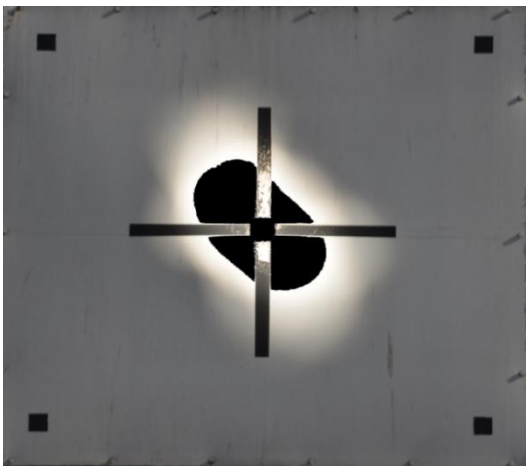

Helio 12

E.5. Heliostat focal image shape at 13:30 pm on 02/08/2018

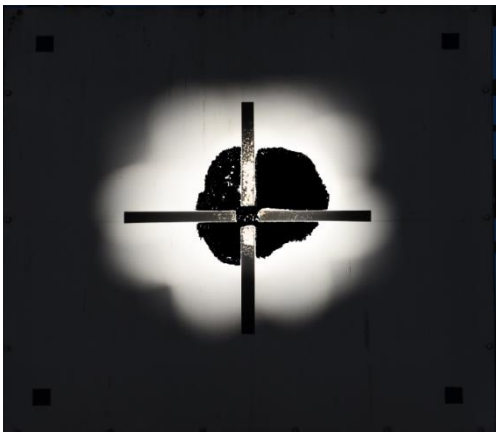

Helio 1

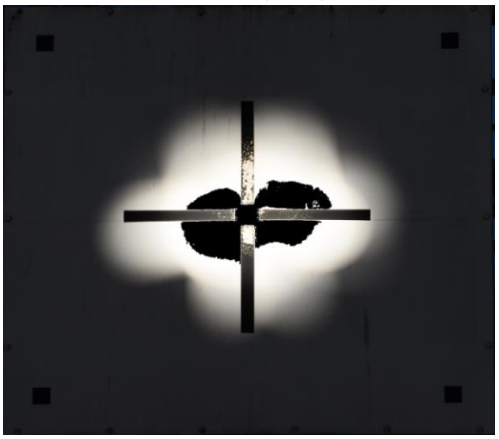

Helio4

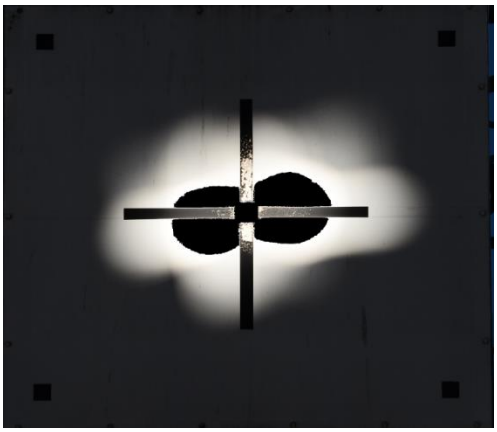

Helio 2

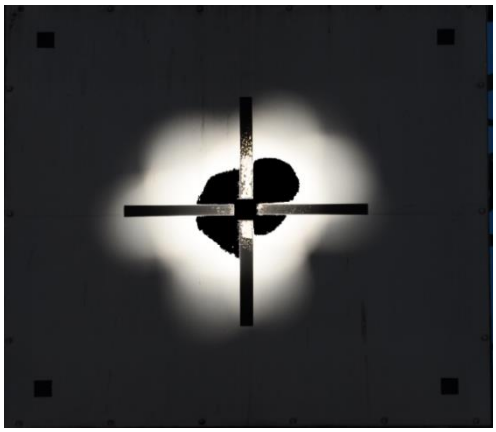

Helio 5

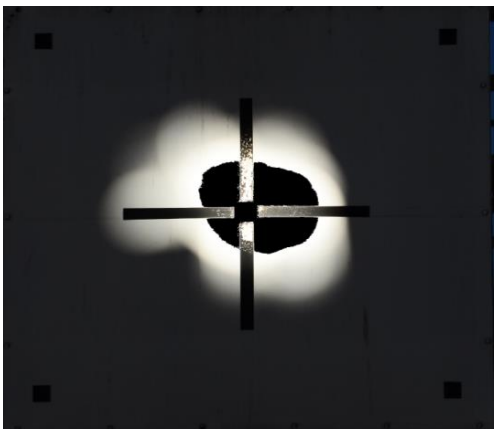

Helio 3

Helio 6

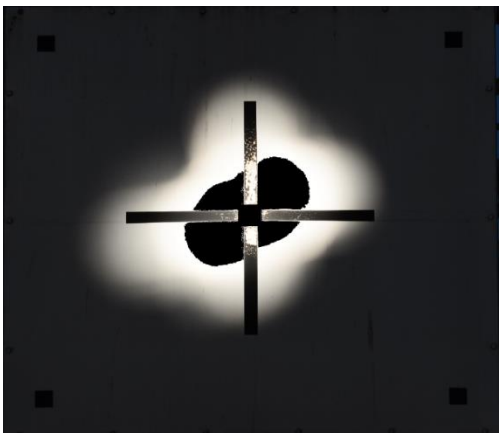

Helio 7

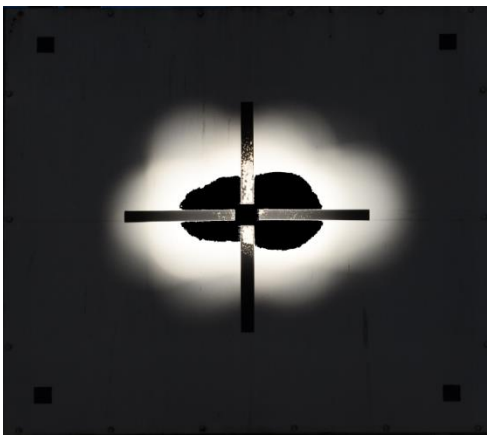

Helio 10

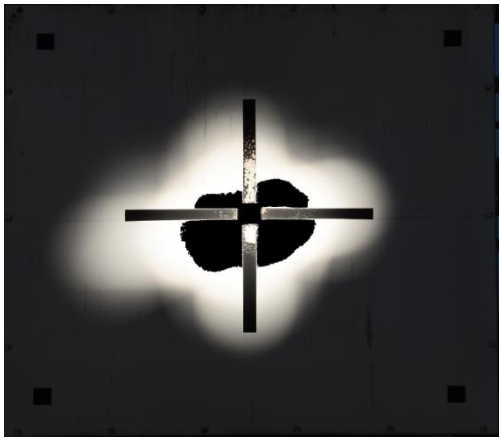

Helio 8

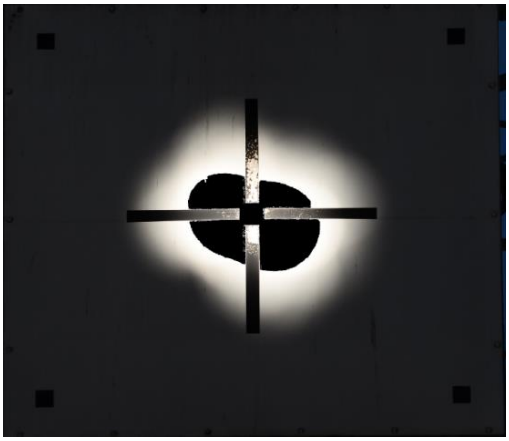

Helio 11

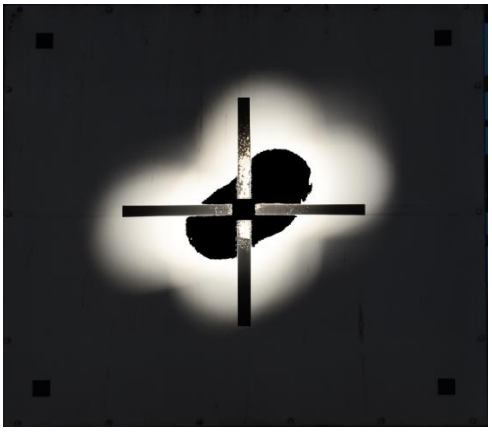

Helio 9

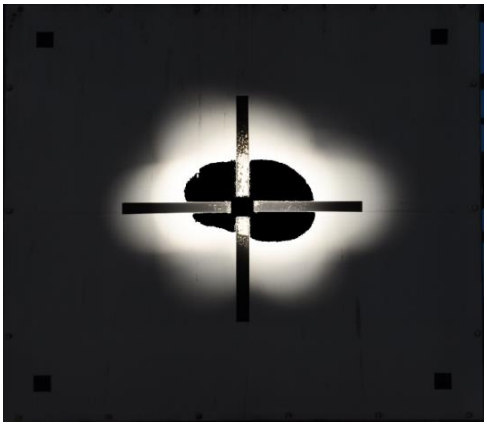

Helio 12

Appendix F: Results

The following sections provide the graphical plots of the measured system response of other tests during which interesting observations were made.

F.1. Sample results

The dips in the response on the 23rd July were caused by heliostat defocussing and refocussing minutes later. Fast thermal ramp-up times are demonstrated in Figures 43-45.

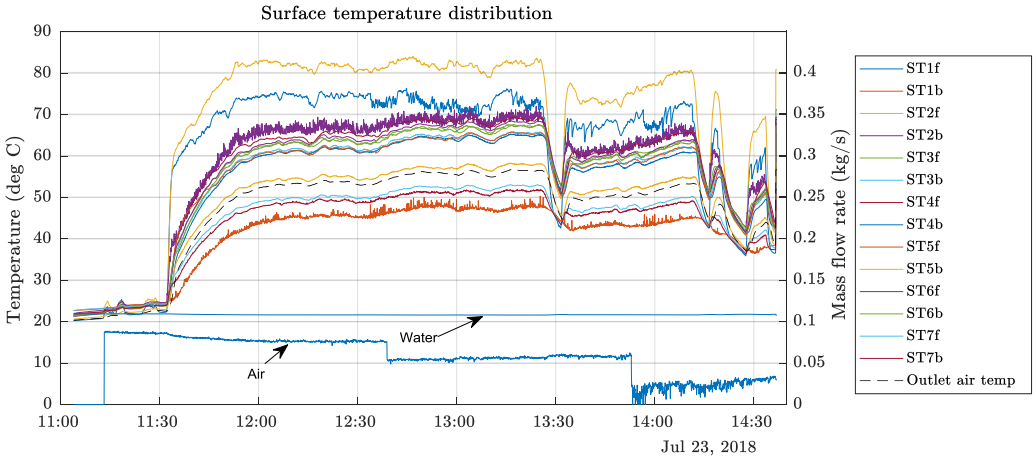

Figure 43: Surface temperature response on 23 July 2018

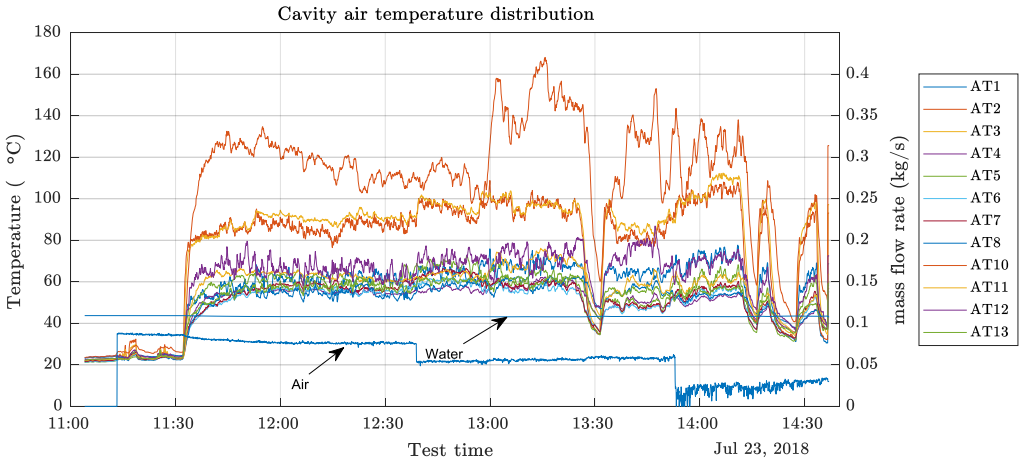

Figure 44: Cavity air temperature distribution on 23 July

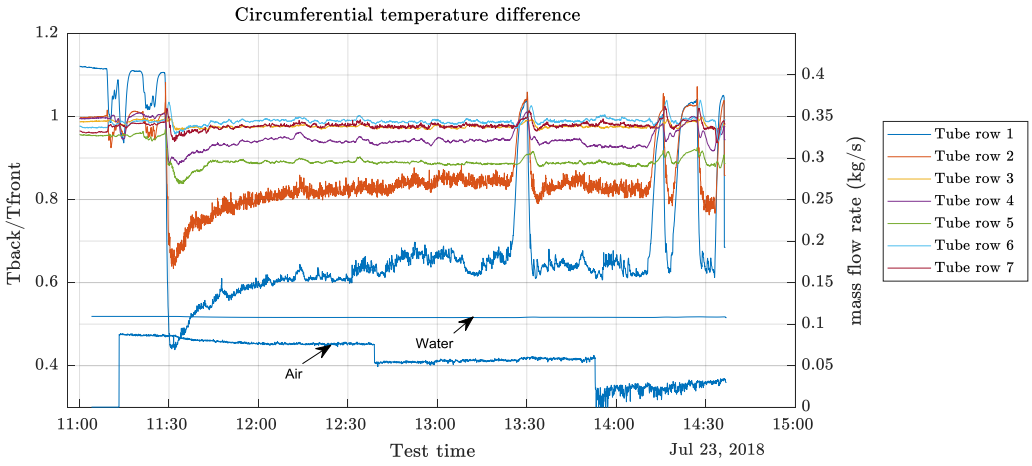

Figure 45: Circumferential temperature difference on 23 July 2018

The circumferential temperature difference response to variations in the external flow is demonstrated in Figure 46.

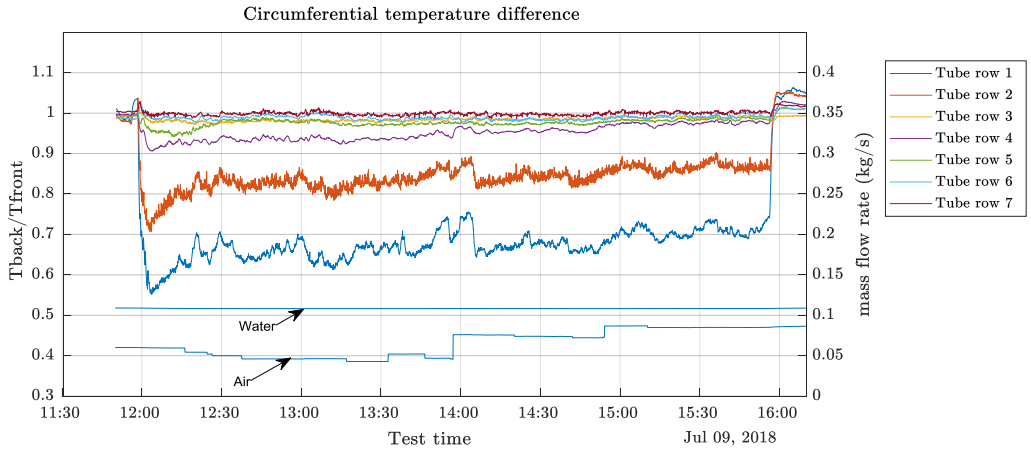

Figure 46: Circumferential temperature difference on 9 July 2018

Appendix G: Computer algorithm

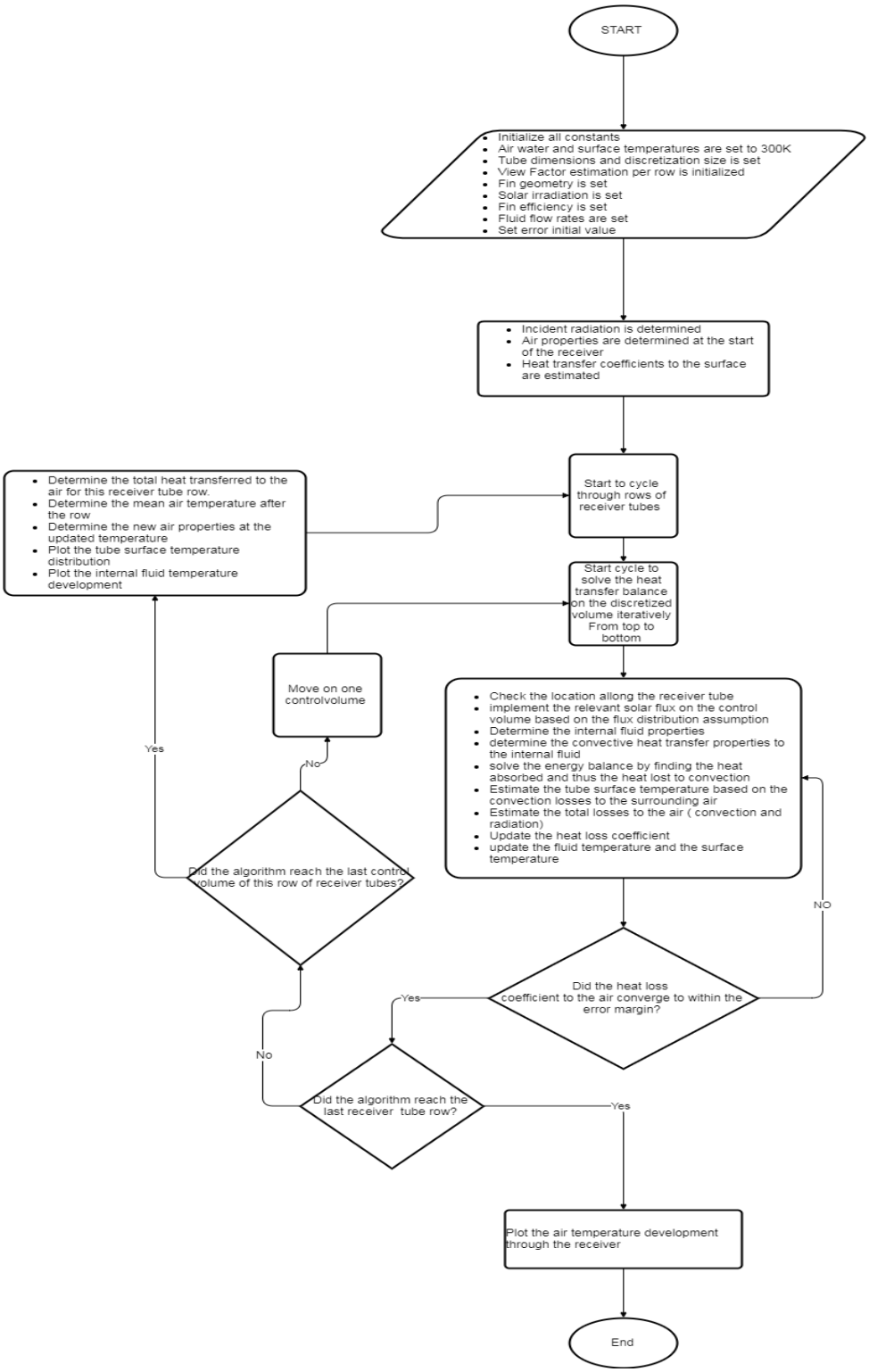

Appendix H: Simulation results

This chapter covers the simulation work performed to characterise the receiver based on the theory discussed in Chapter 4. A generic receiver was simulated which represents a section of the physical model and can be propagated in 360° to provide system performance predictions for a full solar field application. The modelling approach, based on the theory discussed in chapter 4.1, was presented at the 2018 SASEC conference (Basson *et al.* 2018). Several assumptions were made with regards to the flow and geometry which is evaluated and discussed in the experimental results section

H.1. Incident radiation estimation

The incident flux of the modelling control volumes was determined in two ways. The most accurate model was the Monte Carlo ray-tracing, which had to be repeated at each evaluation time slot. The less accurate but quicker method was by analytical estimation. The details of each are discussed in this section.

H.1.1. Ray tracing model

For ray tracing operations and flux distribution estimations Tonatiuh, a Monte Carlo ray tracer for optical simulation of CSP systems by the University of Texas at Brownsville, was used. The heliostat field and receiver were modelled as realistic as possible using the built-in functions of Tonatiuh. The heliostats were modelled as parabolic rectangles with the focal distance for each heliostat set to be the respective distance to the receiver. The physical mirrors were constructed from flat mirrors which were bent, resulting in slight variations in the focal image. The heliostat characterisation investigation can be found in Appendix E.

Aiming strategies are not part of this investigation and therefore all heliostats were aimed at the centre of the receiver aperture. Heliostat reflectivity was set to be 0.88 which is a conservative figure. The pillbox sun shape was used with 0.00465 thetamax.

Tonatiuh has been compared to SolTrace and the results presented at the 2009 SolarPACES international symposium. According to Blanco *et al.* (2009) the differences between the two programs over various simulations never exceeded 2.4 % and were negligible in most cases. This validation by Blanco is assumed to be sufficient for this investigation. At

the time of the investigation, there was no device or method to measure the incident flux at the receiver test facility. This lack of instrumentation led to the macroscopic investigation of energy harnessed as discussed in section 5.5.

The following figures illustrate the field layout and ray paths at 15:00 on the 5th of March 2018. Figure 47 illustrates the field layout and Figure 48 the basic receiver constructed from flat and tubular receiver components to represent the test receiver most accurately. Tonatiuh possesses the ability to import a CAD model onto which the rays can be projected. That function was however not used in this project since the geometry was considered to be too complex.

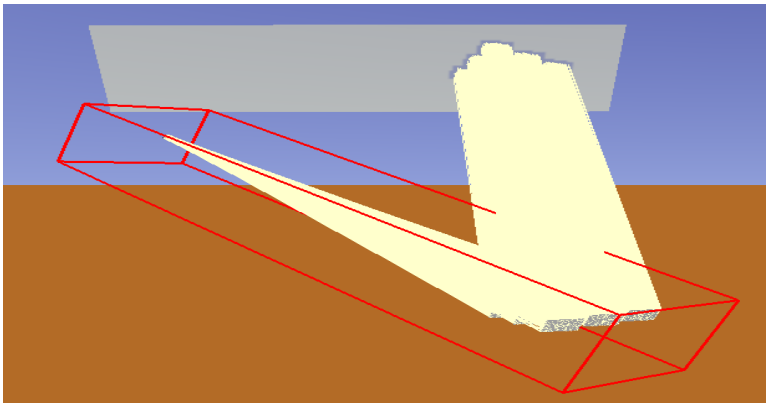

Figure 47: Ray paths and 6 Heliostat field layout

By exporting the incident flux the ray-tracing can be coupled with a 3-D finite volume investigation of flow in the receiver by applying the flux distribution as a boundary condition. This is achieved by creating a volumetric heat source in the first surface layer of similar magnitude to the flux distribution. The method is discussed in the paper by Moghimi, *et al.* (2015).

The base tube diameter was used to model the receiver tubes and a reflectivity value of 0.1 was chosen. This diameter assumption stems from the fact that for assumed perpendicular incident radiation the fins are 80 % open porosity. By using the smaller diameter more realistic penetration data can be obtained for rays passing through the fins deeper as opposed to tubes with fin tip diameter.

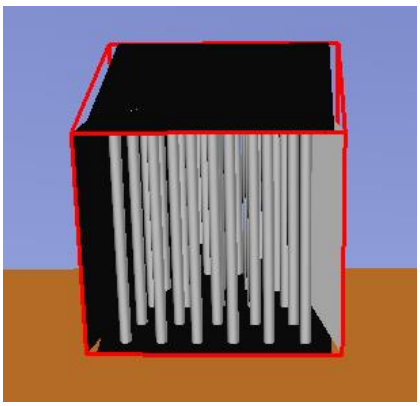

Figure 48: Receiver model on which the flux penetration maps were evaluated.

The flux projection, in Figure 49, was done in MATLAB to visualise the radiation penetration on the 7 selected tubes. The aspect ratio of the plot is skew to better fit all the tubes. The flux intensity on the first two tube columns is higher since both have an unblocked view of the heliostat field. Tube columns 3 and 4 are directly behind column 2 and only receive reflected radiation from within the cavity. Tube column 5 is at an offset from tube columns 3 and 4 and therefore receives some direct irradiation. The last two tubes rely mainly on radiation reflected into the depth of the receiver.

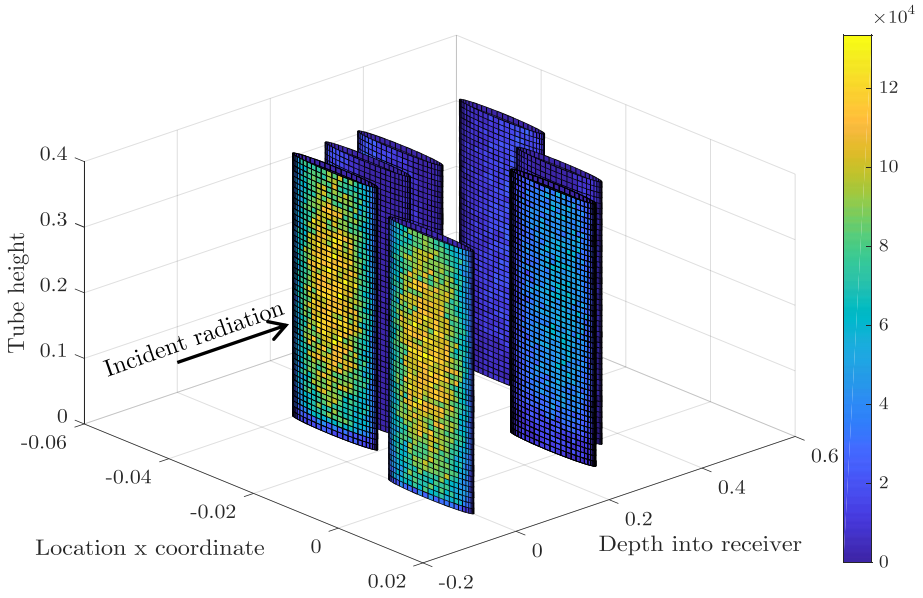

Figure 49: Flux mapping on the selected tubes generated with the ray data from Tonatiuh and plotted in MATLAB

H.1.2. Models with analytical flux distribution estimation

To account for the unidirectional behaviour of the incident flux distribution, the other two models use approximations and assumptions. The incident flux distribution and intensity on the aperture is approximated by reading in weather data from the pyranometer of the Sonbesie weather station 60 meters from the heliostat field centre. Hourly and minutely data is freely available and can be used to approximate the operating cycle of the heliostat field throughout the day by modelling the solar position and doing virtual tracking of the heliostats to estimate the cosine losses. The model solves the steady-state response of the receiver and needs to be altered should an operating cycle be modelled.

The Helio40 heliostat field is said to have a concentration ratio of 50, however, the assumption in the model was that, accounting for losses, the focal point is the size of the aperture. This assumption covers the scenarios where a smaller number of heliostats are used. The overall heliostat field efficiency, used to estimate the incident radiation intensity, is determined by Eq. 46.

$$\eta_{SF} = \eta_{ref}\eta_{shade\&block}\eta_{spill}\eta_{cosine}\eta_{absorb} \tag{46}$$

The ray-tracing model predicted a maximum solar field efficiency of 0.398 on a day of testing on a target with similar aperture. For the same day, the solar field and receiver efficiency was determined to be 0.3 at steady-state operation. This suggests that the receiver operated in the region of 75 % collection efficiency. The analysis on the spillage can be found in Appendix E. From a visual inspection the illuminated focal area covers roughly 1 $m^{2,}$ while the receiver aperture is only 0.16 m^2. This area comparison serves as an indication that the estimated field efficiency value is reasonably accurate for the macroscopic efficiency estimate.

Table 11: Input conditions for DNI based heliostat field model

Parameter	Value
$\eta_{reflect}$	0.88
$\eta_{shade\&block}$	0.90
η_{cosine}	0.95
η_{spill}	0.60
η_{absorb}	0.90
η_{SF}	0.40

An attempt was made to generate a Gaussian flux distribution on the tubes. This shape was approximated by a cosine function for $-\frac{\pi}{a}\ to \frac{\pi}{a}$ with

a being a variable 2≥a≥0. This variable is used to adjust the total absorbed incident radiation by changing the shape of the focal point. To account for the penetration of the incident radiation the incident flux was multiplied by a column specific fraction which was determined from the ray tracing exercise.

H.2. Modelling methods

The following section discusses the different modelling approaches taken to estimate the system response.

H.2.1. Model with tube flux distribution as input

The flux distribution depicted in Figure 49 is imported as an incident flux boundary condition. The incident flux map per tube is a 2-D matrix. In order to fit this matrix to a 1-D vector, the surface flux distribution per tube height row was smoothed with a 5^{th} order polynomial. A Fourier series approximation of the circumferential flux distribution, as done by Heller, was considered, but was decided to be beyond the scope of the investigation.

The next step was to generate an average circumferential incident flux per row using the smoothed curve thereby transforming the flux matrix into a vector. Lastly, a function was created of the average incident values along the length of the tube.

This function of average incident radiation on the circumference along the length of the tube is scaled to the discretised volume heights where it was implemented onto the whole control volume surface. This implementation assumption is made to approximate the normal distribution circumferential flux in 1-D.

H.2.2. Model with analytical flux distribution as input

For this model, it is assumed that the incident flux act on 50 % of the external circumferential area, defined by the fin tip diameter, of a control volume. This is a crude approximation of unidirectional incident radiation onto tubes which overpredicts the total incident energy onto the control volumes. Further, re-radiation and reflectance from neighbour tubes are not taken into account, thereby reducing the total flux absorbed by the receiver tubes. The fin heat transfer behaviour is approximated by finite fin height efficiency correlations.

H.2.3. Conservative model with different surface areas to the heat transfer modes

For this model, the same solar radiation input method was used as discussed in section 5.2.2. However, in this model, the incident radiation is implemented on an area representative of the perpendicular view of the finned tubes. The assumption is that all irradiation travels parallel and will therefore 'see' part of the base tube circumferential area and part fin tip circumferential area.

To model the convective losses the total finned area was used, assuming air flow through the fins, thereby increasing the convective heat transfer area. Lastly, the radiative losses were assumed to only occur at the fin tip area. The base tube is expected to radiate diffusely and the radiation is trapped by the fins. The view factor from the base to ambient is presented in Table three.

These different implementation areas are generated by developing a discrete area ratio of a finned section area to an un-finned section of equivalent length. These ratios are then implemented on the desired control volume size. A grid independence study can be carried out should it be required for better accuracy. The accuracy of the 1-D model to approximate the experiment was found to be questionable and therefore a grid independence study was deemed unnecessary.

H.3. Initialisation

The following section covers the initialisation parameters of the 1-D steady-state analytical model. The receiver is expected to start up from ambient conditions at ambient pressures. It is assumed that the whole system has reached an equilibrium temperature with the ambient environment and that no thermal inertia is carried over from a previous test. Table 12 contains all the initial conditions

Table 12: Initial conditions

Property	Initial state
Iss	1000 W/m^2
$T_{surface}$	300 K
T_{air}	300 K
T_{water}	300 K
$\dot{\mathbf{m}}_{\mathbf{water}}$	0.1079 kg/s
$\dot{\mathbf{m}}_{\mathbf{air}}$	0.0275 kg/s

H.4. Simulation results

For the simulation validation, it was decided to only use the six heliostats in the pod. The relative location to the tower and the receiver tilt (facing the field) enables the assumption that the incident radiation can be approximated as perpendicular to the tubes. This decision allows the heliostat field to be approximated more convenient numerically.

In Figure 50 the Helio40 field layout on the high-temperature solar roof laboratory can be seen. In all the simulation results that follow the initial conditions of Table 12 was used. These six heliostats are expected to produce 5.35 kW_{th} input on the simulated aperture area based on the initial conditions.

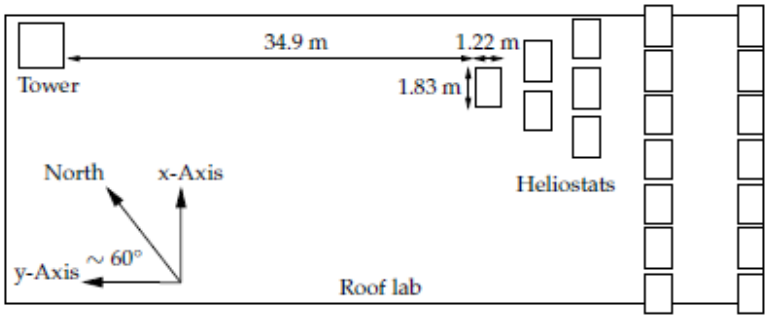

Figure 50: Helio40 field layout (Grobler 2015)

The nature of the receiver geometry, with the first two columns of tubes in a staggered arrangement as depicted in Figure 10, is reflected in the flux data from the ray tracing of the geometry. In Figure 51 it can be observed that the surface temperature predictions do not reduce stepwise towards the back and that the surface temperature of tube 5 is, in fact, higher than that of the neighbours based on its location in the cavity and the resulting view factor to the incident radiation. The flux distribution along the length

of the tube, resembling a Gaussian distribution, is illustrated in the temperature distribution along the length of the tubes.

The lines in the plot are interpreted as the average circumferential surface temperature at the specific control volume. The control volumes are numbered from the fluid entering the receiver until the point where it exits the last tube.

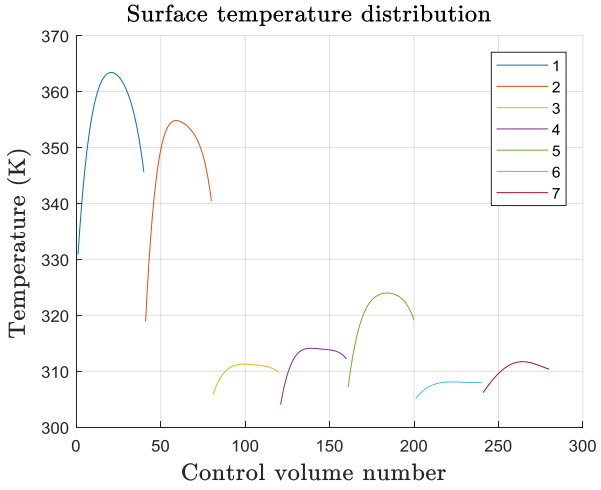

Figure 51: Tube temperature distribution in the receiver depth based on the ray tracing data.

For both the models relying on field estimation a perfect cosine flux profile was assumed (a=2), implying zero incident flux at the edges and max flux in the centre. In Figure 52 the predicted system temperature distribution for the model with variable areas to the different heat transfer modes is presented. Two estimations are made: the first (Figure 52a) is based on the average penetration depth per tube column and the second (Figure 52b) is location specific.

The average penetration depth yields a generic per column surface temperature which can potentially provide reliable system response data while the tube specific data enables comparison to the ray tracing and experimental models. At the flow conditions, the two responses are noted to be dissimilar. The thermal response observed in Figure 52a shows some instability. This is a direct result of the approximation steps taken to approximate the parallel flow in tube rows in the 1-D model.

The predicted surface temperature results are of similar magnitude to Figure 51 however, the approximation does not achieve the geometry

specific response. Furthermore, the model overpredicts the thermal response in comparison with Figure 51.

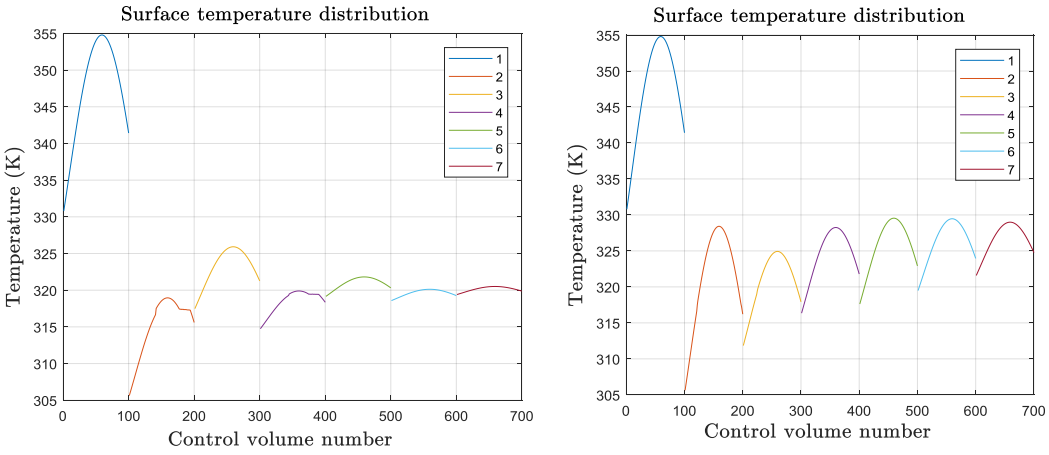

Figure 52: Conservative surface temperature distribution estimation: a) Average column penetration depth, b) Location specific penetration estimation.

The model in Figure 53 incorporates the same radiation assumptions as Figure 52 and the same absorption surfaces are the same as Figure 51. This was taken as a good compromise for simpler and faster solving. The intuitive system behaviour of the receiver can be observed in Figure 53a where the penetration reduces towards the back leading to smaller thermal gradients in tube length. Figure 53b depicts the geometry specific thermal response, the peaks do form a similar trend to Figure 51, however, the large thermal gradients are questionable.

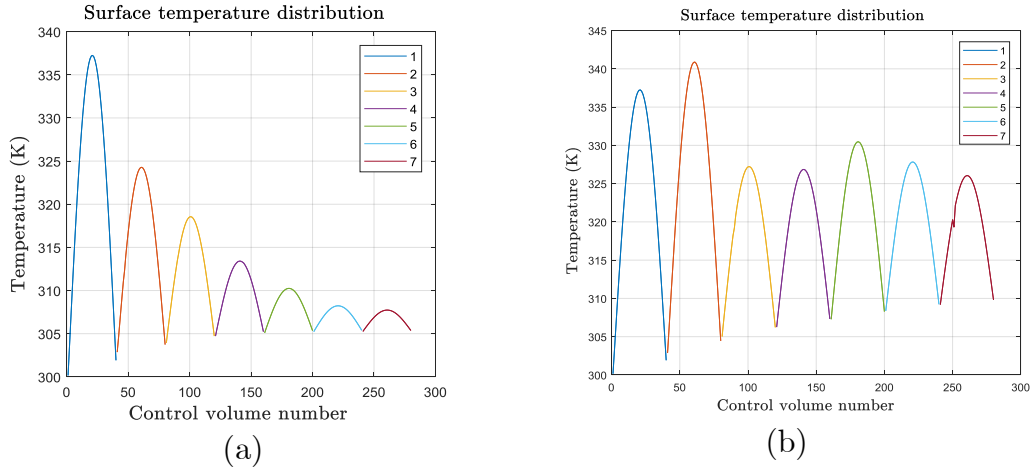

Figure 53: Tube temperature distribution based on field approximation: a) Average column penetration depth, b) Location specific penetration estimation.

The error analysis, in section H.5., compares the three models to measured steady-state data. The incident radiation decline implementation method seems to predict reasonable system behaviour when compared to the ray tracing model however, the flux profile may be significantly different.

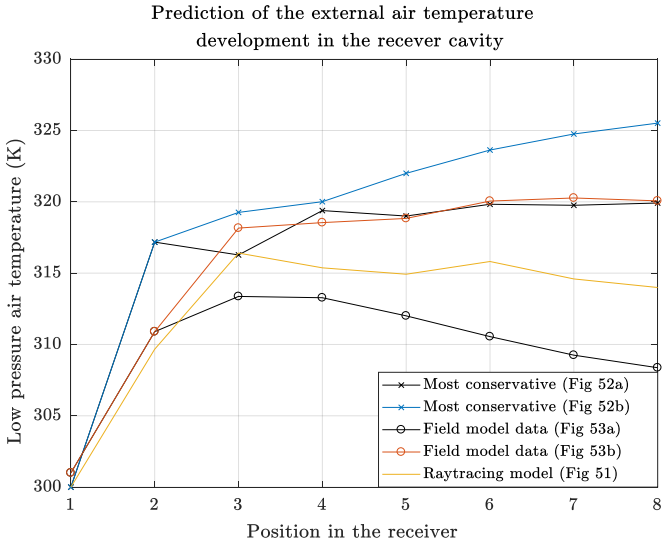

Figure 54: External air temperature development after each row based on the pyranometer data.

The observed behaviour of the external fluid temperature distribution prediction in Figure 54 is true to the surface temperature distribution plots with the highest gradient corresponding to the highest surface temperature crossed. From the negative gradients, it can be deduced that the models solve the energy balance successfully by transferring heat back to surfaces at lower temperatures. When looking at the results in general the models all show a variety of thermal responses. In the error analysis, the most accurate model is selected and evaluated. Using the more accurate validated model the system response to fin geometries was investigated in section 6.2.3.

H.5. Error analysis

H.5.1. Prediction error relative to the ray tracing model

Upon completion of the experimental phase, an error analysis was launched to compare the various 1-D models to the measured response at steady-state conditions. In brief, the environmental conditions were input into all of the respective models for a couple of steady-state responses and

the results compared. The following figure contains the error response for one such steady-state.

The scatter plot in Figure 55 compares the prediction error of the surface temperatures by the various models. The error was calculated relative to the experimental values at the steady-state operation under the same input conditions. A negative percentage is indicative of overestimation and positive underestimation. The geometry specific penetration models show better correlation with the test data, as one would expect. Figures 53a shows the most promising accuracy in estimating the surface temperatures. This alone is however not a good measure of the model accuracy and the ability to determine the harnessed energy was investigated.

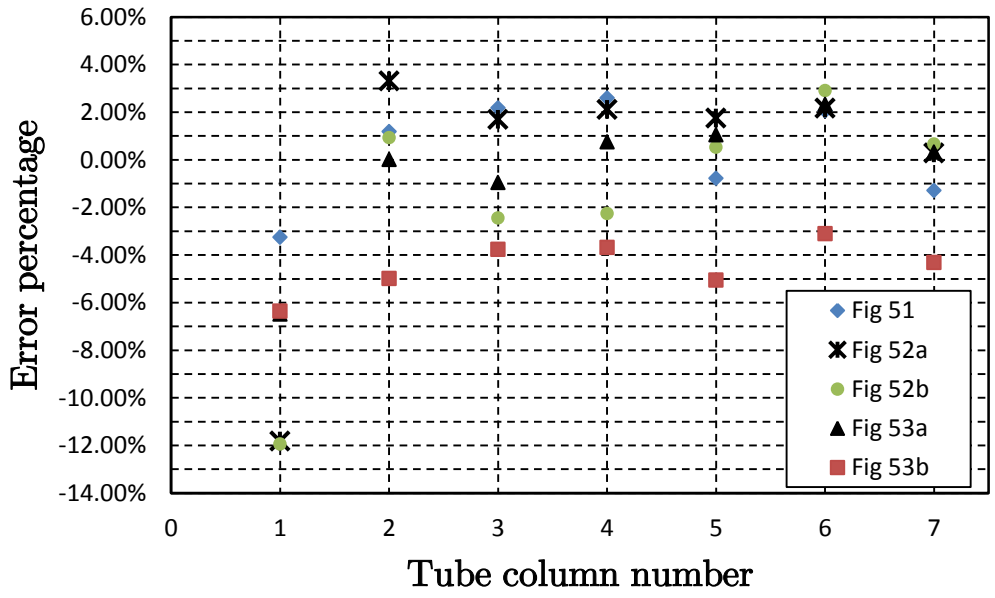

Figure 55: Surface temperature error comparison

The mean square error of the various models is presented in Table 13. As one would expect the root mean square error for surface temperatures indicate that the ray tracing model is most accurate. When investigating the internal fluid mixed results are seen from the models, with the general penetration conservative model performing best. In the case of the external fluid temperature once again mixed results are observed, the model from Figure 53a is performing best. Lastly, the average of the mean square errors is taken which indicates Figure 53a to be the most reliable in estimating the system response.

Table 13: Root Mean Square error comparison of the models

	Fig 51	Fig 52a	Fig 52b	Fig 53a	Fig 53b
Surfaces	6.53	15.36	15.24	8.42	14.45
Internal fluid	0.71	0.35	6.08	2.74	0.94
External fluid	4.71	3.06	1.19	0.57	8.88
Average	3.98	6.26	7.50	3.91	8.09

H.5.2. Prediction errors relative to experimental data

An analysis of the prediction error of the simulation models was carried out. In section H.5.1. the comparison of the different models employed was discussed. Having determined the most accurate model, the analysis could move towards determining the cause of the errors.

Using the chosen model (the model based on field performance estimation and general penetration depth implementation), the steady-state response for a number of tests was compared to the simulated model and compared in Table 14. From the table, it is concluded that the model tends to overestimate the water and surfaces temperatures and under estimate the air temperature. The estimation errors of the surface temperatures are discussed in section H.5.2. and it was concluded that the surface temperature errors are geometry specific.

Table 14: Steady-state prediction error for different tests

Test	Overall error	Surface temp error	Water temp error	Air temp error
2018/07/09 13:00	-33.43%	-41.34%	-100.16%	20.68%
2018/07/09 12:41	-19.25%	-5.91%	-203.90%	29.84%
2018/07/09 14:51	-17.06%	-3.21%	-212.41%	47.72%
2018/07/10 13:00	-6.77%	-1.61%	-117.23%	54.07%
2018/07/10 14:00	-7.88%	-2.42%	-122.78%	53.05%

By increasing the fluid temperature estimate accuracy the overall estimation error can be reduced. The observed external fouling and the discoloration of the internal water, indicating internal fouling, suggested that the errors can be reduced by implementing the fouling in the models. An increase in internal fouling would reduce the energy transferred to the internal fluid which is expected to result in more energy transferred to the external fluid.

The addition of internal fouling provided mixed results which can be found in Table 15. Both the internal and external fluid temperature predictions

increased in accuracy. The surface temperatures, however, increased significantly thereby increasing the root mean square error of the overall system response prediction. This suggested that the flux profile might be at fault by overestimating the total energy incident on the receiver aperture.

Table 15: Investigation of the effect of internal fouling results

	No internal fouling				Internal fouling			
Test	1	2	3	4	1	2	3	4
T_{water}	-24.62%	-22.29%	-23.79%	-22.67%	0.78%	6.02%	-8.94%	2.15%
T_{air}	27.85%	28.75%	3.39%	30.73%	-30.48%	-19.26%	-59.26%	-9.88%
Overall RMSE	7.495	7.167	7.555	7.189	37.024	36.865	43.291	33.694

The exact flux profile could not be measured at the time of this investigation due to a lack of equipment. This modelling was used as an estimation tool with which the working can be predicted. The expected accuracy of a 1-D steady-state model with regards to predicting the performance of such a complex receiver is low and efforts to increase the model complexity, therefore, deemed unnecessary.

A more accurate 3-D finite element and finite volume analysis should be considered instead for predictive plant modelling. The complexity of the receiver geometry results in a computationally very expensive simulation which was beyond the scope of this investigation.

H.6. Conclusion on simulation work

The setup and modelling assumptions were presented which was used to approximate the thermal response of the receiver. The ability of the 1-D steady-state model to predict the receiver behaviour is limited to the validity of the assumptions. These models were accepted as adequate for this investigation where a preliminary estimation model was required. In future work, a more detailed analysis can potentially be undertaken by expanding the modelling to 3-D space. With the aid of the experimental data, such a simulation can be validated.

References

Papers:

ACIN (2016) 'Betz Micromanometer Manual'. Available at: http://www.acin.nl/wp-content/uploads/2016/06/Betz-manual-NL-EN-web.pdf.

Allen, K. G. (2010) 'Performance characteristics of packed bed thermal energy storage for solar thermal power plants by', (March). Available at: http://scholar.sun.ac.za/handle/10019.1/4329.

Amsbeck, L., Buck, R.,Heller, P., Jedamski, J. & Uhlig, R., (2008) 'Development of a tube receiver for a solar-hybrid microturbine system', in *Proceedings of 14th SolarPACES Conference, Las Vegas, NV, March*, pp. 4–7. Available at: http://elib.dlr.de/54223/1/Lars_Amsbeck_Development_of_a_tube_receiver_for_a_solar-hybrid_microturbine_system_Solarpaces2008_proceedings.doc.pdf.

Ávila-Marín, A. L. (2011) 'Volumetric receivers in Solar Thermal Power Plants with Central Receiver System technology: A review', *Solar Energy*, 85(5), pp. 891–910. doi: 10.1016/j.solener.2011.02.002.

Basson, E. J. J., Hoffmann, J. E. and Sebitosi, A. B. (2018) 'Design and testing of externally finned tube cavity receiver for brayton cycle preheating purposes', in. 5th Anual Southern African Solar Energy Conference. Available at: https://www.sasec.org.za/full_papers/7.pdf.

Campbell Scientific, I. (2009) 'CS215 Temperature and Relative Humidity Probe'.

Craig, K., Gauché, P. and Kretzschmar, H. (2013a) 'Optimization of solar tower hybrid pressurized air receiver using CFD', in *Proceedings of SolarPACES*, pp. 1–10.

Craig, K. J., Gauché, P. and Kretzschmar, H. (2013b) 'Optimization of solar tower hybrid pressurized air receiver using CFD and mathematical optimization', *Energy Procedia*. Elsevier B.V., 49(April 2015), pp. 324–333. doi: 10.1016/j.egypro.2014.03.035.

Craig, K. J., Le Roux, W. G. and Meyer, J. P. (2015) 'Computational Fluid Dynamics Analysis of Parabolic Dish Tubular Cavity Receiver', (May), pp. 260–265. Available at: https://repository.up.ac.za/handle/2263/49550.

Dewan, A., Mahanta, P., Raju, K. S., Kumar, P., S., (2004) 'Review of passive heat transfer augmentation techniques', *Proceedings of the Institution of Mechanical Engineers, Part A: Journal of Power and Energy*, 218(7), pp. 509–527. doi: 10.1243/0957650042456953.

DLR (2010) *SOLHYCO Report Summary*. Cologne, Germany. Available at: https://cordis.europa.eu/result/rcn/52948_en.html.

Erasmus, S. J., Von Backström, T. W., Lubkoll, M., & Dinter, F. (2018) 'Design and development of a next generation thermal rock bed storage experimental facility', in. 5th Anual Southern African Solar Energy Conference, Durban South Africa. Available at: https://www.sasec.org.za/full_papers/33.pdf

Fend, T. (2012) 'Characterization of Advanced Solar Air Receiver Materials', pp. 1–27. Available at: http://elib.dlr.de/77652/1/Materials.pdf.

Freescale (2009) 'Freescale Semiconductor Integrated Silicon Pressure Sensor On-Chip Signal Conditioned , Temperature Compensated and Calibrated', *Sensors (Peterborough, NH)*, pp. 2007–2009.

Grobler, A. (2015) *Aiming strategies for small central receiver systems*. Stellenbosch University. Available at: https://scholar.sun.ac.za.

Heller, L. (2013) *Literature Review on Heat Transfer Fluids and Thermal Energy Storage Systems in CSP Plants STERG Report*. Available at: https://pdfs.semanticscholar.org/0535/3e299330ac84882ab456a6c63fcd9ecc3118.pdf.

Heller, L. (2017) *Development of a Dual-Pressure Air Receiver System for the SUNDISC Cycle*. Stellenbosch University. Available at: http://scholar.sun.ac.za/handle/10019.1/101315.

Heller, L. and Gauché, P. (2013) 'Dual-pressure air receiver cycle for direct storage charging', *Energy Procedia*. Elsevier B.V., 49, pp. 1400–1409. doi:

10.1016/j.egypro.2014.03.149.

International Energy Agency (2010) 'Technology Roadmap Concentrating Solar Power', *Current*, 5, pp. 1–52. doi: 10.1787/9789264088139-en.

IPCC (2018) *Global Warming of 1.5°C. Summary for Policymakers*. Available at: http://report.ipcc.ch/sr15/pdf/sr15_spm_final.pdf.

Kipp & Zonen (2018) 'For unattended direct normal incidence solar radiation measurement', *Pyrheliometers*. Available at: http://www.kippzonen.com/Download/43/Pyrheliometers-Brochure.

Kretzschmar, H. (2013) 'Hybrid Pressurized Air Receiver', in *STERG Symposium*. Stellenbosch: Solar Thermal Energy Research Group. Available at: http://sterg.sun.ac.za/wp-content/uploads/2013/09/2.3_H.-Kretzschmar_Hybrid-Pressurized-Air-Receiver-HPAR1.pdf.

Kretzschmar, H. (2014) 'The Hybrid Pressurized Air Receiver (Hpar) for Combined Cycle Solar Thermal Power Plants', (March). Available at: http://scholar.sun.ac.za.

Kribus, A., Doron, P., Rubin, R., Karni, J., Reuven, R., Duchan, S. & Taragan, E. (1999) 'A Multistage Solar Receiver':, *Solar Energy*, 67(1–3), pp. 3–11. doi: 10.1016/S0038-092X(00)00056-6.

Kröger, D.G. (2011). SUNSPOT The Stellenbosch University Solar Power Thermodynamic Cycle. Tech. Rep., Stellenbosch University, Stellenbosch. Available at: http://blogs.sun.ac.za/sterg/files/2011/05/SUNSPOT-2.pdf

Laubscher, H. F. (2017) 'Developing and Testing a Cost Effective Thermal Rock Bed Storage System by', (December). Available at: http://scholar.sun.ac.za/handle/10019.1/102842.

Lubkoll, M. (2017) *Performance Characteristics of the Spiky Central Receiver Air Pre-heater (SCRAP)*, *Elsieier*. Stellenbosch University. Available at: https://scholar.sun.ac.za.

Lubkoll, M., Backström, T. W. Von and Kröger, D. G. (2014) 'Survey on Pressurized Air Receiver Development', in *2nd Southern African Solar Energy Conference 2014*.

Moghimi, M. A., Craig, K. J. and Meyer, J. P. (2015) 'A novel

computational approach to combine the optical and thermal modelling of Linear Fresnel Collectors using the finite volume method', *Solar Energy*. Elsevier Ltd, 116(February 2016), pp. 407–427. doi: 10.1016/j.solener.2015.04.014.

Nel, J. C. (2017) *Development of an Open Volumetric Air Receiver for a Rock Bed Thermal Energy Storage System*. Available at: http://scholar.sun.ac.za/handle/10019.1/102918.

Olivier, J. G. J., Schure, K. M. and Peters, J. A. H. W. (2017) 'Trends in Global CO_2 and Total Greenhouse Gas Emissions', *PBL Netherlands Environmental Assessment Agency*, (September 2017). Available at: http://www.pbl.nl/sites/default/files/cms/publicaties/pbl-2017-summary-trends-in-global-co2-and-total-greenhouse-gas-emissions-2983.pdf.

Reddy, K. S. and Kumar, N. S. (2009) 'An improved model for natural convection heat loss from modified cavity receiver of solar dish concentrator', *Solar Energy*. Elsevier Ltd, 83(10), pp. 1884–1892. doi: 10.1016/j.solener.2009.07.001.

Rodríguez-Sánchez, M. R., Sánchez-González, A., Marugán-Cruz, C., & Santana, D. (2013) 'New designs of molten-salt tubular-receiver for solar power tower', *Energy Procedia*. Elsevier B.V., 49, pp. 504–513. doi: 10.1016/j.egypro.2014.03.054.

Romero, M., Buck, R. and Pacheco, J. E. (2002) 'An Update on Solar Central Receiver Systems, Projects, and Technologies', *Journal of Solar Energy Engineering*, 124(2), p. 98. doi: 10.1115/1.1467921.

Le Roux, W. G., Bello-Ochende, T. and Meyer, J. P. (2011) 'Maximum Net Power Output of the Recuperative Open and Direct Solar Thermal Brayton Cycle', pp. 1–10. doi: 10.1115/ES2011-54189.

Le Roux, W. G., Bello-Ochende, T. and Meyer, J. P. (2014) 'The efficiency of an open-cavity tubular solar receiver for a small-scale solar thermal Brayton cycle', *Energy Conversion and Management*. Elsevier Ltd, 84, pp. 457–470. doi: 10.1016/j.enconman.2014.04.048.

Le Roux, W. G., Meyer, J. P. and Bello-Ochende, T. (2015) 'Experimental Testing of a Tubular Cavity Receiver for a Small-', (May), pp. 295–300. Available at:

https://repository.up.ac.za/bitstream/handle/2263/49493/LeRoux_Experimental_2015.pdf?sequence=1.

Schmidt, K. G. (2010) *VDI Heat Atlas: M1 Heat Transfer to Finned Tubes*. 2nd Ed. Düsseldorf Germany: Springer. Available at: https://link.springer.com/content/pdf/10.1007%2F978-3-540-77877-6.pdf.

Siddique, M., Khaled, A. R. A., Abdulhafiz, N. I. & Boukhary, A. Y. (2010) 'Recent advances in heat transfer enhancements: A review report', *International Journal of Chemical Engineering*, 2010(1). doi: 10.1155/2010/106461.

The Engineering toolbox: Absorbed Solar Radiation. 2018. Absorbed Solar Radiation . [ONLINE] Available at: https://www.engineeringtoolbox.com/solar-radiation-absorbed-materials-d_1568.html. [Accessed 10 August 2018].

Yellowhair, J., Ho, C. K., Ortega, J. D. & Christian, J. M. (2015) 'Testing and optical modeling of novel concentrating solar receiver geometries to increase light trapping and effective solar absorptance', *SPIE Proceedings*, 9559, p. 95590A. doi: 10.1117/12.2186647.

Books:

Callister, W.D. and Rethwisch, D.G. (2011). Material Science and Engineering, 8th ed. Asia: John Wiley & Sons Pte Ltd, ISBN 978-0-470-50586-1

Çengel, Y.A. and Boles, M.A. (2011). Thermodynamics. 7th ed. Singapore: McGraw-Hill Education. ISBN 978-007-131111-3

Çengel, Y.A. and Ghajar, A.J. (2015). Heat and Mass Transfer: Fundamentals and Applications. 5th ed. Singapore. McGraw-Hill Education. ISBN 978-981-4595-27-8

Çengel, Y.A and Cimbala, J.M. (2014). Fluid Mechanics: Fundamentals and Applications. 3rd ed. Singapore.McGraw-Hill Education. ISBN 978-1-259-01122-1

Duffie, J.A. and Beckman, W.A. (2006). Solar Engineering of Thermal Processes, vol. 53. Wiley. ISBN 0471698679.

Figliola, S.R and Beasley, D.E. (2011). Theory and Design for Mechanical Measurements. 5th ed. Asia: John Wiley & Sons Pte Ltd, ISBN 978-0-470-64618-2

Kaltschmitt, M., Streicher, W. and Wiese, A. (2007). Renewable Energy: Thechnology, Economics and Environment. Berlin New York. Springer. ISBN 978-3-540-70949-7

Mills, A.F. and Ganesan, V. (1999). Heat transfer, 2nd ed. India: Pearson Education. ISBN 9780139476242

Budynas, R.G. and Nisbett, J.K. (2015) Shigley's Mechanical Engineering Design, 10th ed. New York, McGraw-Hill Education. ISBN978-981-4595-28-5